Nitriding – fundamentals, modeling and process optimization

by

Mei Yang

A Dissertation

Submitted to the Faculty

of the

WORCESTER POLYTECHNIC INSTITUTE

in partial fulfillment of the requirements for the

Degree of Doctor of Philosophy

in

Material Science and Engineering

April 2012

Approved: _____

Prof. Richard D. Sisson Jr, Advisor

Director of Manufacturing and Materials Engineering

George F. Fuller Professor

ABSTRACT

Gas nitriding is an important thermochemical surface treatment that is used to improve the wear and corrosion resistance as well as the fatigue endurance of steel parts. Accurate process control is the effective way to ensure the properties reliability of nitriding process. To realize the accurate process control, the nitriding process parameters need to be modeled and controlled to meet the specifications.

There has been ongoing effort on the simulation of the gas nitriding process since 1990s. However, most of the work has been done to simulate the gas nitriding process of pure iron due to the limited thermodynamics and kinetics information available on the gas nitriding process of steels. The objective of this project is to develop an accurate and user friendly software model to simulate the gas nitriding process of steels based on the fundamental understanding of thermodynamics and kinetics.

In this work, the customized Lehrer diagram which describes the phase stabilities in specified steel as a function of nitriding potential and temperature has been successfully constructed by computational thermodynamics for the first time. Based on the Lehrer diagrams for steels, the compound layer growth model is proposed to simulate the gas nitriding process of steels. By using this model, the properties of the nitrided steels based on the phase constitution, surface nitrogen concentration, nitrogen concentration profile, case depth, as well as growth kinetics can be simulated as a function of the process parameters (temperature, time, and the nitriding atmosphere). The results of the model are in excellent agreement with experimental results.

TABLE OF CONTENTS

ACKNOWLEDGEMENTS

I wish to express my sincere gratitude to my advisor, Professor Richard D. Sisson Jr., for his constant advice, guidance, and encouragement during my Ph.D. study at WPI.

I also wish to express my gratitude to Professor Diran Apelian, Professor Makhlouf Makhlouf, Professor Satya Shivkumar, Professor Jianyu Liang, and Professor Yong-Ho Sohn for their help, encouragement, and serving in my thesis committee.

I owe my deepest gratitude to Professor Sisson and Professor Apelian for giving me the chance to back to school and work on this project. Without their help, I cannot imagine where I am now.

I would also take the opportunity to thank all my friends and colleagues as well as the faculty and staff in the Materials Science and Engineering program for their help and cooperation during my stay at WPI.

I am grateful to Rita Shilansky for her constant assistance and Dr. Boquan Li for helping me to carry out the experiments.

The financial support of the Center for Heat Treating Excellence at the Metal Processing Institute and the consortium member companies, which was essential for my graduate studies, is gratefully acknowledged.

I would like to thank Craig Zimmerman, Dennis Donahue, and Terry Flanagan from Bluewater Thermal Solutions, Mohammed Maniruzzaman, Zachary S. Birky and Ryan A. Dusheke from Caterpillar Inc., Madeleine. C. Smith, Kyle. P. Schafer and Danielle. M. Karenus from Cummins Inc. for their experimental assistance.

It is a pleasure to thank Paul Mason and Qing Chen from Thermo-Calc Software Inc for their assistance and continuing support.

Finally, I would like to thank my family members, especially my husband, Yu Zhong and my son, Alex Zhong for their constant encouragement and invaluable support. Without my husband's understanding and faith in me this thesis could not have been completed.

Chapter 1

INTRODUCTION

Gas nitriding is a thermochemical surface treatment in which nitrogen is transferred from an ammonia atmosphere into the surface of steels at temperatures within the ferrite and carbide phase region. [1, 2] After nitriding, a compound layer and an underlying diffusion zone (i.e. case) are formed near the surface of the steel. The compound layer, also known as the white layer, consists predominantly of ε - $Fe_{2-3}(C, N)$ and/or γ' - Fe_4N phases and can greatly improve the wear and corrosion resistances. [3] The hardened diffusion zone, which is composed of interstitial solid solution of nitrogen dissolved in the ferrite lattice and nitride and/or carbonitride precipitation for the alloy steels containing the nitrides forming elements, is responsible for a considerable enhancement of the fatigue endurance. Furthermore, being a low temperature process, nitriding minimizes the distortion and deformation of the heat treated parts. [1] Therefore, nitriding is an important surface treatment for ferritic steels.

Although the industrial use of the gas nitriding began in the 1930s, it has not gained wide applications mainly due to its low performance reliability. [4] The properties of nitrided steels are determined by the nitrided case microstructures. To ensure the reproducible and desirable properties from batch to batch, the gas nitriding need to be controlled to ensure the microstructure evolution. The successful gas nitriding process control depends on: 1) process parameters selection to meet the specification, 2) accurate process parameters control during the process.

The gas nitriding process parameters include temperature, time, and the nitriding atmosphere. For the nitriding atmosphere control, the ammonia dissociation rate was traditionally adopted as the controlling parameter. It represents the percentage of ammonia dissociated into hydrogen and nitrogen and is manually measured by using a burette in the furnace exhaust gas. Since dissociation rate is not an in-situ measurement and the measurement is done manually, it introduces operator induced variability and cannot provide the accurate control on the nitriding process. A new control parameter, the nitriding potential, was introduced in the 1990's [5]. The nitriding potential is defined by;

$$K_n = \frac{p_{NH_3}}{p_{H_2}^{3/2}} \tag{1}$$

where p_{NH_3} and p_{H_2} are the partial pressures of the ammonia and hydrogen gases respectively. By utilizing the thermal conductivity hydrogen sensor in conjunction with the two-loop controller/programmer, the nitriding potential can be calculated and controlled automatically and accurately.

With the development of measure and control systems, the gas nitriding process parameters can be controlled accurately. How to pre-define the nitriding process parameters to meet the specifications becomes the main challenge of the gas nitriding process control. Conventionally, trial and error methods were used to define the nitriding process parameters to meet the specifications. This method is expensive, time consuming, and hard to control. Therefore, an effective simulation tool is needed to define the process parameters based on the performance specifications of various steels. By using this tool, the properties of the nitrided steels based on the phase constitution, surface nitrogen concentration, nitrogen concentration profile, case depth, as well as growth kinetics can

be simulated through variation of process parameters (temperature, time, and the nitriding atmosphere). [6]

There has been ongoing effort on the simulation of the gas nitriding process since 1990s and most of the work has been done to simulate the nitriding process of pure iron [7-9]. However, the pure iron is never used for nitriding in industry while the simulation for nitridable steels is greatly needed.

The objective of this work is to develop a computational model to determine the nitrogen concentration and nitride profiles in the nitrided steels in terms of temperature, atmosphere composition, steel surface condition, alloy composition and the pre-nitriding steel microstructure. Based on this model, the nitride profile as well as the nitrogen concentration profile can be predicted from the input of the process parameters such as nitriding potential, temperature, time, and the steel composition.

To construct this model, it is worthwhile to investigate the thermodynamics and kinetics involved in the gas nitriding process of steels. In the first part of this work (Paper #1), thermodynamic calculations and experimental work have been completed to help determine the effects of process parameters (i.e. temperature and nitriding potential as well as the starting steel microstructure and composition) on the nitriding process.

Base on thermodynamics, the nitrogen concentration and nitride phase constitution at the surface of the nitrided case are determined by the temperature and nitriding potential. The Lehrer diagram, which describes the phase stabilities in pure iron under different nitriding potentials and temperatures, is inherently designed to provide the gas nitriding process parameters. This diagram was developed by experiments in 1930

[10] and there is no experimentally determined Lehrer diagrams available for alloy steels. Therefore, Lehrer diagram has been widely used to provide the process control parameters for the gas nitriding process of steels in industry. However, applying the pure iron Lehrer diagram for the steels can lead to erroneous results because of the different phase stabilities in the steels.

In the second part of this work (Paper #2), the Lehrer diagram of AISI 4140 steel was determined for the first time by computational thermodynamics and nitriding experiments were also carried out to verify the predictions of customized AISI 4140 Lehrer diagram. The customized Lehrer diagrams can determine the composition and phases at the surface of the nitrided steels.

In the third part of this work (Paper #3), a series of customized Lehrer diagrams are developed to analyze the effects of carbon and manganese on the nitriding process. These diagrams can be used to provide the nitriding process parameters for the specified steels but also pave a way for computational materials design of nitridable steels.

Besides temperature and nitriding potential, time is another important process control parameter. To investigate the time effect on the nitriding process, the kinetics during the gas nitriding process should be investigated.

In the fourth part of this work (Paper #4), the compound layer growth model, which is derived from the nitride layer growth model of pure iron [7], is for the first time developed to simulate the compound layer growth kinetics for steels. This model can be used to predict the nitride and nitrogen concentration profiles as a function of time and

position during the nitriding process of steels. In addition, it can be used to predict the thickness of the compound layer.

References

[1]   Pye D. Practical nitriding and ferritic nitrocarburizing. Materials Park, OH: ASM International, 2003.

[2]   Somers MAJ. Thermodynamics, kinetics and microstructural evolution of the compound layer; A comparison of the states of knowledge of nitriding and nitrocarburizing. Heat Treatment of Metals 2000;27:92.

[3]   Du H, Somers M, Agren J. Microstructural and compositional evolution of compound layers during gaseous nitrocarburizing. Metallurgical and Materials Transactions A 2000;31:195.

[4]   Zinchenko V, Syropyatov V. New possibilities of gas nitriding as a method for anticorrosion treatment of machine parts. Metal Science and Heat Treatment 1998;40:261.

[5]   Lotze TH. GAS NITRIDING. Application Bulletin, vol. Issue 1: Super Systems, Inc., 2003.

[6]   Maldzinski L, Liliental W, Tymowski G, Tacikowski J. New possibilities for controlling gas nitriding process by simulation of growth kinetics of nitride layers. Surface Engineering 1999;15:377.

[7]   Somers MAJ, Mittemeijer EJ. Layer-Growth Kinetics on Gaseous Nitriding of Pure Iron - Evaluation of Diffusion-Coefficients for Nitrogen in Iron Nitrides. Metallurgical and Materials Transactions a-Physical Metallurgy and Materials Science 1995;26:57.

[8]   Somers MAJ, Mittemeijer EJ. Modeling the Kinetics of the Nitriding and Nitrocarburizing of Iron. Heat Treating 1997: Proceedings of the 17th Conference (ASM International) 2000;15-18:321.

[9]   Torchane L, Bilger P, Dulcy J, Gantois M. Control of iron nitride layers growth kinetics in the binary Fe-N system. Metallurgical and Materials Transactions a-Physical Metallurgy and Materials Science 1996;27:1823.

[10]   Lehrer E. The equilibrium, iron-hydrogen-amnonia. Zeitschrift fuer Elektrochemie und Angewandte Physikalische Chemie 1930;36:383.

Chapter 2

LITERATURE REVIEW

1.1. Fundamental of nitriding process

Nitriding is a thermochemical surface treatment in which nitrogen is transferred from a media into the steel at temperatures completely within the ferrite and carbide phase field [1-3].

After nitriding, a compound layer and an underlying diffusion zone (i.e. case) are formed at the surface of the steel. The compound layer, also known as the white layer, consists predominantly of ε-$Fe_2(N,C)_{1-x}$ and/or γ'-Fe_4N phases[4]. In the region beneath the compound layer, the so-called diffusion zone or case, for pure iron, nitrogen from outside dissolves interstitially in the ferrite lattice at the nitriding temperature. For the steel containing nitride forming elements, alloy nitride precipitates are also formed in the diffusion zone[3, 5, 6]. Figure 1 presents the schematic compound layer and diffusion zone structure of nitrided iron/steel.

The compound layer can have greatly improved wear and corrosion resistance [4]. The hardened diffusion zone is responsible for a considerable enhancement of the fatigue endurance. Furthermore, being a low temperature process (performed in the ferrite regime on Fe-N phase diagram does not requiring quenching). Nitriding minimizes distortion and deformation of the heat treated parts [3]. Therefore, nitriding is an important surface heat treatment for ferritic steels and can be widely used.
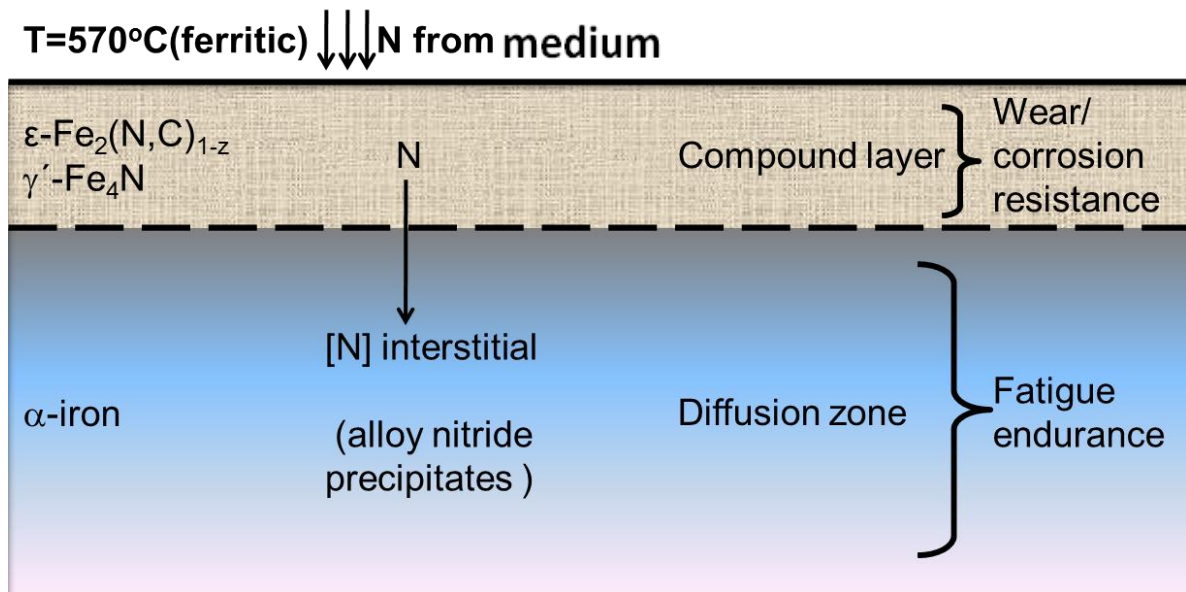
Figure 1. Schematic compound layer and diffusion zone structure of nitrided iron/steel

1.1.1. Various nitriding processes

According to the medium used to provide the nitrogen, the nitriding process can be classified as gas nitriding, plasma nitriding, pack nitriding, and salt bath nitriding.

1.1.1.1. Gas nitriding

In gas nitriding, nitrogen is introduced into a steel surface from a controlled atmosphere by holding the metal at a suitable temperature in contact with a nitrogenous gas, usually ammonia, NH_3. The process represents one of the most efficient among the various methods of improving the surface properties of engineering components, especially the parts with complicated shapes requiring homogeneous hardening of the surface [7].

1.1.1.2. Plasma nitriding

Plasma nitriding uses plasma-discharge technology at lower temperature to introduce nascent nitrogen on the steel surface. It is another well-established surface hardening process in steel [8, 9] and also known as ion nitriding. Plasma is formed by high-voltage electrical energy in vacuum. Nitrogen ions are then accelerated to impinge on the workpiece which is connected as a cathode. The ion bombardment heats the work piece, cleans the surface and provides the nascent nitrogen for diffusion into the steel material [10].

1.1.1.3. Pack nitriding

Pack nitriding uses nitrogen-bearing organic compounds as a source of nitrogen [10]. The steels are packed in glass, ceramic or aluminum containers together with the nitriding compound which is often dispersed in an inert packing media. Upon heating, the organic compounds used in the process form reaction products that are relatively stable at temperatures up to 570°C. The reaction products are decomposed at the nitriding temperature and they provide a source of nitrogen. The process time can range from 2 hours to 16 hours.

1.1.1.4. Salt bath nitriding

Salt bath nitriding process is carried out in a molten salt bath. It can be applied to carbon steels, low-alloy steels, tool steels, stainless steels and cast iron. The case hardening medium is a nitrogen-bearing salt bath containing cyanides or cyanates. During the process, the dimensional stability of the workpiece can be preserved, thus processing

of finished parts is possible. This implies that it can be used to complement engineering properties developed during carburizing and carbonitriding.

1.1.2. Fe-C binary and Fe-C-N ternary phase diagrams

Phase diagrams are the base to understand the phase evolution during the nitriding process. Figure 2 shows the experimental Fe-N binary phase diagram in which, Fe_4N is usually called γ' phase and ε represents Fe_2N_{1-x}. On this phase diagram, the complete ferritic phase range is below the eutectoid temperature (around 590°C). It shows that when the nitrogen concentration exceeds the nitrogen solubility limitation of α-Fe (ferrite), the first phase developing at the surface of the ferrous substrate is γ' (near 6 wt.% N). Then ε phase is formed with increasing of the nitrogen concentration.
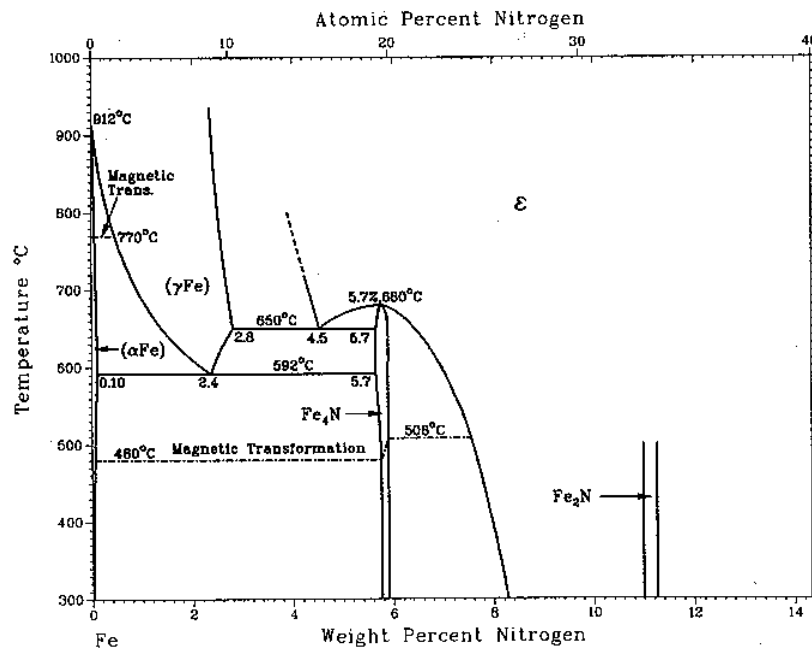
Figure 2. Fe-N binary phase diagram [11].

However, the Fe-N-C ternary phase diagram proposed by Slycke et al. [12] Figure 3 shows the ε phase becomes the first nitride phase formed in compound layer with the presence of carbon. By controlling the nitrogen and carbon concentration the single ε phase can be developed. And γ' phase is only formed during a relative low carbon concentration range and coexists with ε phase. This is explained by the crystallographic resemblance between orthorhombic and hexagonal. Cementite (Fe_3C), which composes the matrix when carbon exists, has orthorhombic crystal structure and can easily be converted into hexagonal ε phase.[13]
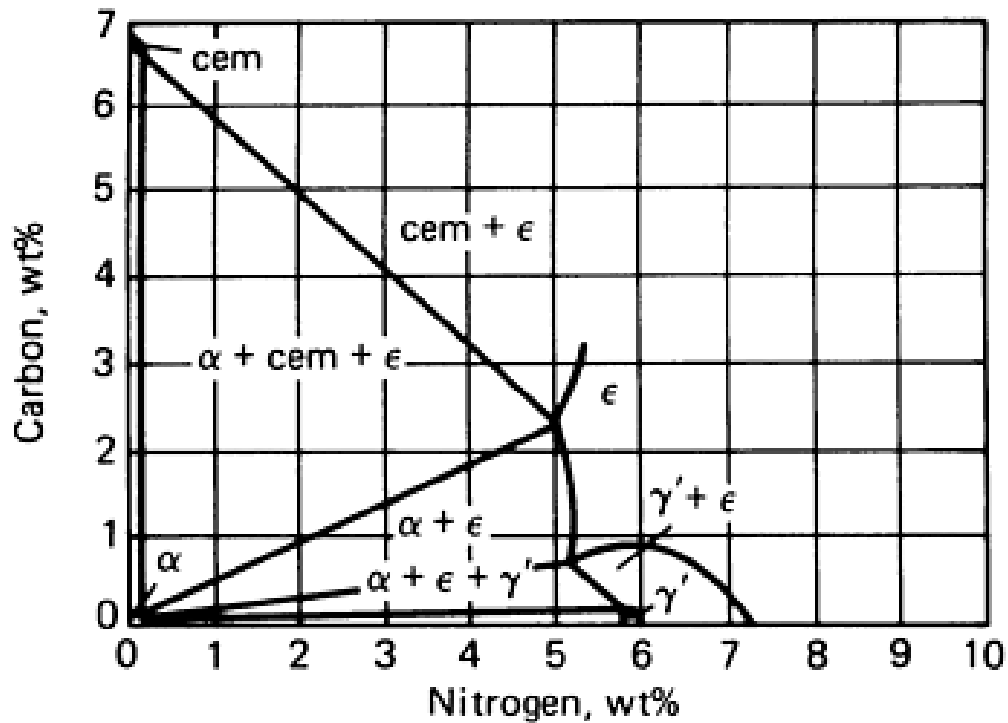
Figure 3.Tentative Fe-N-C phase diagram at 570-580˚C. Sizes of α, γ′ and cementite fields are not in scale [12].

1.1.3. Microstructures

The microstructure of nitrided iron is shown in Figure 4. It is clear that the compound layer is composed of sublayers of ε phase and γ′ phase. The ε phase is close to the surface and the γ′ phase is near to the diffusion zone.

(a)   (b)
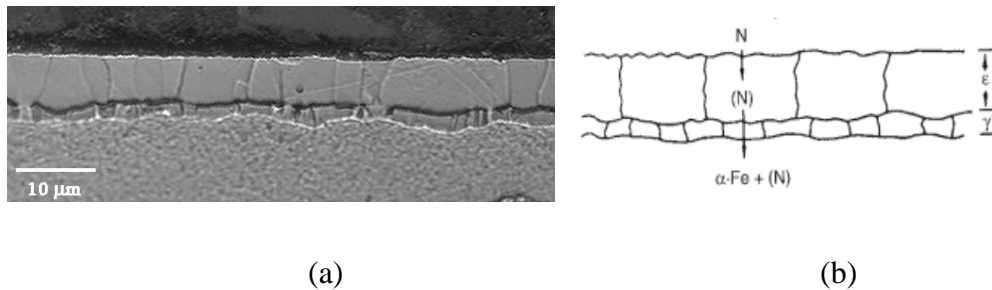
Figure 4. (a) Compound layer structure of nitrided iron [14] (b) Schematic sequence of phases during iron nitriding [15]

However, the well-defined ε and γ′ sublayer structure is replaced by a mixture of ε and γ′ phases in steel as shown in Figure 5[16]. In Figure 5 ε_1 and ε_2 represent Fe_2N_{1-x} and $Fe_2(N,C)_{1-x}$, respectively. The microstructure change in compound layer is due to the presence of carbon in steel matrix, which is in good agreement with the previous Fe-C-N ternary phase diagram (Figure 3) description.

1.2. Gas nitriding

The current project is focusing on the fundamental investigation and modeling of gas nitriding process. As it is previously described, gas nitriding is a thermochemical surface treatment in which nitrogen is transferred from nitrogenous gas, usually

ammonia, NH_3 into the steel at temperatures completely within the ferrite and carbide phase field [1-3], usually 570°C [17].
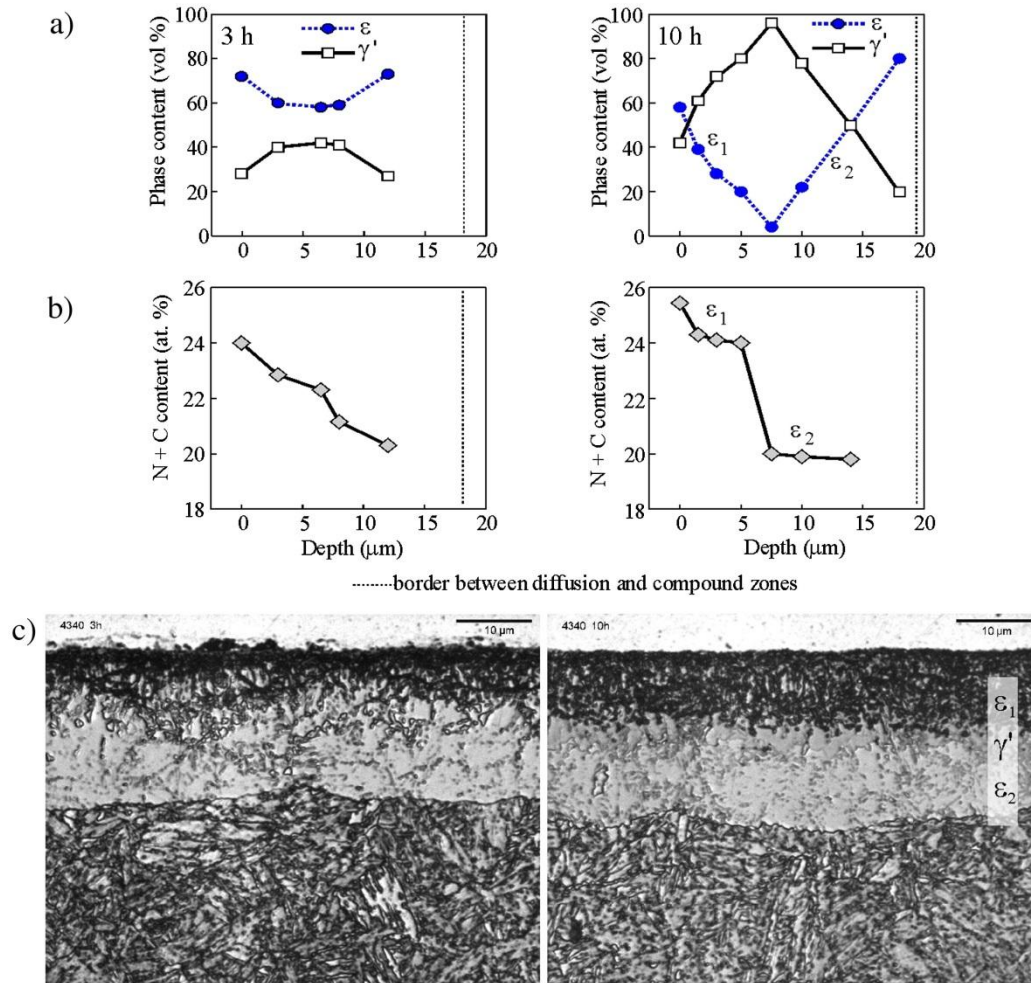
Figure 5.The final phase composition of (carbo)nitrides zone after 3 and 10 h of single-stage process at $K_N = 3.25$ and $T = 853$ K (580 °C): a. depth distributions of ε and γ' phases in the compound zone on steel 4340; b. total interstitial content (N + C) as a function of depth; c. optical micrographs of the cross sections of the compound zone—γ' appears dark grey, ε appears light grey. [16]

During the gas nitriding, ammonia, NH_3 is used as nitrogen-providing medium due to the relatively higher chemical potential of nitrogen compared to nitrogen gas, N_2. The chemical potential of nitrogen in N_2 is extremely low and an equilibrium N_2 pressure up to several thousand atmospheres would be necessary to incorporate a considerable amount of nitrogen into the steel surface.[18]
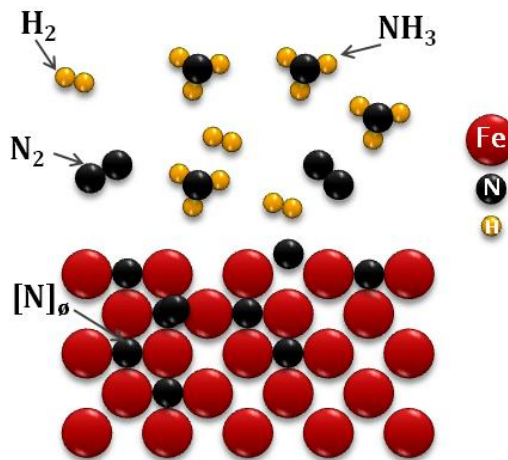
Figure 6. Schematic illustration of gas nitriding

For the illustration of the gas nitriding (Figure 6), the dissolution of nitrogen in steel occurs via the dissociation of ammonia at the surface

$$NH_3 = N_{ad} + \frac{3}{2}H_2 \tag{1}$$

Followed by the dissolution of nitrogen in steel

$$N_{ad} = [N] \tag{2}$$

and/or the formation of nitrogen gas

$$N_{ad} + N_{ad} = N_2 \tag{3}$$

where N_{ad} denotes N adsorbed at the steel surface and [N] represents nitrogen which is

dissolved in the steel surface.

1.3. Process control for gas nitriding

The dissociation rate of ammonia or the nitriding potential are the most critical parameters to understand and control the nitriding process. The chemical potential of nitrogen, μ_N, thermodynamically defines the nitridability of the nitriding atmosphere. [19] At thermodynamic equilibrium, the chemical potential in the steel surface (μ_{N_s}) equals

that in the nitriding atmosphere ($\frac{1}{2}\mu_{N_2,g}$). That means

$$\frac{1}{2}\mu_{N_2,g} = \mu_{N_s} \tag{4}$$

And the chemical potential of nitrogen in the steel can be related to nitrogen

activity a_N by

$$\frac{1}{2}\mu^0_{N_2,g} + \frac{1}{2}RT\ln\left(\frac{p_{N_2}}{p^0_{N_2}}\right) = \mu^0_{N_s} + RT\ln a_N \tag{5}$$

where R is the gas constant, T is temperature, p_{N_2} is the partial pressure of nitrogen, $p^0_{N_2}$ is

the partial pressure of nitrogen at the standard state.

Since the chemical potential of nitrogen is extremely low in N_2 and relatively high in ammonia, ammonia is used as the principal constituent of the nitriding atmosphere, [19] giving

$$NH_3 = [N] + \frac{3}{2}H_2 \tag{6}$$

where [N] represents nitrogen which is dissolved on the steel surface.

For local equilibrium between N in the gas phase and N in the steel surface the activity of nitrogen, a_N, is given by:

$$a_N = K \frac{p_{NH_3}}{p_{H_2}^{3/2}} p_0^{1/2} \tag{7}$$

where K is the equilibrium constant of reaction, p_0 is the total pressure, and p_{NH_3} and p_{H_2} are the partial pressures of the ammonia and hydrogen gases respectively. On the basis of eq.(4),

$$K_n = \frac{p_{NH_3}}{p_{H_2}^{3/2}} \tag{8}$$

is defined as nitriding potential (K_n) measured in $p_a^{-1/2}$ or $atm^{-1/2}$.

Dissociation rate represents the percentage of ammonia dissociated into hydrogen and nitrogen based on Eq.(3) and is measured by using a burette in the furnace exhaust gas. Dissociation rate and nitriding potential can be easily converted to each other based on the equations described above.
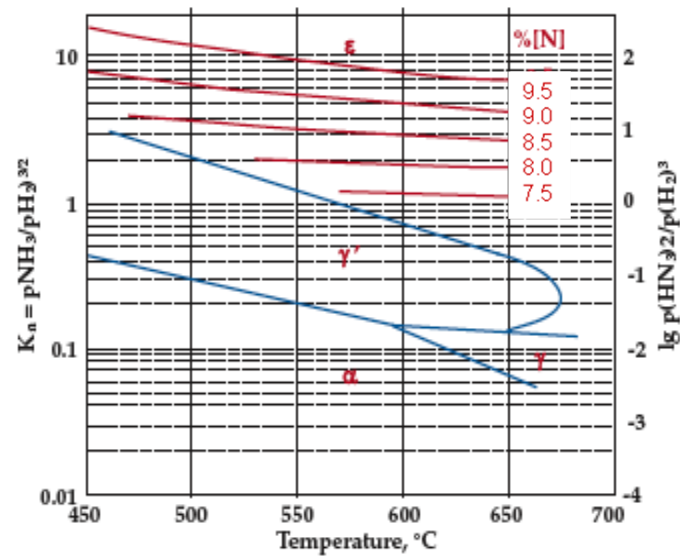
Figure 7. The experimental Lehrer diagram of the pure iron [20] with isoconcentration lines added [21]

The state of the art for controlling the nitriding process is to define the composition and phase distribution at the surface of the steel by measuring and controlling the nitriding potential. The widely used Lehrer diagram for pure iron is presented in Figure 7, showing the relationship between the phases formed under local equilibrium and the nitriding potential as a function of temperature for pure iron. However, the Lehrer diagrams for alloy steels do not exist. Application of the pure iron Lehrer diagram can lead to incorrect prediction of the phases at the steel surface.

1.4.Process modeling

1.4.1. Previous effort on the modeling of gas carburizing process

Carburizing process involves diffusing carbon into a low carbon steel to form a high carbon steel surface[22].In gas carburizing, carbon transfers from gaseous atmosphere through the boundary layer, reacts with the steel surface in vapor-solid interface and then diffuses into the bulk of the material (Figure 8).
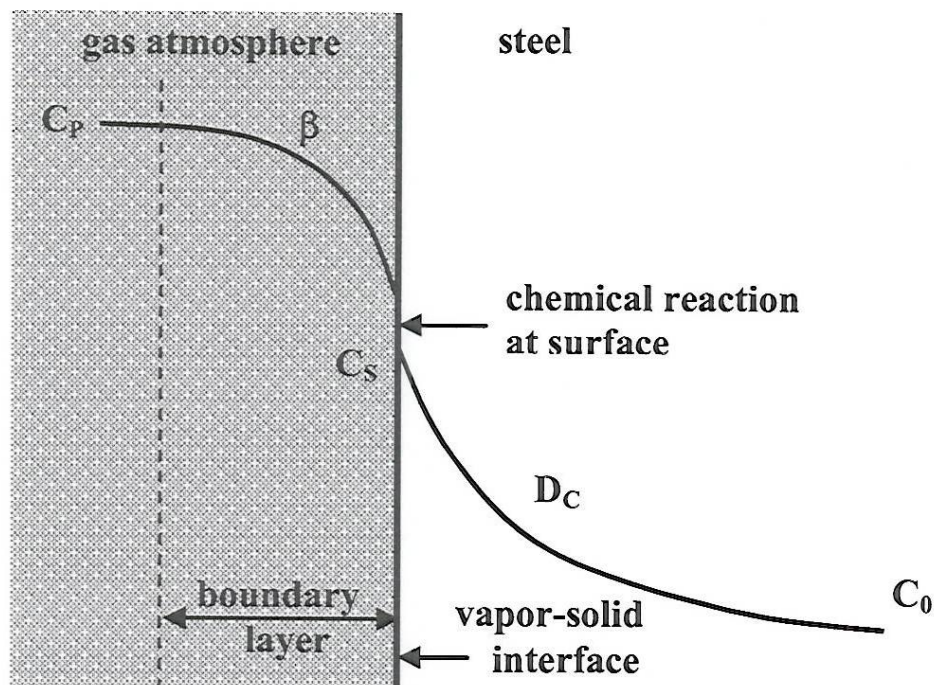
Figure 8. The schematic representation of carbon transportation in carburizing [23]

During gas carburizing process, there are several controllable parameters which can be adjusted to meet the customer's specifications, including carbon potential (C_P) in the atmosphere, temperature and time. The maximum carburization rate can be achieved by controlling the rate of carbon transfer from the atmosphere and the rate of carbon

diffusion into the steel. Carburizing process performance strongly depends on the process parameters, as well as furnace types, materials characteristics, atmosphere etc. All of these factors contribute to the mass transfer coefficient (β) which relates the mass transfer rate, mass transfer area, and carbon concentration gradient as driving force. So the mass transfer coefficient and the coefficient of carbon diffusion in steel are the parameters that control the process. [24-26]

The total quantity of the carbon which diffused through the surface can be estimated by integrating the carbon concentration profile over the depth of the carburized layer. Furthermore, differentiation of the total weight gain by the carburizing time yields the total flux of carbon atoms through the vapor/solid interface as presented in equation (9). [27]

$$J = \frac{\partial}{\partial t}\left(\frac{\Delta M}{A}\right) \tag{9}$$

where J is the carbon flux (g/cm^2*s), ΔM is the total weight gain (g), A is the surface area (cm^2) and t is the carburizing time(s).

The flux in the atmosphere boundary layer is proportional to the difference between the surface carbon concentration in the steel and the atmosphere carburizing potential, the mass transfer coefficient can be presented as follows [28] :

$$\beta = \frac{\frac{\partial}{\partial t}\int_{x_\infty}^{x_0} C(x,t)\,dx}{\left(C_P - C_S\right)} = \frac{\left(\Delta M/A\right)}{t\left(C_P - C_S\right)} \tag{10}$$

where β is the mass transfer coefficient (cm/s), C_s is the surface carbon concentration in the steel, and C_P is the atmosphere carburizing potential.

Gas carburizing process is modeled [28] using a second-order parabolic partial differential equation (equation (11)) for carbon diffusion in steel and a set of boundary conditions (equation (10)) accounting for the mass transfer coefficient at the steel surface and kinetics of the interfacial reactions:

$$\frac{\partial C}{\partial t} = \frac{\partial}{\partial x}(D_C \frac{\partial C}{\partial x}) + u \cdot \frac{D_C}{r + ux} \cdot \frac{\partial C}{\partial x}$$

(11)

where u = -1 for convex surface, u = 0 for plane surface and u = 1 for concave surface, D_C is the coefficient of carbon diffusion in steel, r is radius of the curvature, x is distance from the surface.

1.4.2. Modeling of gas nitriding

Comparing with the gas carburizing modeling, the gas nitriding modeling is much more complicated due to the formation of nitrides. Therefore, the gas nitriding process model should consider the phase evolution during the nitriding process.

1.4.2.1. Kinetics of Nitriding

The phase diagrams show the equilibrium phase evolution during nitriding. However, the deviations from the equilibrium may occur during nitriding especially in the initial stage of the treatment. In practice, nitriding is a complex process which involves:

1) ammonia transfer from the atmosphere to the substrate surface,

2) surface chemical reactions including ammonia adsorption and dissociation and nitrogen absorption and desorption,

3) diffusion of the absorbed nitrogen atoms and growth of nitrides layers.

1.4.2.2. Nitride layer growth model on pure iron nitriding process

There has been ongoing effort on the simulation of the gas nitriding process since 1990s. And most of the successful work has been done to simulate the gas nitriding process of pure iron due to the limited thermodynamics and kinetics information available on the gas nitriding process of steels.

In nitrided iron, single-phase layers exist in the compound layer. The kinetics of diffusion-controlled growth of the nitride layers ε and γ'can be described by the shift of the interfaces (ε/γ' and γ'/α) between ε, γ', and α due to the differences on the fluxes of nitrogen arriving at the interfaces and the fluxes of nitrogen leaving from the interfaces.

The nitrogen concentrations on the interfaces between these layers can be defined from the binary Fe-N phase diagram when the local equilibrium is assumed at the interfaces [29] as shown in Figure 9.

According to Fick's first law, the fluxes differences at the interfaces can be described as the amount of nitrogen that diffuses through the interfaces within the time increment. Somers and Mittemeijer [30] successfully adopted this nitride layer growth model to derive the monolayer (γ') and bilayer (ε and γ') growth into the substrate for the pure iron nitriding process.
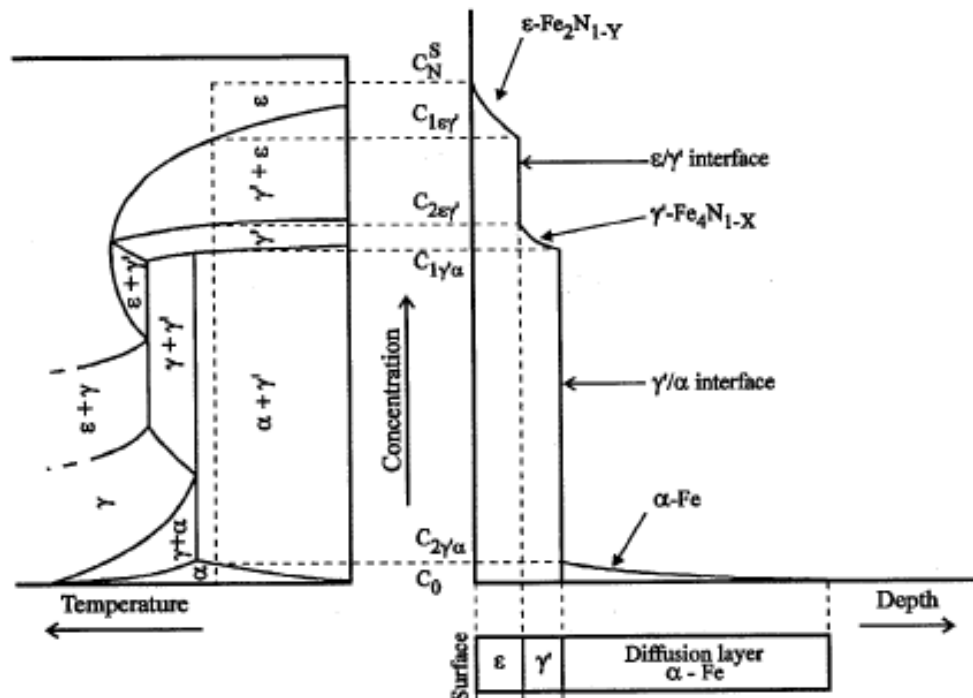
Figure 9. Relation between Fe-N phase diagram and concentration/ depth for growth of a bilayer ε-Fe$_2$N$_{1-x}$ and γ'-Fe$_4$N into a substrate α-Fe [29]

1.4.3. Nitrogen Diffusivity in Ferrite

Nitrogen diffusivity is one of the key kinetic parameters which defines not only the nitrogen diffusion in substrate but also the growth of the nitrides.

The diffusivity of C and N in α-Fe was studied by Silva and McLellan[31]. According to the experimental data they collected, the diffusivity of C and N at high temperature does not obey the classical formula:

$$lnD = lnD_0 - Q/kT \tag{12}$$

Instead,

$$lnD_C = -2.087 - \frac{1.197 \times 10^4}{T} + \frac{3.7 \times 10^5}{T^2} \tag{13}$$

and

$$lnD_N = -4.485 - \frac{0.9979 \times 10^4}{T} + \frac{1.4 \times 10^5}{T^2} \tag{14}$$

are more suitable.
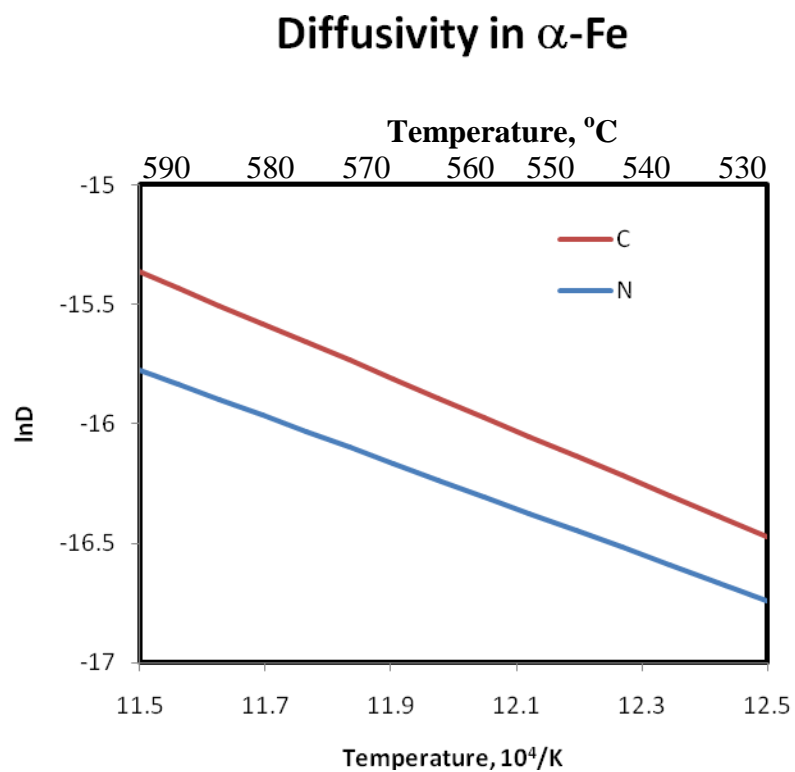
Figure 10. Plot of lnD vs. 1/T for the carbon and nitrogen in α-Fe

The relationship between the lnD and 1/T is plotted in Figure 10. It can be seen that the diffusivity of carbon in α-Fe is greater than diffusivity of nitrogen in α-Fe in the nitriding temperature range.

1.4.4. Case Depth

After the thermochemical surface treatment, the ferrous substrate surface layer which becomes substantially harder than the remaining material is called the case. When the case depth is discussed, the total case depth, effective case depth to 50 HRC, and case depth to 0.40 wt% N should be specified.

Effective case depth is the perpendicular distance from the surface of a hardened case to the deepest point at which a specified level of hardness is reached. The hardness criterion, except when otherwise specified, is 50 HRC. The effective case depth is typically about two-thirds to three-fourths the total case depth [32].

Total case depth may be defined as the perpendicular distance from the surface of a hardened or unhardened case to the point at which differences in chemical or physical properties of the case and core can no longer be distinguished. [32]

Table 1.Temperature factors for Harris equation [3]

Temperature		Temperature factor (K)
˚C	˚F	
460	865	0.00150
470	875	0.00155

475	885	0.00172
480	900	0.00195
500	930	0.00210
510	950	0.00217
515	960	0.00230
525	975	0.00243
540	1000	0.00262

F.E. Harris defined a formula to describe the effect of time on carburizing case depth which depends on the temperature[33]. This formula is also used in nitriding and as shown in the following formula, the effective case depth changes linearly with the square root of process time.

$$Case\ depth = K\sqrt{t} \tag{15}$$

where the case depth is in inches, t (time) is in hours, and K is the particular temperature factor which can be found in the Table 1.

1.5. Computational thermodynamics

In the current work, the thermodynamic simulations involved were calculated by the CALPHAD approach. CALPHAD is an acronym for the CALculation of PHAse Diagram. It is capable of predicting the phase behavior in multi-component systems. In this approach, the Gibbs energy of individual phases is modeled and the model parameters are collected in a thermodynamic database. Models for the Gibbs energy are

based on the crystal structures of the phases. CALPHAD has been under development since early 1970's. The development of CALPHAD techniques in the past three decades was discussed by Saunders and Miodownik [34].

1.5.1. Available thermodynamic database

TCFE is a database for Thermo-Calc that has been continuously developed and improved over the years. TCFE can also be used with other software from Thermo-Calc Software such as DICTRA, TC-PRISMA and Programming Interfaces. Typical applications for TCFE include Steel and Fe-alloy design and engineering.

TCFE can be used with satisfying results for several of different alloys e.g. stainless steels, high-speed steels, tool steels, HSLA steels, cast iron, corrosion-resistant high strength steels and more.

Before choosing the TCFE database, the accuracy and the limits of the database were investigated. The database is applicable for various types of steels/Fe-alloys with a Fe-minimum of 50wt%, and for alloying elements the recommended composition limits (in weight percent) are shown in Table 2.

Table 2 limits of TCFE database

Element	max	Element	max	Element	Max	Element	max
Al	5	Cu	5	Ni	20	Ti	3
B	Trace	Mg	Trace	O	Trace	V	15
C	7	Mn	20	P	Trace	W	15
Ca	Trace	Mo	10	S	Trace	Zr	10
Co	20	N	5	Si	5		
Cr	30	Nb	5	Ta	10		

The database has been based on complete reassessments of binary and many ternary systems; however, many intermediate compounds that do not occur in steels/Fe-alloys have been deleted from the database. Therefore, it is not suitable to calculate complete binary and ternary systems, but rather only in the iron-rich corner. Each parameter in the database has a reference to its origin.

The most important systems in the nitriding process, Fe-N binary system and Fe-C-N ternary system, were selected to examine the TCFE database accuracy. The Fe-N binary database was updated by Du et al. [35] based on the work by Frisk [36] with comparison with various Fe-N system experimental data [36-47]. The Fe-C-N ternary database was also updated by Du et al. based on their previous work [48] with comparison with various ternary system experimental data. [48-55]. Overall, both systems show very good agreement with experimental data.

Based on the above analysis, TCFE6 database were used to make all the calculations for present work, which were carried out using Thermo-Calc [56].

References

1   M. A. J. Somers, *Heat Treatment of Metals* 27, (2000) 92-102.

2   D. H. Herring, *Heat Treating Progress*, (2002) 17.

3   D. Pye, *Practical nitriding and ferritic nitrocarburizing*, ASM International, Materials Park, OH (2003).

4   H. Du, M. A. J. Somers, J. Agren, *Metallurgical and Materials Transactions a-Physical Metallurgy and Materials Science* 31, (2000) 195-211.

5   T. Bell *Gaseous and Plasma Nitrocarburizing*, ASM International, Materials Park, Ohio (1997)

6   T. Bell, Y. Sun, A. Suhadi, *Vacuum* 59, (2000) 14-23.

7   M. H. S. M. Hernandez, and E.S. Puchi-Cabrera, *Surf. Coat. Technol.* 202, (2008) 1935-1943.

8   M. P. F. M.J. Baldwin, S.C. Haydon, S. Kumar, G.A. Collins, K.T. Short, and J. Tendys, *Surf. Coat. Technol.* 98, (1998) 1187-1191.

9   G. B. McFadden, A. A. Wheeler, D. M. Anderson, *Physica D* 144, (2000) 154-168.

10   J. R. Davis *Surface Hardening of Steels-Understanding the Basics*, Davis & Associates, (2002)

11   A. S. M. Handbook *Alloy Phase Diagrams*, ASM, Metals Park, OH (1992)

12   J. S. L. A. J. Slycke, *Scand. J. Metal.* 17, (1988) 122.

13   E. J. Mittemeijer, W. T. M. Straver, P. F. Colijn, P. J. van der Schaaf, J. A. van der Hoeven, *Scr. Metall.* 14, (1980) 1189-1192.

14   L. Tatiana, *Phase transformations in interstitial Fe-N alloys*, (2005).

15   M. A. J. Somers, *HÃ¤rt.-Tech. Mitt.* 46, (1991) 375.

16   J. Ratajski, J. Tacikowski, M. A. J. Somers, *Surface Engineering* 19, (2003) 285-291.

17   T. Bell *Gaseous and Plasma Nitrocarburizing of Steels, Heat Treating*, ASM International, (1991)

18   K.-M. Winter *Gaseous Nitriding: In Theory and in Real Life*, United Process Controls, Heiningen, Germany (2009)

19   E. J. Mittemeijer, J. T. Slycke, *Surface Engineering* 12, (1996) 152-162

20   E. Lehrer, *Zeitschrift fuer Elektrochemie und Angewandte Physikalische Chemie* 36, (1930) 383.

21   P. Z. Maldzinski L., Kunze L., *Steel Research* 12, (1986) 645-649.

22   L. D. Liu, F. S. Chen, *Surface & Coatings Technology* 183, (2004) 233-238.

23   J. B. Dulcy, P.; Zimmermann, D.; Gantois, M., *La mettalurgia italiana* 4, (1999) 39-44.

24   P. Stolar, B. Prenosil, *Kovove Materialy-Metallic Materials* 22, (1984) 626-637.

25   M. Yan, Z. Liu, and G.Zu., *Materials Science Progress (in Chinese)* 6, (1992) 223-225.

26   B. A. Moiseev, Y.M. Brunzel, and L.A. Shvartsman, *Metal Science and Heat Treatment* 21, (1979) 437-442.

27   R. Collin, S. Gunnarson, and D.Thulin, *Journal of the Iron and Steel Institute* 210, (1972) 785-789.

28   O. Karabelchtchikova, R. D. Sisson, *Journal of Phase Equilibria and Diffusion* 27, (2006) 598-604.

29   L. Torchane, P. Bilger, J. Dulcy, M. Gantois, *Metallurgical and Materials Transactions a-Physical Metallurgy and Materials Science* 27, (1996) 1823-1835.

30   M. A. J. Somers, E. J. Mittemeijer, *Metallurgical and Materials Transactions a-Physical Metallurgy and Materials Science* 26, (1995) 57-74.

31   J. R. G. da Silva, R. B. McLellan, *Materials Science and Engineering* 26, (1976) 83-87.

32   A. S. M. handbook *Methods of Measuring Case Depth in Steels, Heat Teatment*, ASM International, Materials Park, OH (1991)

33   F. E. Harris, *Metal Progress*, (1943) 265-272.

34   N. Saunders, A. P. Miodownik, *CALPHAD (Calculation of Phase Diagrams): A Comprehensive Guide*, Pergamon, Oxford ; New York (1998).

35   H. Du, *Journal of Phase Equilibria* 14, (1993) 682-693.

36   K. Frisk, *Calphad* 15, (1991) 79-106.

37   H. J. Grabke, *Berichte der Bunsengesellschaft für physikalische Chemie* 73, (1969) 596-601.

38   Z. Przylecki, L. Maldzinski *Carbides, nitrides and borides*, (1987)

39   M. A. J. Somers, E. J. Mittemeijer, *Metallurgical Transactions a-Physical Metallurgy and Materials Science* 21, (1990) 189-204.

40   H. A. Wriedt, *TRANS MET SOC AIME* 245, (1969) 43-46.

41   K. H. Jack, *Proceedings of the Royal Society of London. Series A. Mathematical and Physical Sciences* 208, (1951) 200-215.

42   L. J. Dijkstra, *Journal of Metals* 1, (1949) 252.

43   N. S. Corney, E. T. Ihrkdogan, *Journal of the Iron and Steel Institute* 18, (1955) 344-348.

44   W. Pitsch, E. Houdremont, *Ein Beitrag zum System Eisen-Stickstoff*, Verl. Stahleisen(1956).

45   R. Rawlings, D. Tambini, *Iron and Steel Institute* 184, (1956) 302.

46   L. Maldzinski, Y. Przylecki, J. Kunze, *Steel Res.* 57, (1986) 645-649.

47   E. Lehrer, *Zeitschrift für Elektrochemie und angewandte physikalische Chemie* 36, (1930) 383-392.

48   H. Du, M. Hillert, *Zeitschrift fur Metallkunde* 82, (1991) 310-316.

49   M. Somers, *Z. Metallkd.* 81, (1990) 33-43.

50   F. K. Naumann, G. Langenscheid, *Archiv Eisenhüttenwesen* 36, (1965)

51   M. A. J. Somers, E. J. Mittemeijer, *Surface engineering* 3, (1987) 123-137.

52   L. C. Browning, T. W. DeWitt, P. H. Emmett, *Journal of the American Chemical Society* 72, (1950) 4211-4217.

53   A. F. Guillermet, G. Grimvall, *Physical Review B* 40, (1989) 10582.

54   A. F. Guillermet, G. Grimvall, *Journal of Physics and Chemistry of Solids* 53, (1992) 105-125.

55   A. Wells, T. Bell, *Heat Treat. Met.* 10, (1983) 39-44.

56   J. O. Andersson, T. Helander, L. H. Hoglund, P. F. Shi, B. Sundman, *Calphad* 26, (2002) 273-312.

Chapter 3

PUBLICATIONS

This section summarizes the results for the outlined theoretical work and experimental investigations. The section is structured as a collection of papers – each presented as a subsection outlined in the research plan.

Paper #1: Intelligent Heat Treating: Simulation of the Ferritic Nitriding Process – Database Development (Proc. MS&T 2010, Houston, TX, pp. 957-968.)

Abstract

Heat treaters need an effective simulation tool to predict the nitriding performance for a wide variety of steels. This tool is needed not only to predict the hardness and nitrogen concentration profiles as a function of process parameters but also to optimize the process in terms of cycle time and cost. To develop a tool, it is necessary to predict the phase evolution in the hardened case during nitriding. In the present work, thermodynamic calculations and experimental work have been completed to help determine the effects of process parameters (i.e. temperature and nitriding potential as well as the starting steel microstructure and composition) on the nitriding process. The thermodynamic calculations show that γ' - Fe_4N should coexist with ε - $Fe_{2-3}(C, N)$ phase in the compound layer, while only Fe_4N is found in the compound layer by X-ray

diffraction. However, the SEM results show the existence of two phases in the compound layer and the TEM results at the interface between the compound layer and the diffusion zone verify the coexistence of γ' - Fe_4N and ε - $Fe_{2-3}(C, N)$ phases. The nitriding characteristics were also examined in terms of weight gain, microhardness, and nitrogen concentration profiles. These data will be used to develop the simulation tool to optimize and control the nitriding process.

1.   Introduction

Nitriding is a thermochemical surface treatment in which nitrogen is transferred from an ammonia atmosphere into the steel at temperatures within the ferrite and carbide phase field [1-3], at approximately 570 °C [4].

After nitriding, a compound layer and an underlying diffusion zone (i.e. case) are formed at the surface of the steel. The compound layer, also known as the white layer, consists predominantly of ε - $Fe_{2-3}(C, N)$ and/or γ' - Fe_4N phases [5]. For pure iron, in the diffusion zone beneath the compound layer, nitrogen from the atmosphere dissolves interstitially in the ferrite lattice at the nitriding temperature. For the steel with tempered martensite (ferrite + Fe_3C and other carbides), the nitrogen also dissolves interstitially with ferrite (or low carbon martensite) and reacts with the carbides to form carbonitrides. For the steel containing nitride forming elements, alloy nitride precipitates are also formed in the diffusion zone [2, 6, 7].

The compound layer has greatly improved wear and corrosion resistance [5]. The hardened diffusion zone is responsible for a considerable enhancement of the fatigue

endurance. Furthermore, being a low temperature process (performed in the ferrite regime on Fe-N-C phase diagram, quenching is not require), nitriding minimizes distortion and deformation of the heat treated parts [2]. Therefore, nitriding is an important surface heat treatment for ferritic steels and can be widely used.

This paper presents experimental results and thermodynamic calculation results for nitrided AISI 1045 and AISI 4140 steels, which will pave the way to the further model development as well as optimization and control of the nitriding process.

2. Computational Thermodynamics (CALPHAD)

The thermodynamic simulations were carried out via the CALPHAD methodology. CALPHAD is an acronym for the CALculation of PHAse Diagram. It is capable of predicting the phase behavior in multi-component systems. In this approach, the Gibbs free energy of individual phases is modeled and the model parameters are collected in a thermodynamic database. Models for the Gibbs free energy are based on the crystal structures of the phases. CALPHAD has been under development since early 1970's. The development of CALPHAD techniques in the past three decades was discussed by Saunders and Miodownik [8]. TCFE4 database were used to make all the calculations for AISI 1045 and AISI 4140, which were carried out using the Thermo-Calc software [9].

3.   **Experimental Procedure**

   3.1.Materials and nitriding

   The AISI 1045 and AISI 4140 bars used in the experimental study were
purchased from Peterson Steel Corporation and their compositions determined by optical
emission spectroscopy (OES) are listed in Table 3 and in Table 4.

Table 3 Composition of AISI 1045 in wt.%

C	Mn	P	S
0.437	0.71	0.01	0.028

Table 4 Composition of AISI 4140 in wt.%

C	Mn	P	S	Si	Cr	Mo
0.399	0.91	0.01	0.029	0.266	0.88	0.166

   Before nitriding, the cylindrical steel bars were heat treated to harden the core by
heating to $843^{o}C$ for one and a half hours in Endothermic gas at 0.4% carbon potential,
followed by quenching in agitated $54^{o}C$ mineral oil. The parts were washed in hot water
and tempered in air at $579^{o}C$ for 3 hours (Bodycote, Worcester, MA, USA). Hardness
after core hardening was measured by Wilson Rockwell Hardness Tester. The Rockwell
scale characterizes the indentation hardness of steel through the depth of penetration of
an indenter, loaded on a sample and compared to the penetration in some reference
material. In the current work, the HRc was measured 5 times for individual steel. The
average HRc is 36.8 for AISI 4140 and 24.0 for AISI 1045.

The bars were machined into disks of 3.175 cm diameter and 1 cm thick with a 2mm diameter hole near the edge. The disks were washed with alcohol prior to the nitriding process. A standard two - stage industrial nitriding process was used in the current work. During the first stage, nitriding was carried out using ammonia gas with a dissociation rate of 24~28% at 527$^\text{o}$C for 10 hours. The temperature was then raised to 548$^\text{o}$C for 50 hours with a dissociation rate of 79%~82%. Dissociation rate is measured by using a burette in the furnace exhaust gas to determine the percentage of ammonia dissociation into hydrogen and nitrogen.

3.2.Characterization

The process characteristics of nitriding were evaluated by documenting weight gain, microhardness, and nitrogen concentration profiles. Laboratory scales sensitive to 0.01mg were used for weight gain measurements. Vickers hardness test was used to measure the cross section microhardness for the steels. Shimadzu HMV-2000 Micro Hardness Tester was used in the test with a 200gf load and 15s loading time. Nitrogen concentration profiles were obtained by Spectro MaXx LMM14 optical emission spectroscopy (OES) analyzer. The upper limitation of accurate nitrogen measurement is approximately 0.4wt.%. Extrapolation is made for samples with higher nitrogen concentrations. XRD and TEM analysis are also used to identify the phases in the samples. Focused ion beam (FIB) in-situ lift-out (INLO) technique was employed to prepare site-specific TEM specimen. Detailed information on FIB-INLO has been reported previously [10-11]. TEM/STEM using FEI/Tecnai F30 equipped with high angle

annular dark field (HAADF) was employed for phase identification by selected area electron diffraction (SAED).

4.   Results and Discussion

4.1. Thermo-Calc calculation results

Thermodynamic calculations using Thermo-Calc were completed to determine the isopleths of AISI 1045 and AISI 4140 as function of temperature and nitrogen concentration. The results of the analysis are presented in Figure 11 and Figure 12. Both alloys show that the HCP (ε - $Fe_{2\text{-}3}$(C, N)) becomes stable with increasing nitrogen concentration. The Fe_4N (γ') becomes stable when the nitrogen concentration is increased to more than 2wt.%. Figure 13 and Figure 14 show the mole fraction of phases vs. weight percentage of nitrogen for AISI 1045 and AISI 4140 at 548°C. The nitrogen concentration in the steel before nitriding process is zero. The alloys consists of 2 phases: BCC (α) + cementite (Fe_3C) in AISI 1045 and 3 phases: BCC + cementite (Fe_3C) + FCC (γ) in AISI 4140. The existence of γ phase in AISI 4140 is due to the stabilizing effect of chromium.
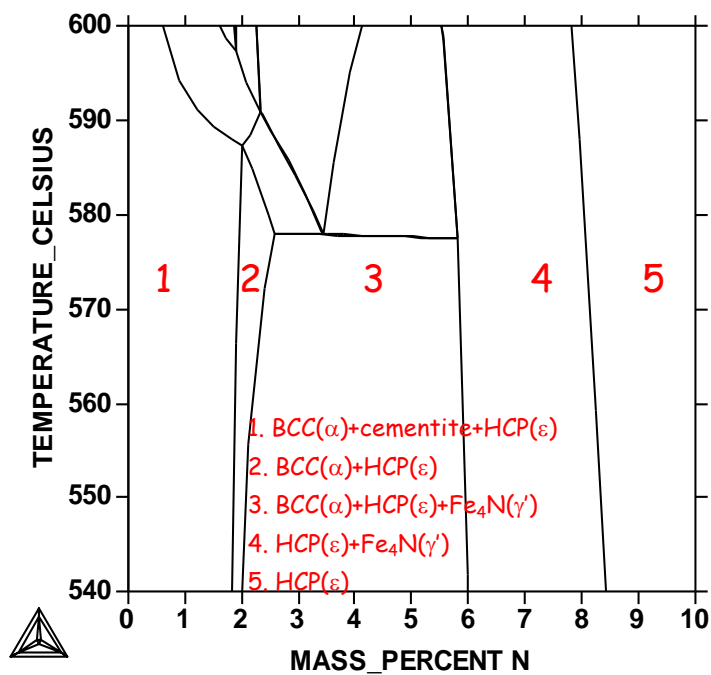
Figure 11 Isopleth of temperature vs. nitrogen concentration for AISI 1045.
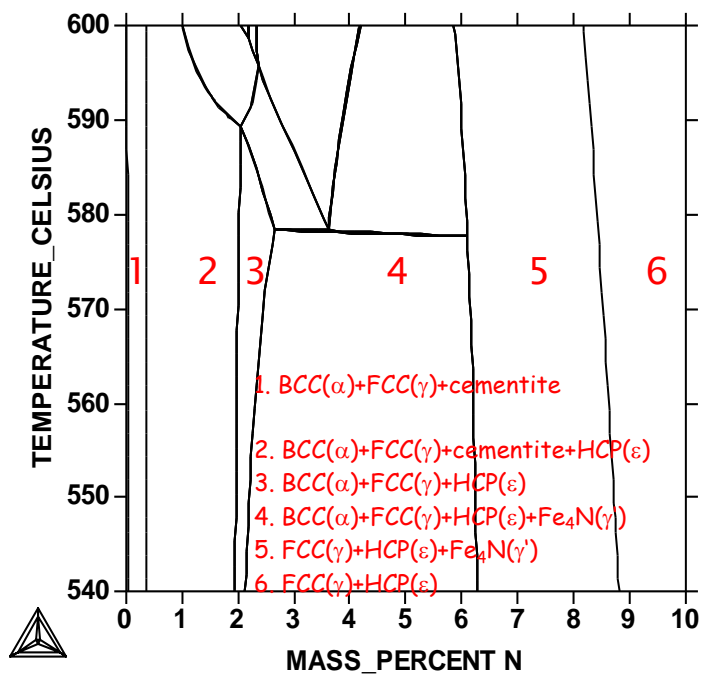
Figure 12 Isopleth of temperature vs. nitrogen concentration for AISI 4140.
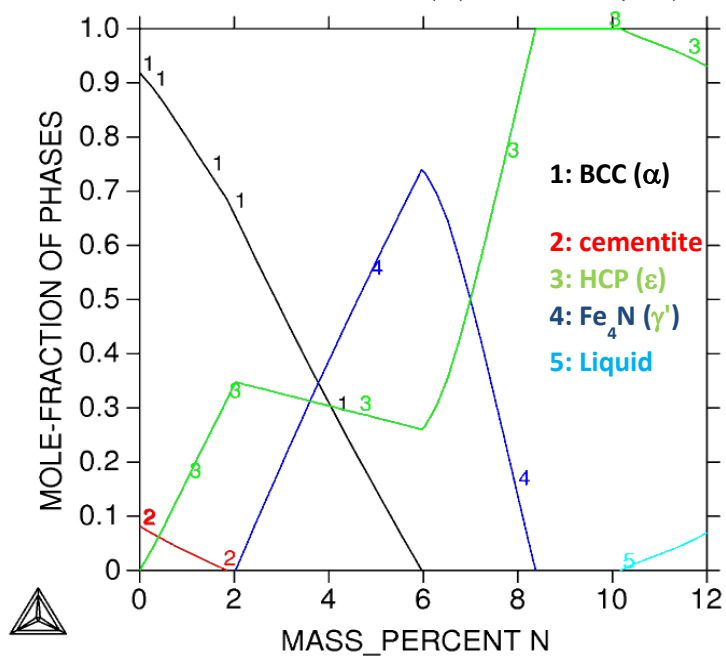
Figure 13 Phase evolution as a function of nitrogen content for AISI 1045 at 548°C
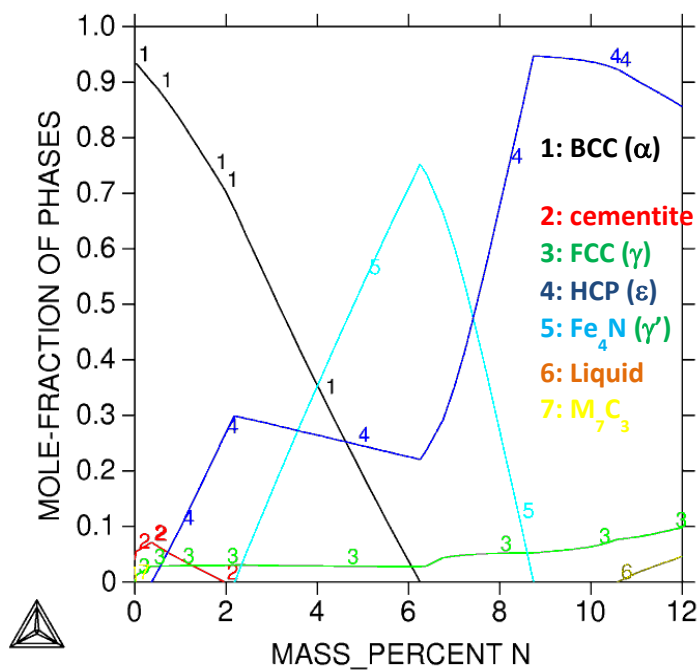
Figure 14 Phase evolution as a function of nitrogen content for AISI 4140 at 548°C

Assuming local equilibrium, it should be observed that Fe_3C and BCC ferrite gradually decompose from the core of the sample to the surface as nitrogen absorbed. ε - $Fe_{2-3}(C, N)$ will increase with the nitrogen concentration. When the nitrogen concentration is greater than 2wt.%, γ' - Fe_4N will form and coexist with ε - $Fe_{2-3}(C, N)$ from 2wt.% to 8wt.%N.

4.2. Experimental results

4.2.1. Optical microscopy

Figure 15 presents the optical photomicrographs of AISI 1045 and 4140 after the nitriding process. There is a compound layer formed on the surface for both steels. The average thicknesses are 17.0μm for AISI 1045 and 18.6μm for AISI 4140.
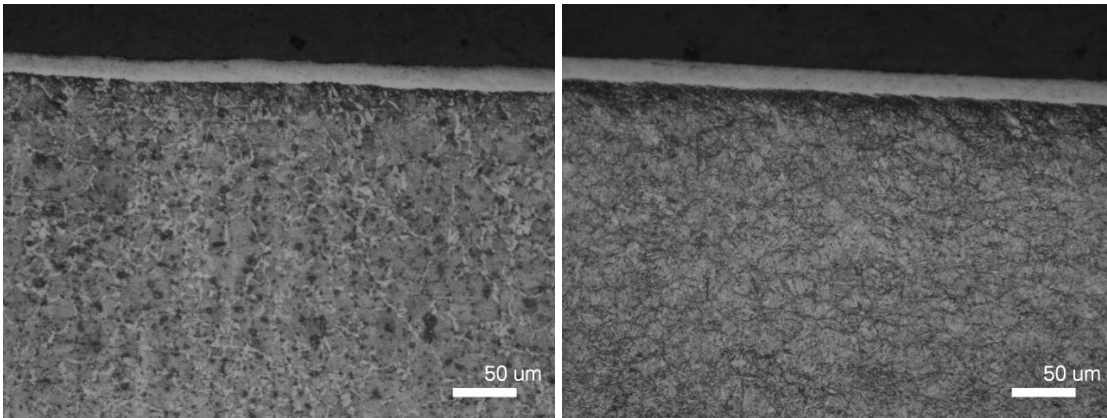
Figure 15 Optical microscopy of the cross section of the AISI 1045 (left) and AISI 4140 (right) after the nitriding process, etched with 2% nital solution

4.2.2. The weight gain and average flux

The weight gain from the nitriding process was calculated based on the measurement of the individual weight of each disk before and after the nitriding process. The average flux is thus calculated from the following equation:

$$J = \frac{1}{t} \cdot \left(\frac{\Delta M}{A} \right) \tag{1}$$

where J is the average flux, $\frac{\Delta M}{A}$ is weight gain per unit surface area, and t is the nitriding time. Figure 16 presents the average flux of AISI 1045 and AISI 4140 for 10 different samples respectively.
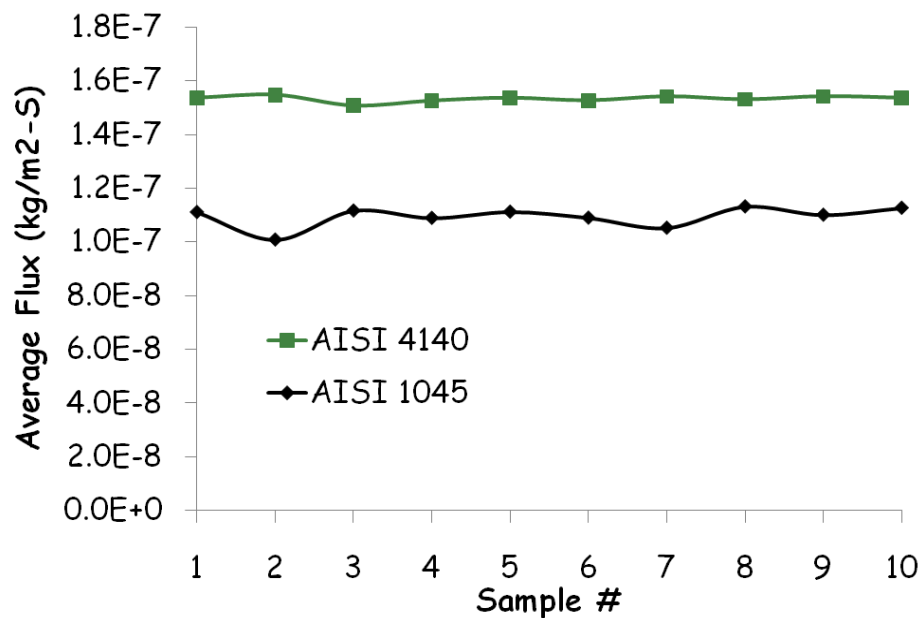
Figure 16 Average flux of AISI 1045 and AISI 4140 after nitriding process

Figure 16 presents that the average flux of AISI 4140 after nitriding is larger than that of AISI 1045. This difference in flux may be a result of the difference in the initial microstructure. The AISI 1045 microstructure consists of ferrite and pearlite, while the AISI 4140 microstructure is tempered martensite. In addition, Figure 13 and Figure 14 present that in AISI 4140, chromium and nitrogen stabilized the Austenite (γ) phase. The solubility of nitrogen in γ is one hundred times that of ferrite. Further work will determine if the flux difference is due to the existence of γ phase in AISI 4140.

4.2.3. Microhardness and nitrogen concentration

The microhardness for the cross section of AISI 1045 and AISI 4140 samples were measured to document the hardness change from the surface layer to the bulk. The measurements started at 50μm depth from the edge with an increment of 100μm per measurement afterwards.

Nitrogen concentrations were measured using an OES and were taken at four different locations on the surface of each layer. Layers of metal were removed and measurements were taken at each layer.

The microhardness and the weight percentage of nitrogen vs. depth from surface were both plotted for AISI 1045 and AISI 4140 as shown in Figure 17 and Figure 18, respectively. There are excellent correlations between the nitrogen concentration and the microhardness in both cases.
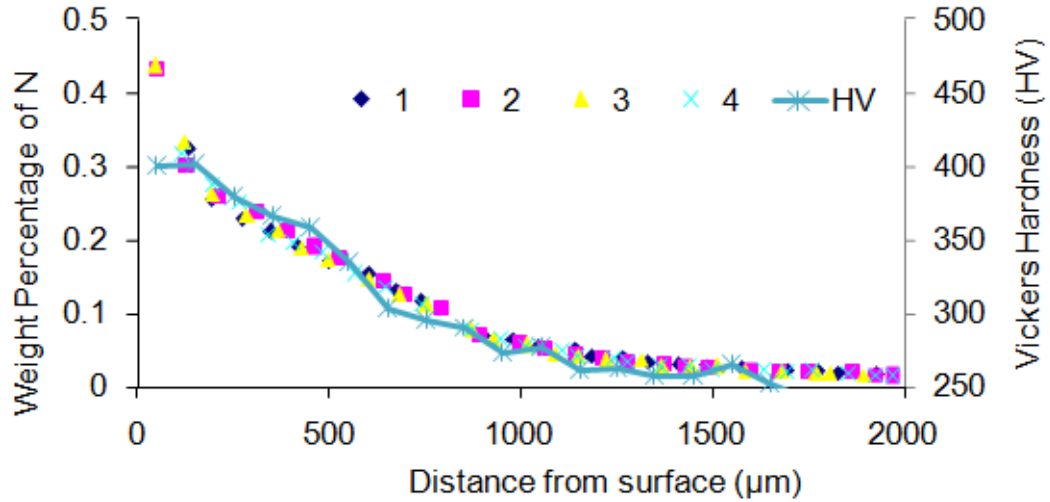
Figure 17 Weight percentage of nitrogen vs. depth from surface and Vickers hardness vs. depth from surface for AISI 1045. The weight percentages of nitrogen were measured by OES for four different locations.
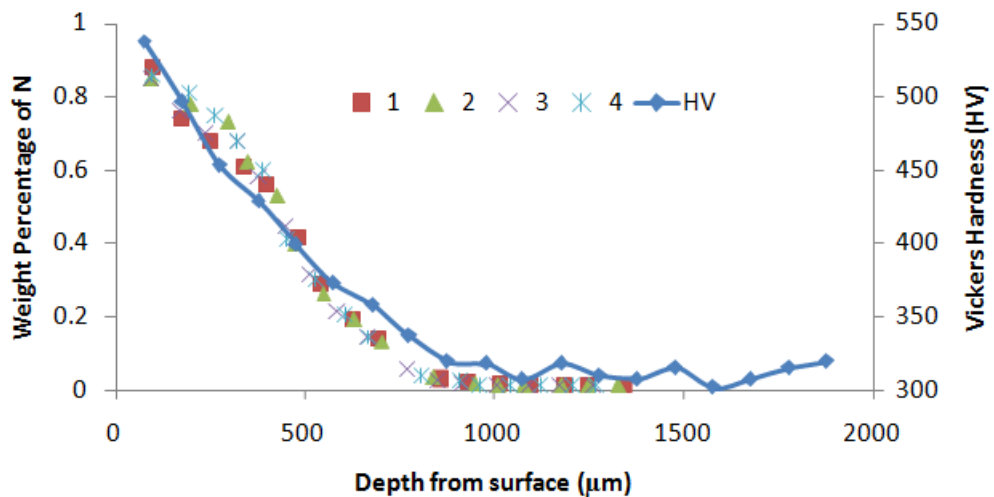
Figure 18 Weight percentage of nitrogen vs. depth from surface and Vickers hardness vs. depth from surface for AISI 4140. The weight percentages of nitrogen were measured by OES for four different locations.

4.2.4. Surface XRD analysis

The surface XRD analysis was conducted to indentify the phases near the surface. As shown from Figure 19 and Figure 20, only Fe_4N was detected for both AISI 1045 and AISI 4140. Combined with the observations from optical microscopy presented in Figure 15, it may appear that Fe_4N is the only phase in the compound layer of both steels. However, based on the thermodynamic prediction, both γ' - Fe_4N and ε - $Fe_{2-3}(C, N)$ phases should be observed.
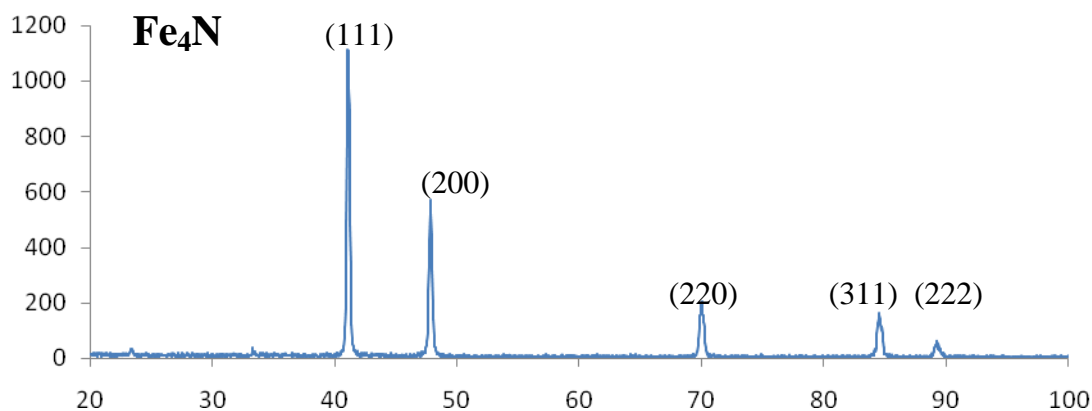
Figure 19 XRD spectrum of the surface scan for AISI 1045 after the nitriding process
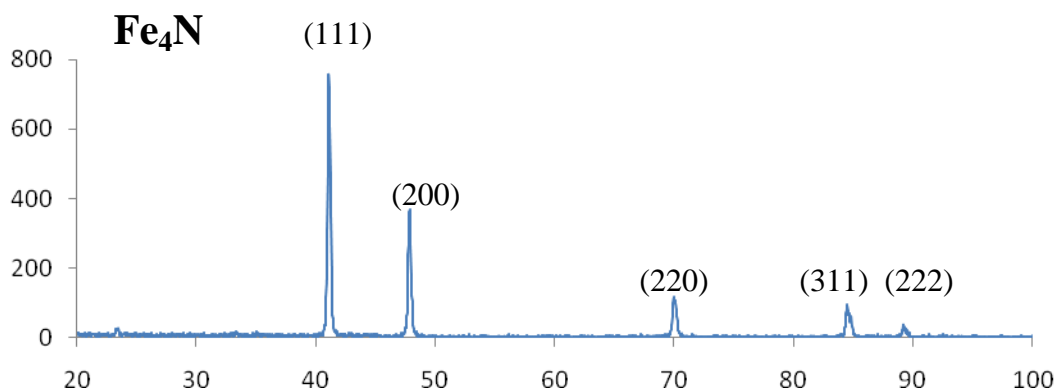
Figure 20 XRD spectrum of the surface scan for AISI 4140 after the nitriding process

4.2.5. SEM analyses
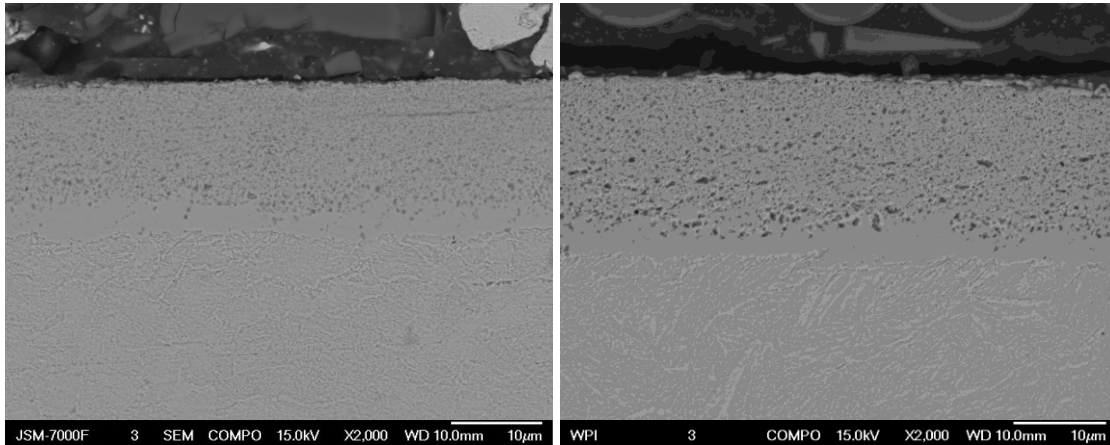
Figure 21 The SEM backscatter micrographs of the surface of the nitrided AISI 1045 (left) and AISI 4140 (right)

SEM analysis was performed to determine if any other phases exist in the compound layer. Figure 21 presents the SEM backscatter micrographs of the cross sections of the nitrided AISI 1045 and AISI 4140. It can be seen that the compound layer actually consists of two layers. The inner layer is mainly composed of the light phase. The outer layer has light areas and dark areas. The typical size of the dark areas is less than 1μm. The dark areas appear to be a very fine secondary phase.

4.2.6. TEM analysis

The discrepancy between surface XRD analysis and the SEM analysis may due to the fine size or the small volume fraction of second phase. TEM analysis was performed to observe the phase development in the nitrided case for AISI 1045 and AISI 4140.

Figure 22 presents the three distinct regions for the nitrided AISI 1045. Regions A and B corresponds to the two layers in the compound layer and region C corresponds to

the diffusion zone. Region A consists of two phases, γ' - Fe_4N (the light phase) and ε - $Fe_{2-3}(C, N)$ (the dark phase). Region B is mainly dominated by γ' - Fe_4N. In region C martensite and Fe_3C are found. The γ' - Fe_4N and ε - $Fe_{2-3}(C, N)$ phases were identified by SAED. Similar analysis was done for the AISI 4140 sample as shown in Figure 23. There are also three distinct regions in nitrided AISI 4140. Based on SAED, three different phases, γ' - Fe_4N, ε - $Fe_{2-3}(C, N)$ and Fe_7C_3 were found in region A, γ' - Fe_4N and Fe_7C_3 are found in region B, and martensite is the only phase found in region C. The diameter of the ε phase is less than 500nm as shown in Figure 22 and Figure 23. TEM results are in good agreement with the calculated results that γ' - Fe_4N and ε - $Fe_{2-3}(C, N)$ coexist in the compound layer.
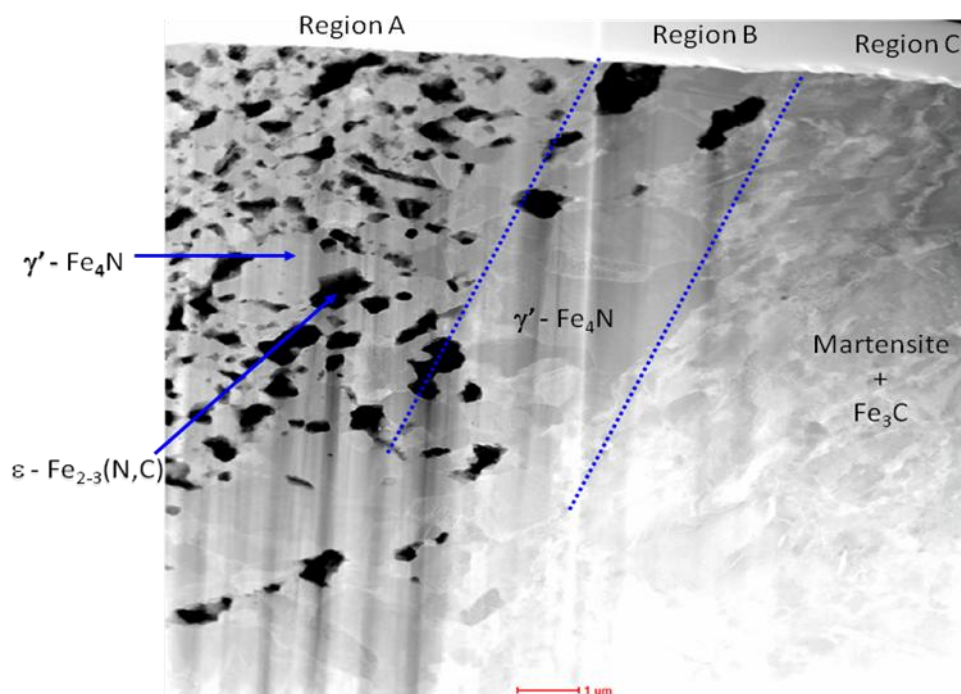
Figure 22. High angle annular dark field TEM micrograph from the nitrided case of nitrided AISI 1045
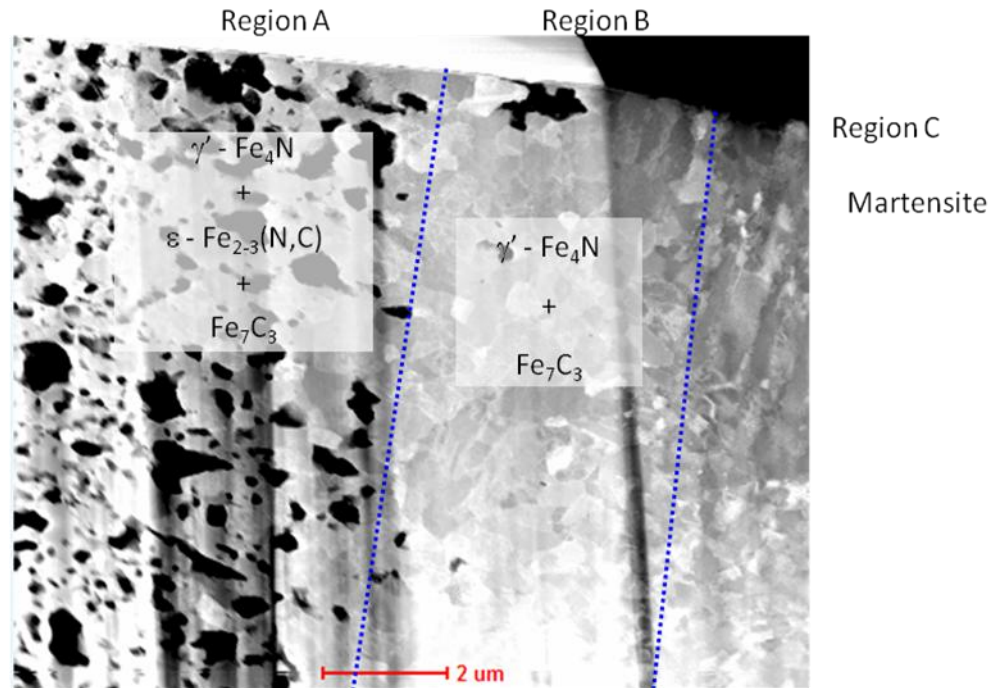
Figure 23. High angle annular dark field TEM micrograph from the nitrided case of nitrided AISI 4140

5. Conclusions

The phase and microstructural development during nitriding process of AISI 1045 and AISI 4140 has been investigated by computational thermodynamics and experimental investigations.

- Based on thermodynamic calculation results, ε - $Fe_{2-3}(C, N)$ phase becomes stable with the increase of nitrogen concentration and γ' - Fe_4N becomes the dominate phase with high nitrogen concentration. γ' - Fe_4N should coexist with ε - $Fe_{2-3}(C, N)$ for both alloys.

- The nitrided AISI 1045 and AISI 4140 samples were analyzed with a variety of characterization tools, including optical microscopy, OES, XRD, SEM, and TEM. The nitrogen concentration decreases monotonically from the surface through the diffusion zone for both alloys. The compound layer consisted of two layers; the outer layer contains γ' - Fe_4N and ε - $Fe_{2-3}(C, N)$ while in the inner layer is mostly Fe_4N.

- TEM analysis using HAADF and SAED demonstrated that the γ' - Fe_4N coexists with ε - $Fe_{2-3}(C, N)$ in the compound layer. This is consistent with the predictions by the CALPHAD approach.

Acknowledgement

References

[1] M. A. J. Somers, Thermodynamics, Kinetics and Microstructural Evolution of the Compound Layer; A Comparison of the States of Knowledge of Nitriding and Nitrocarburizing, *Heat Treatment of Metals*, Vol 27,Issue 4, 2000, pp. 92-102.

[2] D. Pye, Practical nitriding and ferritic nitrocarburizing, *ASM International*, Materials Park, OH, 2003.

[3] D. H. Herring, Comparing Carbonitriding and Nitrocarburizing, *Heat Treating Progress*, 2002, pp. 17.

[4] T. Bell, Gaseous and Plasma Nitrocarburizing of Steels, Heat Treating, *ASM Handbook, ASM International,* Vol. 4, 1991.

[5] H. Du, M. A. J. Somers, J. Agren, Microstructural and Compositional Evolution of Compound Layers during Gaseous Nitrocarburizing, *Metall Mater Trans. A*, Vol 31A, Issue 1, 2000, pp. 195-211A.

[6] T. Bell, Y. Sun, A. Suhadi, Environmental and Technical Aspects of Plasma Nitrocarburising, *Vacuum*, Vol 59, Issue 1, 2000, pp. 14-23.

[7] T. Bell, Gaseous and Plasma Nitrocarburizing, *ASM Handbook, ASM International*, Materials Park, Ohio, Vol. 4, 1997, pp. 425.

[8] N. Saunders, A. P. Miodownik, CALPHAD (Calculation of Phase Diagrams): A Comprehensive Guide (Pergamon, Oxford ; New York), 1998.

[9] J. O. Andersson, T. Helander, L. H. Hoglund, P. F. Shi and B. Sundman, Thermo-Calc & DICTRA, computational tools for materials science, Calphad, 26, 2002, pp. 273-312.

[10] K. Gamo, Nucl Instrum Meth B, 121, 1997, pp. 464-469.

[11] T. Kamino, T. Yaguchi, T. Ohnishi, K. Umemura and S. Tomimatsu., Microsc Microanal, 6, 2000, pp. 510.

Paper 2:Simulation of the Ferritic Nitriding Process (International Heat Treatment and Surface Engineering, vol.5 No.3, 2011, pp. 122-126.)

Abstract

The Lehrer diagram of pure iron is widely used to select the nitriding process of alloy steels. In the present work, the Lehrer diagram of AISI 4140 was determined for the first time by computational thermodynamics. It is demonstrated that the Lehrer diagram of AISI 4140 differs from that of pure iron significantly. Nitriding experiments for AISI 4140 were also carried out to verify the predictions from computational thermodynamics. The scanning electron microscopy (SEM) results show the existence of two phases in the compound layer and the transmission electron microscopy (TEM) results at the interface between the compound layer and the diffusion zone verified the coexistence of γ' - Fe_4N and ε - $Fe_{2-3}(C, N)$ phases. These experimental results agree well to the customized Lehrer diagram of AISI 4140 constructed from computational thermodynamics.

1. Introduction

Nitriding is a thermochemical surface treatment in which nitrogen is transferred from an ammonia atmosphere into the steel at temperatures within the ferrite and carbide phase field.[1-2] After nitriding, a compound layer and an underlying diffusion zone (i.e. case) are formed near the surface of the steel. The compound layer, also known as the

white layer, consists predominantly of ε - $Fe_{2-3}(C, N)$ and/or γ' - Fe_4N phases and can greatly improve wear and corrosion resistance.[3] The hardened diffusion zone is responsible for a considerable enhancement of the fatigue endurance. Furthermore, being a low temperature process, nitriding minimizes distortion and deformation of the heat treated parts.[2] Therefore, nitriding is an important surface heat treatment for ferritic steels with superior performance in a variety of applications.

The dissociation rate of ammonia or the nitriding potential is the most critical parameter to understand and control the nitriding process. Lehrer diagam[4] depicts the development of phase constituents in pure iron as functions of nitriding potential and temperature. In commerical practice, the experimental Lehrer diagram for pure iron is widely used to select the nitriding potential for alloy steels. Unfortunately, applying the Lehrer diagram of pure iron to the nitriding process of alloy steels can be misleading, because the phase equilibria for alloy steels can be significantly different from that of pure iron. Thus, it would be necessary to determine Lehrer diagrams for various alloy steels so that the appropriate nitriding potentials and process temperatures may be determined for the alloy steels.

In the present work, the Lehrer diagram of pure iron was first developed by computational thermodynamics and compared with the pure iron Lehrer diagram that was determined experimentally. More importantly, the Lehrer diagram of AISI 4140 steel was constructed to determine the composition and phases at the surface of the Nitrided AISI 4140. The thermodynamic calculation results were verified with experimental observations of nitriding using electron microscopy.

2. Nitriding potential and Dissociation rate

The chemical potential of nitrogen μ_N thermodynamically defines the nitridability of the nitriding atmosphere.[5] At thermodynamic equilibrium, the chemical potential in the steel surface ($\mu_{N,s}$) equals that in the nitriding atmosphere ($\frac{1}{2}\mu_{N_2,g}$). That means

$$\frac{1}{2}\mu_{N_2,g} = \mu_{N,s} \tag{1}$$

And the chemical potential of nitrogen in the steel can be related to nitrogen activity a_N by

$$\frac{1}{2}\mu^0_{N_2,g} + \frac{1}{2}RT\ln(\frac{p_{N_2}}{p^0_{N_2}}) = \mu^0_{N,s} + RT\ln a_N \tag{2}$$

where R is the gas constant, T is temperature, p_{N_2} is the partial pressure of nitrogen, $p^0_{N_2}$ is the partial pressure of nitrogen at the standard state.

Since the chemical potential of nitrogen is extremely low in N_2 and relatively high in ammonia, ammonia is used as the principal constituent of the nitriding atmosphere,[5] giving

$$NH_3 = [N] + \frac{3}{2}H_2 \tag{3}$$

where [N] represents nitrogen which is dissolved on the steel surface.
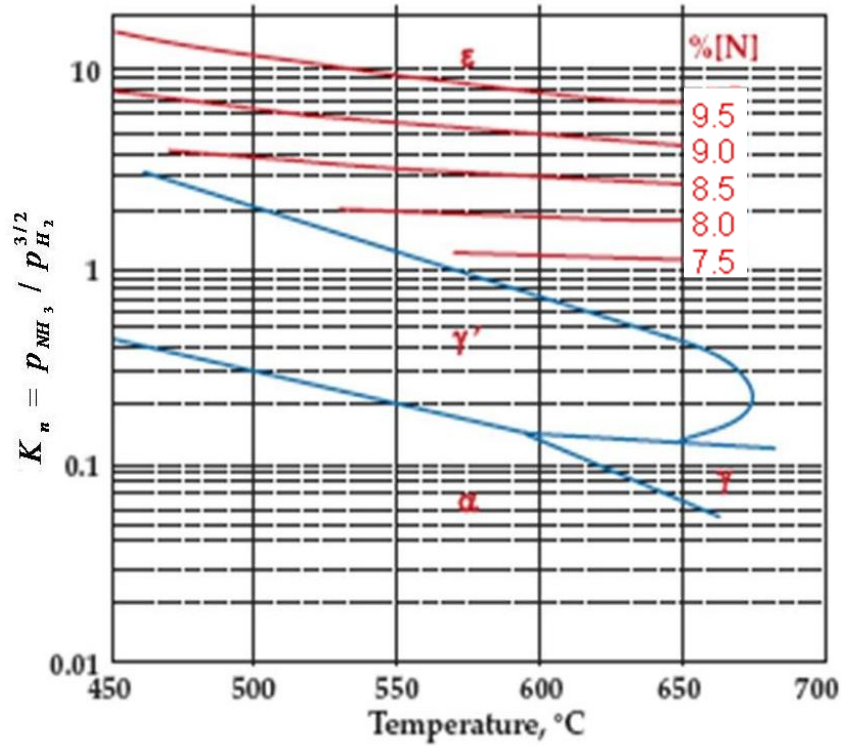
Figure 24. The experimental Lehrer diagram of the pure iron[4] with isoconcentration lines added.[6]

For local equilibrium between N in the gas phase and N in the steel surface the activity of nitrogen, a_N, is given by:

$$a_N = K \frac{p_{NH_3}}{p_{H_2}^{3/2}} p_0^{1/2} \tag{4}$$

where K is the equilibrium constant of reaction, p_0 is the total pressure, and p_{NH_3} and p_{H_2} are the partial pressures of the ammonia and hydrogen gases respectively. On the basis of eq.(4),

$$K_n = \frac{p_{NH_3}}{p_{H_2}^{3/2}}$$

(5)

is defined as nitriding potential (K_n) measured in $Pa^{-1/2}$ or $atm^{-1/2}$.

Dissociation rate represents the percentage of ammonia dissociated into hydrogen and nitrogen based on Eq.(3) and is measured by using a burette in the furnace exhaust gas. Dissociation rate and nitriding potential can be easily converted to each other based on the equations described above.

The state of the art for controlling the nitriding process is to define the composition and phase distribution at the surface of the steel by measuring and controlling the nitriding potential. The widely used Lehrer diagram for pure iron is presented in Figure 24, showing the relationship between the phases formed under local equilibrium and the nitriding potential as a function of temperature for pure iron. However, the Lehrer diagrams for alloy steels do not exist. Application of the pure iron Lehrer diagram can lead to incorrect prediction of the phases at the steel surface.

3. Computational Thermodynamics (CALPHAD)

The thermodynamic simulations were carried out via the CALPHAD methodology.[7] CALPHAD is an acronym for the CALculation of PHAse Diagram. It is capable of predicting the phase behavior in multi-component systems. In this approach, the Gibbs free energy of individual phases is modeled and the model parameters are collected in a thermodynamic database. Models for the Gibbs free energy

are based on the crystal structures of the phases. CALPHAD has been under development since early 1970's. The development of CALPHAD techniques in the past three decades was discussed by Saunders and Miodownik.[7] TCFE6 database were used to make all the calculations for pure iron and AISI 4140, which were carried out using the Thermo-Calc software. [8]

The Gibbs energy of fcc phase in the TCFE6 database was modeled to describe the regular austenite of Fe alloys and the M(C,N) carbonitrides since both share the same crystal structure. Two sublattice model $(M)_1(C,N,Va)_1$ was adopted for fcc according to its crystal structure. Metallic elements (M), such as Fe, Mn, Mo, and Cr, occupy the first sublattice that corresponds to the 4a site of fcc structure; while C, N, and vacancy occupy the second sublattice, that corresponds to the 4b site of fcc structure. If the 4b site is mainly occupied by vacancy, it is the austenite of Fe alloys. In the current isopleth, there are more than two fcc phases due to the immiscibility of the Gibbs energy description of the fcc phase in the TCFE6 database.

4. Experimental Procedure
4.1.   Materials and nitriding

The AISI 4140 bars used in the experimental study were purchased from Peterson Steel Corporation and their compositions determined by optical emission spectroscopy (OES) are reported in Table 5.

Before nitriding, the cylindrical steel bars were heat treated to harden the core[9] by heating to 843^oC for 1.5 hours in Endothermic gas at 0.4% carbon potential, followed

by quenching in agitated 54°C mineral oil, and were washed in hot water and tempered in air at 579°C for 3 hours (Bodycote, Worcester, MA, USA).

Table 5. Composition of AISI 4140 in wt.%

C	Mn	P	S	Si	Cr	Mo	Fe
0.399	0.91	0.01	0.029	0.266	0.88	0.166	Balance

The bars were machined into disks with a diameter of 3.175 cm and thickness of 1 cm. A hole of 2mm in diameter was drilled near the edge for holding the sample. The disks were washed with alcohol prior to the nitriding process. A standard two - stage industrial nitriding process was used for the current work. During the first stage, nitriding was carried out using ammonia gas with a dissociation rate of 24%~28% ($K_n \approx 9.24$) at 527°C for 10 hours. The temperature was then raised to 548°C for 50 hours with a dissociation rate of 79%~82% ($K_n \approx 0.43$).

4.2. Characterization

Scanning electron microscopy (SEM) was carried out in order to identify the distinctive layers that develop during nitriding of AISI 4140. Transmission electron microscopy (TEM) analysis was used to identify the phases in the samples. Focused ion beam (FIB) in-situ lift-out (INLO) technique was employed to prepare site-specific TEM specimen. Detailed information on FIB-INLO has been reported previously.[10-11] A FEI/Tecnai F30 equipped with high angle annular dark field (HAADF) was employed for

the TEM/STEM analysis.   Phases were identified using selected area electron diffraction (SAED), and convergent beam electron diffraction (CBED).

5. Results and Discussion
5.1.   Thermodynamic calculation results
5.1.1. Lehrer diagram of pure iron

By using the computational thermodynamics, the Lehrer diagram of pure iron was calculated. Figure 25 shows the calculated Lehrer diagram for pure iron, which is overall in good agreement with the experimental diagram presented in Figure 24. This comparison proved the utility of using thermodynamic database to calculate the customized Lehrer diagrams for alloy steels.
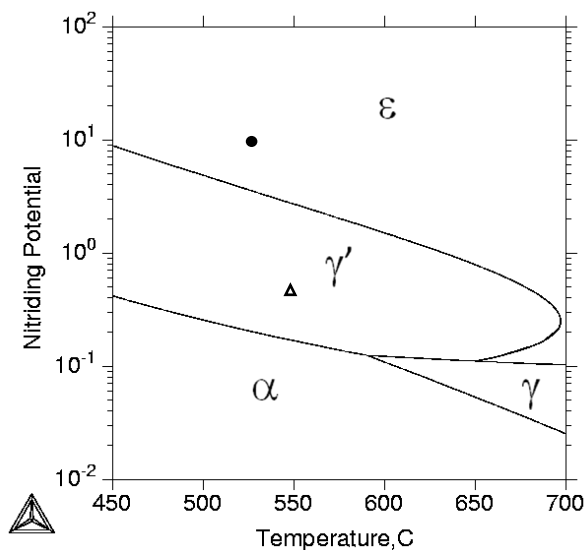
Figure 25. The calculated Lehrer diagram of the pure iron, ($\bullet$) represents nitriding condition in stage 1, i.e. K_n=9.24, T=527°C, (Δ) represents nitriding condition in stage 2, i.e. K_n=0.43, T=548°C

5.1.2. Lehrer diagram of AISI 4140

The isopleth of AISI 4140 is shown in Figure 26 (a) with the relevant phase regions labeled. The relationship between the mole fractions of phases vs. weight percentage of nitrogen for AISI 4140 at 548°C was also drawn as calculated in Figure 26 (b). The hcp (ε phase- $Fe_2(N,C)_{1-z}$) becomes stable with increasing nitrogen concentration and Fe_4N (γ' phase) becomes stable when the nitrogen concentration is increased to more than 2wt.%. Two different fcc phases, i.e. fcc1 (($Fe_{0.63}Cr_{0.36})_1(N_{0.75}Va_{0.25})_1$) and fcc2 (($Cr_{0.57}Fe_{0.25}Mo_{0.16})_1(N)_1$), are observed. The computational results clearly show the phase stabilities of fcc1 and fcc2, which indicate the addition of Cr, Mo, and N stabilize the fcc structure at low temperatures. However, the mole fractions of the two fcc phases are typically less than 3% and are very low compared to the other phases, which may lead to difficulties in their experimental detection.

(a)   (b)
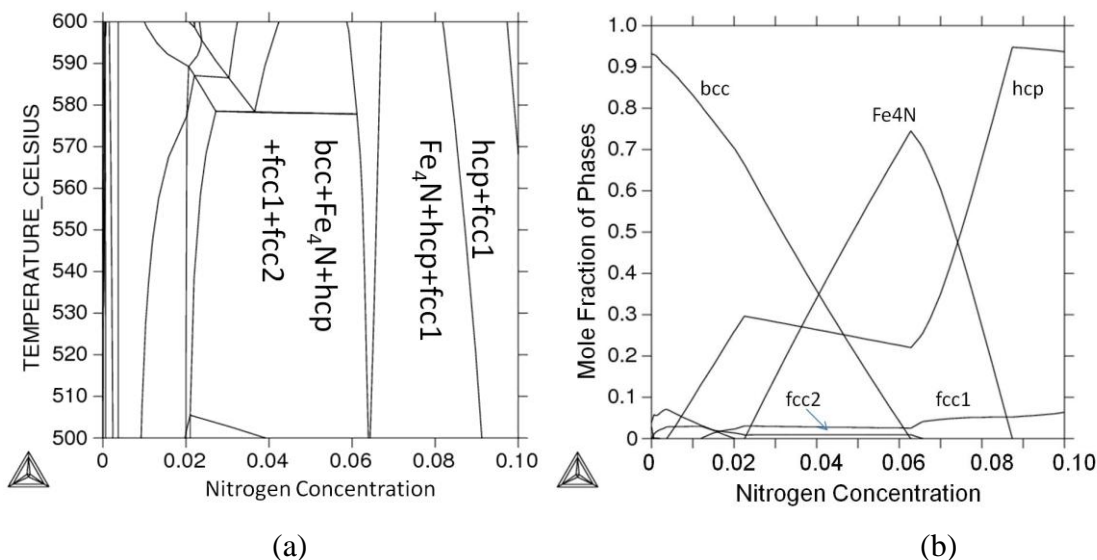
Figure 26. Isopleths of temperature vs. nitrogen concentration for AISI 4140 (a) and Phase evolution of phases with nitrogen concentration for AISI 4140 at 548°C (b)

Based on Figure 26(b), the phase evolution can be determined during the nitriding process. If the thermodynamics dominates during the nitriding process, the hcp (ε) will become stable with more than 0.5wt.% N and the stability increases with the nitrogen concentration. When the nitrogen concentration reaches more than 2wt.%, Fe_4N (γ') will form and coexist with hcp (ε) from 2.2wt.% to 8.7wt.% N.
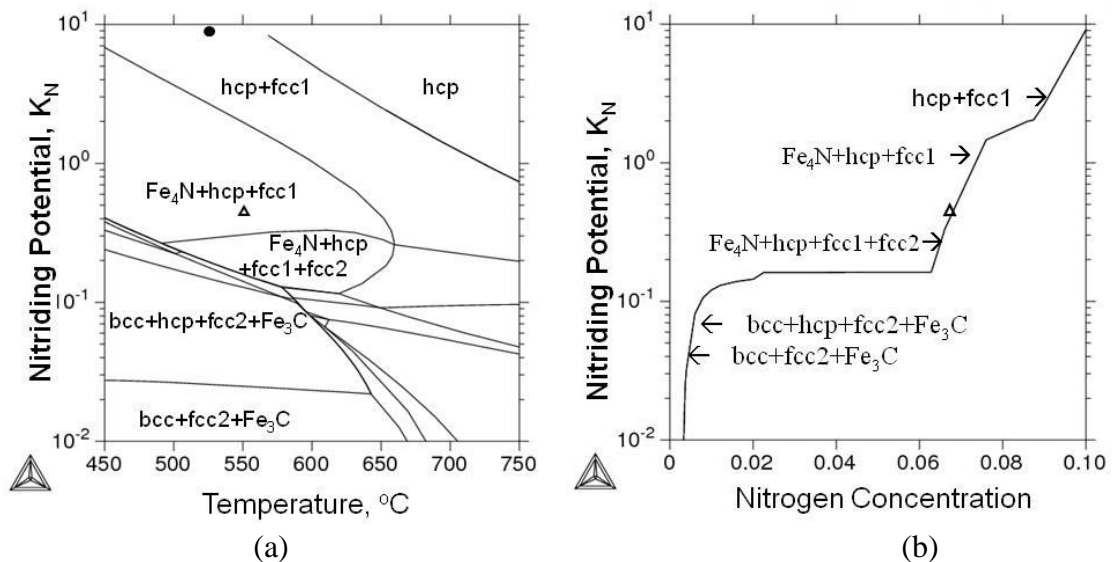
Figure 27. Lehrer diagram of AISI 4140 (a) and nitriding potential evolution with nitrogen concentration for AISI 4140 at 548°C (b).($\bullet$) represents nitriding condition in stage 1, i.e. K_n=9.24, T=527°C, (Δ) represents nitriding condition in stage 2, i.e. K_n=0.43, T=548°C

However, with the above phase diagrams, it is still difficult to choose the appropriate nitriding potential to enter the desired phase region. Therefore, the Lehrer diagram of AISI 4140 was calculated as shown in Figure 27 (a). The Lehrer diagram of

AISI 4140 clearly presents the phase regions corresponding to different nitriding potentials and is significantly different from that of pure iron as shown in Figure 25. Based on the Lehrer diagram of AISI 4140, the relationship between the nitriding potential and the nitrogen concentration at 548°C was also calculated.

Same as in Figure 25, the solid circles (●) in Figure 27 (a) corresponds to the nitriding parameters (temperature and nitriding potential) of stage 1, and the open triangles (Δ) corresponds to the nitriding parameters of stage 2. Since stage 2 involves higher temperature and longer process time, the final phase stabilities should be determined by stage 2. The Lehrer diagram of pure iron predicts that the single phase γ' should be observed in the compound layer, while the Lehrer diagram of AISI 4140 shows that both γ' and ε should exist in the compound layer. Figure 27 (b) shows that the nitrogen concentration on the surface of the the Nitrided AISI 4140 should be equal to approximately 6.8wt.%.

5.2.   Experimental results
5.2.1. SEM analyses

Figure 28 presents the backscatter electron micrograph from the cross section of the nitrided AISI 4140. The average thickness of the compound layer is 18.6μm and it is consisted of two layers. The inner layer (Region B) is mainly composed of a phase with bright contrast. The outer layer (Region A) shows two different contrasts (light areas and dark areas). The typical size of the discontinuous phase that appears dark is less than 1 m. This demonstrates the presence of very fine secondary phases.
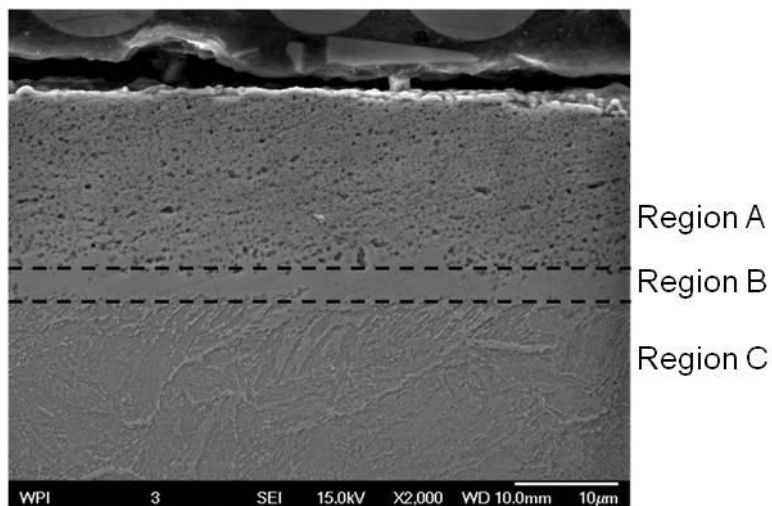
Figure 28. The SEM backscatter micrograph of the surface of the nitrided AISI 4140

5.2.2. TEM analysis

TEM analysis was performed to observe the phase development in the nitrided case for AISI 4140. Figure 29 presents the three distinct regions for the nitrided AISI 4140. Regions A and B corresponds to the two layers in the compound layer and region C corresponds to the diffusion zone. As indicated in the Figure 29, region A consists of three phases, γ' - Fe_4N, ε - $Fe_{2-3}(C, N)$, and Fe_7C_3. Although phase ε - $Fe_{2-3}(C, N)$ and Fe_7C_3 exhibit similar dark contrast on HAADF-TEM micrograph, a much smaller fraction of Fe_7C_3 is expected due to the low C concentration in this zone. Region B consists of γ' - Fe_4N and Fe_7C_3. In region C martensite and carbides were found. Representative indexed diffraction patterns are shown in Figure 30. The space group, crystal structure, and lattice parameters of identified phases are listed in Table 6. Fe_2N and Fe_3N are conventionally treated as ε - $Fe_{2-3}(C, N)$ phase due to the very close structure of Hexagonal and Orthorhombic Fe_2N[12]. TEM results are in good agreement

with the prediction from AISI 4140 Lehrer diagram that γ' - Fe_4N and ε - $Fe_{2-3}(C, N)$ coexist in the compound layer.
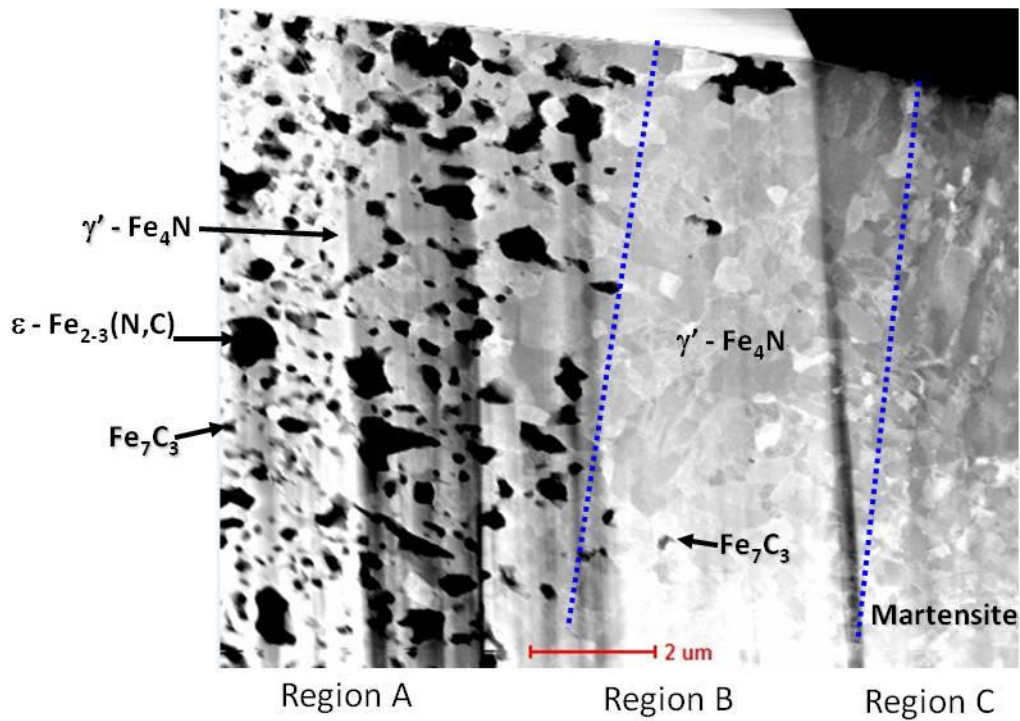
Figure 29. High angle annular dark field TEM micrograph from the nitrided case of AISI 4140

Table 6. Space group, crystal structure, and lattice parameters of relevant phases[13]

Phases	Space group (number)	Structure	Lattice parameters (Å)
Fe_4N	$Pm\bar{3}m$ (221)	Cubic	3.795
Fe_2N	Pbcn (60)	Orthorhombic	$4.443 \times 5.547 \times 4.848$
Fe_3N	P6322 (182)	Hexagonal	4.716×4.3869
Fe_7C_3	P63mc (186)	Hexagonal	6.882×4.54
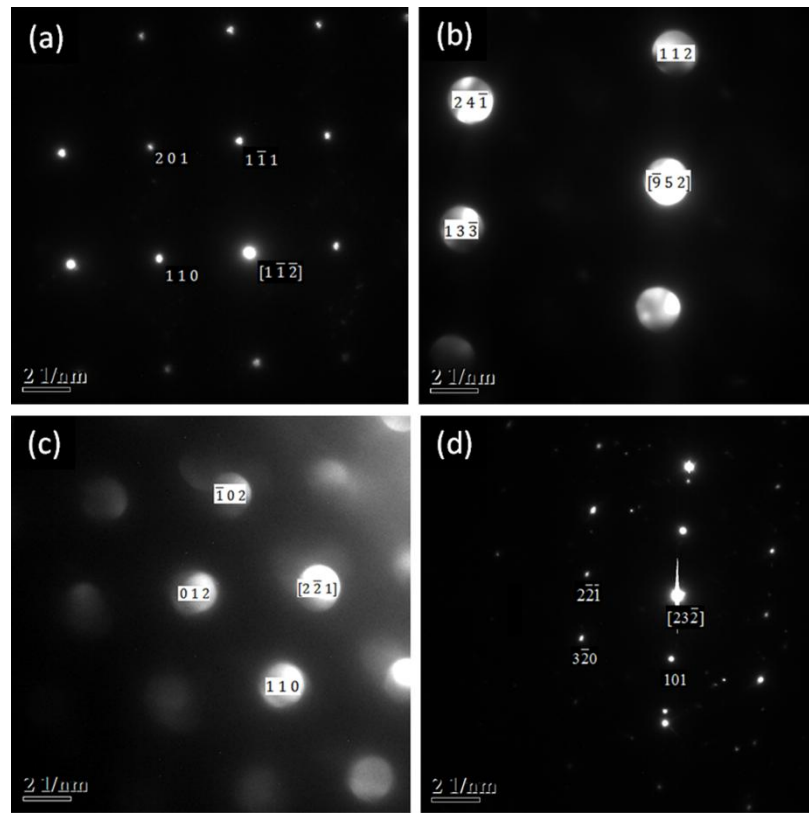
Figure 30. Representative diffraction patterns indexed to be (a) Fe_4N, (b) Fe_2N, (C) Fe_3N, and (d) Fe_7C_3 phase

6. Conclusions

The customized Lehrer diagram of AISI 4140 was successfully developed by computational thermodynamics. It differs from the Lehrer diagram of pure iron significantly. This diagram predicted the coexistence of ε - $Fe_{2-3}(C, N)$ and γ' - Fe_4N under the present nitriding process parameters. TEM diffraction analysis demonstrated that the γ' - Fe_4N coexists with ε - $Fe_{2-3}(C, N)$ in the compound layer of the nitrided AISI 4140 sample. This is consistent with the prediction from the customized AISI4140 Lehrer diagram.

Acknowledgement

References

1. M. A. J. Somers, *Heat Treat. Met.*, Vol 27, Issue 4, 2000, pp. 92-102.

2. D. Pye, *ASM International*, Materials Park, OH, 2003.

3. H. Du, M. A. J. Somers, J. Agren, *Metall. Mater. Trans. A*, Vol 31A, Issue 1, 2000, pp. 195-211A.

4. E. Lehrer, *Z. Elektrochem. Angew. Phys. Chem.*, 36, 1930, pp. 383.

5. E.J. Mittemeijer, J.T. Slycke, *Surf. Eng*., 12, 1996, pp. 152.

6. L. Maldzinski, Z. Przylecki, J. Kunze, *Steel Res.*, 57, 645 – 649 (1986).

7. N. Saunders, A. P. Miodownik, CALPHAD (Calculation of Phase Diagrams): A Comprehensive Guide (Pergamon, Oxford; New York), 1998.

8. J. O. Andersson, T. Helander, L. H. Hoglund, P. F. Shi and B. Sundman, Calphad, 26, 2002, pp. 273-312.

9. J. R. Davis, *Surface hardening of steels: understanding the basics,* Materials Park, OH, 2002.

10. K. Gamo, Nucl. Instrum. Methods Phys. Res., Sect. B, 121, 1997, pp. 464-469.

11. T. Kamino, T. Yaguchi, T. Ohnishi, K. Umemura and S. Tomimatsu., Microsc. Microanal., 6, 2000, pp. 510.

12. K.H. Jack, *Acta Cryst.*, 5, 1952, pp. 404.

13. *The inorganic crystal structure database (ICSD)*. 2004, Fachinformationzentrum (FIZ): Karlsruhe, Germany

Paper 3: Gaseous Nitriding Process Control: Application of Customized Lehrer Diagrams (submitted to Calphad)

Abstract

The state of the art for controlling the nitriding process is to measure and control the nitriding potential in the atmosphere to define the nitrogen concentration and phase stability at the steel surface. The experimental Lehrer diagram for pure iron is widely used in industry to specify the nitriding potential for the nitriding process of steels. However, applying the pure iron Lehrer diagram for the steels can lead to erroneous results because of the different phase stabilities in the steels. A customized Lehrer diagram for AISI 4140 had been developed previously based on computational thermodynamics[1]to predict the relationship between the nitriding potential and the phase stability as a function of temperature. The prediction is in excellent agreement with the experimental investigation and this proves the utility of using thermodynamic database to calculate the customized Lehrer diagrams for the steels. In the present work, a series of Lehrer diagrams are developed to analyze the effects of carbon and manganese on the nitriding process. These diagrams can be used to provide the nitriding process parameters for the specified steels but also pave a way for computational materials design of nitridable steels.

7. Introduction

Gaseous nitriding is a thermochemical surface treatment in which nitrogen is transferred from the atmosphere into the steel below the eutectoid temperature.[2, 3] This process is widely used to improve the wear and corrosion resistance and enhance

the fatigue endurance of steels. The specified properties of the nitrided steels depend on the nitriding process parameters. Conventionally, the trial and error method was used to define the nitriding process parameters to meet the specifications. This method is expensive, time consuming, and hard to control. The state of the art for controlling the nitriding process is to control the nitriding potential to define the microstructure of the nitrided layer.[4]

In our recent publication [1], the customized Lehrer diagram of AISI 4140 was constructed by computational thermodynamics. This diagram differs from the Lehrer diagram of pure iron significantly and shows excellent agreement with the experimental results. In the present work, the customized Lehrer diagrams of various iron-based alloys are developed by the same approach. Four Fe-C binary alloys with different carbon concentration were selected to understand the effect of carbon. Carbon steels with same carbon concentrations were selected to understand the effect of Mn.

These diagrams are used to analyze the effects of carbon and manganese on the relationship between nitriding process parameters and nitrided layer structure. Similar analysis will be expanded to the nitride forming elements such as Al, Cr, V, and Mo in the future. The results can not only be used to determine the appropriate process parameters but also pave a way to computational materials design of nitridable steels.

8. Nitriding Potential and Lehrer Diagram

In the gas nitriding process, the nitriding potential is used to describe the nitridability of the nitriding atmosphere which contains ammonia. It is defined as

$$K_n = \frac{p_{NH_3}}{p_{H_2}^{3/2}}$$

(1)

where p_{NH_3} and p_{H_2} are the partial pressures of the ammonia and hydrogen gases respectively. The experimental Lehrer diagram for pure iron was developed in 1930 [5] to show the relationship between the phases formed under local equilibrium and the nitriding potential as a function of temperature for pure iron. This diagram can provide the nitriding process parameters for pure iron. However, pure iron is never treated in real nitriding processes and the Lehrer diagrams for nitridable steels do not currently exist. The customized Lehrer diagrams for various steels are greatly needed.

The present work focused on the theoretical understanding of the effect of C and Mn to the gas nitriding process by using the customized Lehrer diagrams. In the real nitriding process, because the activity difference of C in the atmosphere and in the nitriding alloys, the decarburizing may be observed in the compound layer. During the nitriding process, the C on the surface may react with H in the atmosphere to form CH_4. The carbon concentration on the surface layer may be lower than which in the diffusion zone. The C concentration fluctuation in the compound layer was observed Winter [6]. However, the decarburization does not change much of the partial pressures of NH_3 and H_2 in the atmosphere, which determine the nitriding potential. The customized Lehrer

diagram is thus the right tool to understand the alloying effect in the gas nitridng process. Furthermore, the C effect summarizes in the present work can be helpful to understand the decarburization effect.

9. Computational Thermodynamics (CALPHAD)

The thermodynamic simulations were carried out via the CALPHAD methodology.[6] CALPHAD is an acronym for the CALculation of PHAse Diagram. It is capable of predicting the phase behavior in multi-component systems. In this approach, the Gibbs free energy of individual phases is modeled and the model parameters are collected in a thermodynamic database. Models for the Gibbs free energy are based on the crystal structures of the phases. CALPHAD has been under development since early 1970's. The development of CALPHAD techniques in the past three decades was discussed by Saunders and Miodownik.[6] In the current work, TCFE6 database was used to make all the calculations for pure iron and various Fe-C binary alloys and carbon steels, which were carried out using Thermo-Calc[7].

In the current work, TCFE6 database was used to make all the calculations for pure iron and various Fe-C binary alloys and carbon steels, which were carried out using Thermo-Calc [8]. There are always arguments on the accuracy of the thermodynamic description of the most important Fe-C-N ternary system for nitriding process. Fe-N binary system and Fe-C-N ternary system in the TCFE6 database use the thermodynamic description by Du et al. [9] The results from Du et al. [9] show overall good agreement

with the old experimental data as well as the recent experimental data on the phase

transformation between $\alpha+\gamma$'+cementite and $\alpha+\varepsilon+\gamma$' [10].

10. Lehrer diagram of pure Fe

Figure 31 presents the Fe-N binary phase diagram for the nitriding process area

drawn from Thermo-Calc. It shows that in the pure Fe within the nitriding temperature

range (below the eutectoid temperature, 590°C), with the increase of nitrogen

concentration in the iron the first nitride developing at the surface is γ' (Fe_4N). Then ε

($Fe_{2-3}N$) phase is formed with higher nitrogen concentrations.

Figure 25 shows the calculated pure iron Lehrer diagram from our recent work

[1]. It shows at low nitriding potential, N dissolves interstitially in the α (Ferrite) matrix

phase, which corresponds to the diffusion zone in the nitrided iron. With increasing the

nitriding potential, γ' phase forms and then ε phase. It is always observed that ε and γ'

phases form two well-defined layers on the surface of nitrided pure iron [8], which

corresponds to the compound layer. Therefore, at the constant temperature the phase

evolution during the nitriding process is determined by the nitriding potential. The Lehrer

diagram also indicates the maximum nitriding temperature is approximately 590°C for

pure iron, as γ (Austenite) phase will form at higher temperature.

11. Customized Lehrer diagrams of Fe-C systems

In industry, many steels have been designed for the nitriding process. These steels

present a wide variation in composition; however they have some common elements,

such as C, Mn, Al, Cr, V, and Mo.To understand the effect of different alloy elements on the nitriding process parameters, the first step is to investigate carbon effect since carbon exists in all steels. Four compositions, i.e. 0.2wt.%, 0.4wt.%, 0.6wt.%, and 0.8wt.% C concentrations in Fe-C system were thus selected to construct the customized Lehrer diagrams for Fe-C alloys.

Figure 33 presents the570^{o}C isothermal section of Fe-C-N ternary phase diagram. It shows that the ε phase becomes the first nitride phase to form in compound layer with the presence of carbon. By controlling the nitrogen and carbon concentration the single ε (Fe$_{2-3}$(N,C)) phase region can be developed. However, γ' phase is only formed at a relative low carbon concentration range and coexists with ε phase. This can be explained by the crystallographic resemblance between orthorhombic and hexagonal crystal structure. Cementite (Fe$_3$C), which is part of the steel matrix, has orthorhombic crystal structure and can easily be converted into hexagonal ε phase. [9]

The isopleths of Fe-C-N phase diagram with various carbon concentrations are presented in Figure 34. These diagrams show that the first nitride phase to form during the nitriding process changes to the ε (Fe$_{2-3}$(N,C)) phase, which indicates that carbon stabilizes the ε phase.

In addition, Figure 34shows the formation of the γ' (Fe$_4$N) phase requires more nitrogen for higher carbon concentration steels and the solubility range of the nitrogen in the ε phase increases with the increase of the carbon content. Furthermore, the eutectoid temperature was reduced to ~577°C, which decreases the maximum nitriding temperature.

The corresponding customized Lehrer diagrams for these Fe-C alloys are presented in Figure 35. Obviously, these Lehrer diagrams are very different from pure iron Lehrer diagram. No single γ' phase region exists in these diagrams, which means γ' single phase layer cannot be formed during the nitriding process. Figure 36 presents the comparisons between pure iron and various Fe-C alloys for the phase transformation from ε and γ' two phase's region toε single phase region. For pure iron, the boundary exists between ε and γ'.It shows nitriding potential at the fixed nitriding temperature drop with the increase of carbon concentration. At the typically nitriding temperature, i.e. 570°C, the nitriding potential need to be over 2.3 for pure iron and only 1.1 for Fe-0.8wt.%C to form εsingle phase on the surface.

Figure 37 shows that the phase transformation from the ε+γ' two phase region toε single phase region at the nitriding potential around 0.25 (the nose of the figures) drop dramatically from 696°C for pure iron to 625°C forFe-0.8wt.%C. Therefore, carbon stabilizes the ε phase, which is in good agreement with the isopleths plots.

12.Customized Lehrer diagrams of carbon steels

The same calculations were done for various carbon steels, i.e. AISI 1020, AISI 1040, AISI 1060, and AISI 1080, the compositions were listed in Table 7. The main difference between the carbon steels and the Fe-C systems is the addition of manganese. In the calculations below, only Fe, C, and Mn are considered, while P and S are neglected due to their low concentration. 0.2wt.%C, 0.4wt.%C,0.6wt.%C,and 0.8wt.%C are taken for AISI 1020, AISI 1040, AISI 1060, and AISI 1080respectively to do the calculations.

And 0.45wt.%Mn is used for AISI 1020, 0.75wt.%Mn is used for AISI 1040, AISI 1060, and AISI 1080.

The isopleths of these steels are shown in Figure 38. It shows the carbon steels are composed of α-Fe (ferrite) and Fe_3C (cementite) before nitriding. And similar to Fe-C alloys nitriding, the first nitride phase formed during a nitriding process is the ε phase.

The Lehrer diagrams of these carbon steels are presented in Figure 39. It is seen that the Lehrer diagrams of carbon steels are very different from that of pure iron but similar to those of Fe-C binary alloys. There is no single γ' phase in carbon steels. The comparisons of phase transformation from ε and γ' two phase's region to ε single phase region for various carbon steels and pure iron are shown in Figure 40 and Figure 41. They are basically same as those for Fe-C alloys as shown in Figure 36 and Figure 37. Therefore, it can be concluded that carbon concentration plays dominate role on the $(\gamma'+\varepsilon)/\varepsilon$ phase transformation.

Comparing the Lehrer diagrams of carbon steels with those of Fe-C alloys, it is found that the phase boundaries between the $(\alpha + Fe_3C + \varepsilon)$ ternary phase region and $(\alpha+Fe_3C)$ binary phase region shift to higher nitriding potential level. Therefore, the addition of manganese significantly affects the phase transformation from Fe_3C to ε phase. With the existence of Mn, the formation of ε phase occurs at higher nitrogen concentration. Figure 42 presents the comparison among AISI 1040, AISI1060, and AISI1080 for the $(\alpha + Fe_3C + \varepsilon)/(\alpha+Fe_3C)$ phase transformation. Same calculation results for AISI 1020 are not listed, as the Mn content in AISI1020 is lower than that in the other

three carbon steels. With the addition of carbon in carbon steels, the nitriding potential of this transformation drops. C enhances the phase stability of εin the diffusion zone.

13.Conclusions

In the present work, the isopleths and customized Lehrer diagrams of various Fe-C alloys and carbon steels were drawn in comparison with those of pure iron. The detail comparisons show the effect of C and Mn on nitriding temperatures and the phase stabilities during the nitriding process. It is seen that the addition of C stabilized the εphase. The maximum nitriding temperature is greatly reduced due to the addition of C decreasing the eutectoid temperature .Mn decreases the stability of ε phase in the diffusion zone.

Similar analysis of the other important alloying elements will be discussed in the future. The customized Lehrer diagrams are very useful to optimize the nitriding process as the Lehrer diagrams of different alloys are very different from each other. By incorporating the thermodynamic predictions from Lehrer diagrams with the kinetic simulations, the nitriding process of individual alloys can be optimized and new alloys may be designed.

Reference:

1   M. Yang, B. Yao, Y. H. Sohn, R. D. Sisson Jr., *International Heat Treatment and Surface Engineering* 5, (2011) 122-126.

2   M. A. J. Somers, *Heat Treatment of Metals* 27, (2000) 92-102.

3   D. Pye, *Practical nitriding and ferritic nitrocarburizing*, ASM International, Materials Park, OH (2003).

4   W. Gräfen, B. Edenhofer, *Surface and Coatings Technology* 200, (2005) 1830-1836.

5   E. Lehrer, *Zeitschrift fuer Elektrochemie und Angewandte Physikalische Chemie* 36, (1930) 383.

6   N. Saunders, A. P. Miodownik, *CALPHAD (Calculation of Phase Diagrams): A Comprehensive Guide*, Pergamon, Oxford, New York (1998).

7   J. O. Andersson, T. Helander, L. H. Hoglund, P. F. Shi, B. Sundman, *CALPHAD* 26, (2002) 273-312.

8   L. Tatiana, *Phase transformations in interstitial Fe-N alloys*, (2005).

9   E. J. Mittemeijer, W. T. M. Straver, P. F. Colijn, P. J. van der Schaaf, J. A. van der Hoeven, *Scr. Metall.* 14, (1980) 1189-1192.
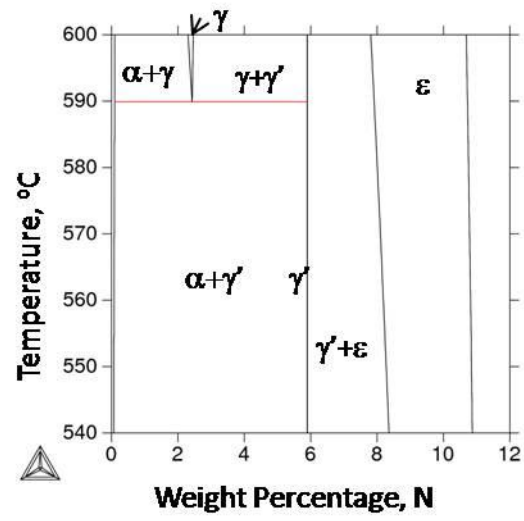
Figure 31. The Fe-N binary phase diagram drawn by Thermo-Calc.
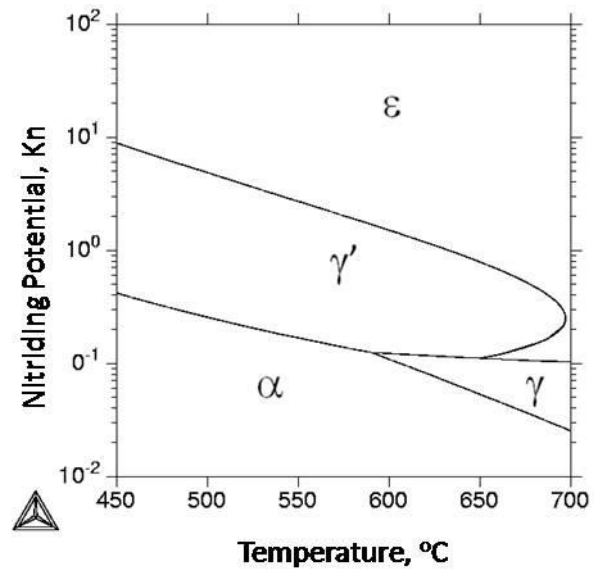
Figure 32. Lehrer diagram of the pure iron from Thermo-Calc calculation.
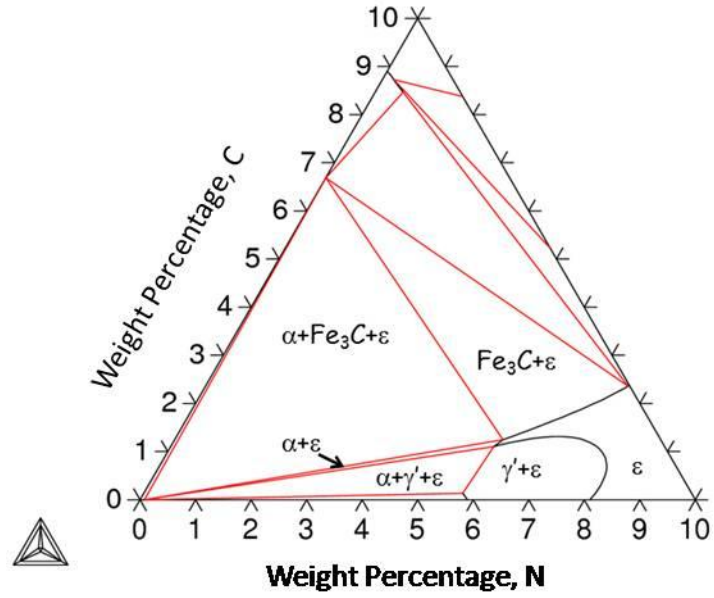
Figure 33. Fe-C-N isothermal section at 570$^{\text{o}}$C from Thermo-Calc
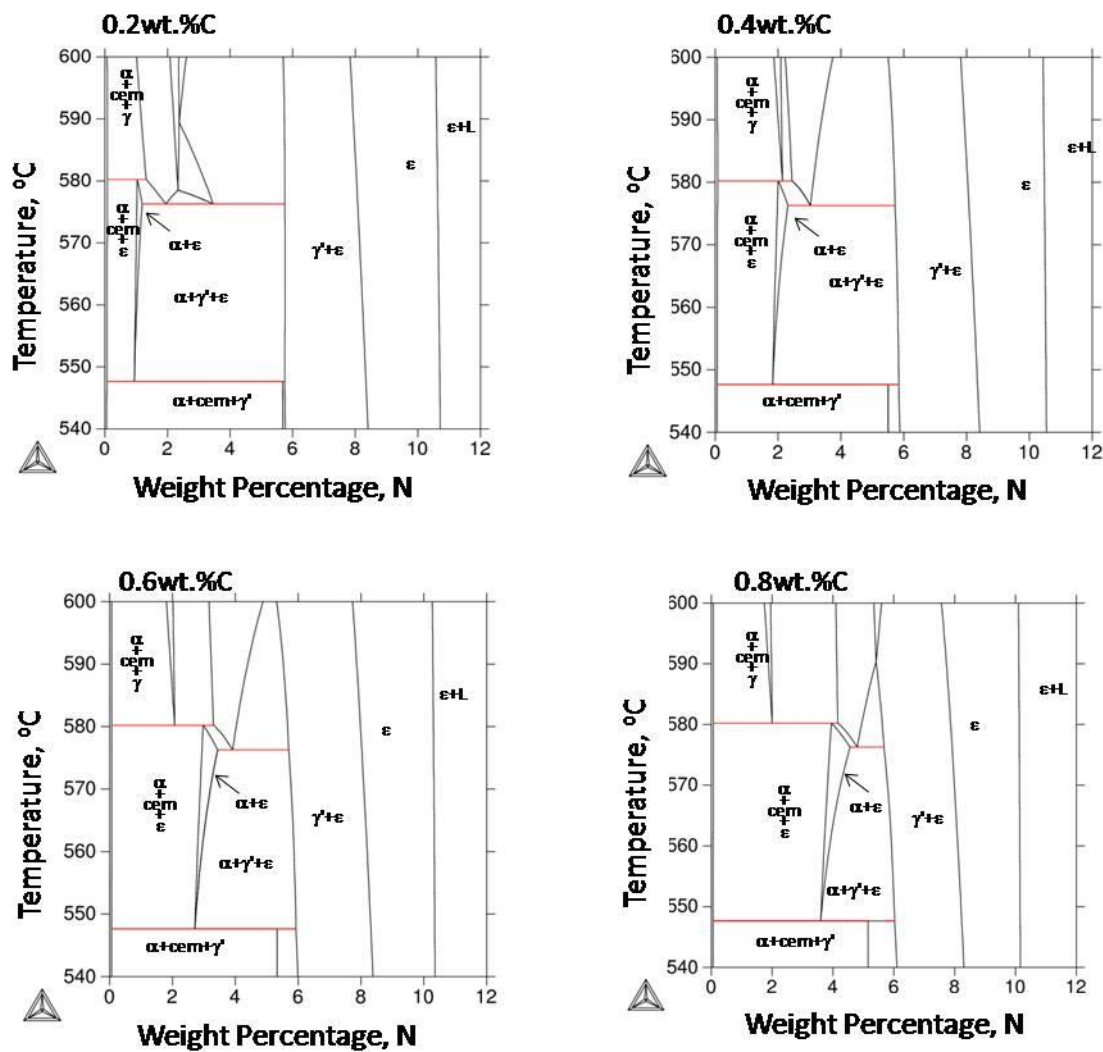
Figure 34. Isopleths calculated by Thermo-Calc for various Fe-C-N alloys with

0.2wt.%C, 0.4wt.%C, 0.6wt.%C, and 0.8wt.%C.
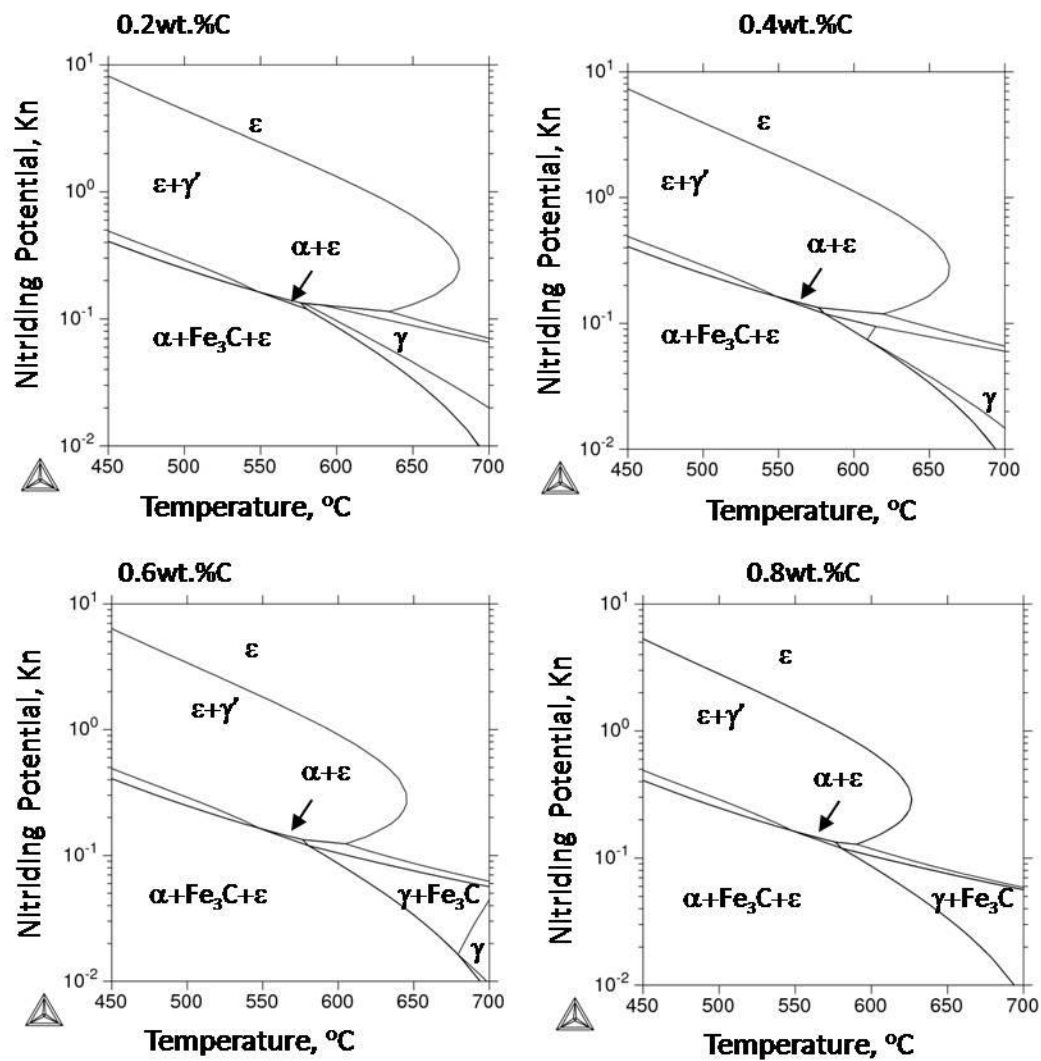
Figure 35. Customized Lehrer diagrams calculated by Thermo-Calc for various Fe-C

alloys, i.e. 0.2wt.%C, 0.4wt.%C, 0.6wt.%C, and 0.8wt.%C.
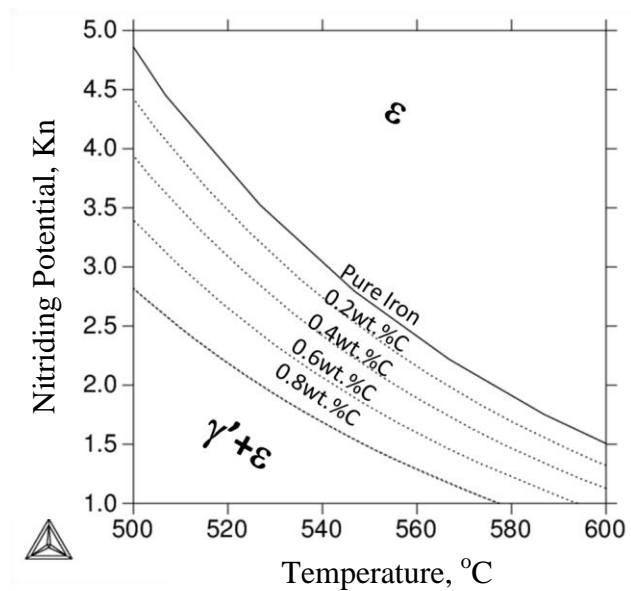
Figure 36. A portion of the Lehrer diagram of pure iron and various Fe-C alloys, i.e. 0.2wt.%C, 0.4wt.%C, 0.6wt.%C, and 0.8wt.%C, describing the phase equilibria boundary of (γ'+ε)/ε between 500°C and 600°C drawn by Thermo-Calc.

Figure 37. A portion of the Lehrer diagram of pure iron and various Fe-C alloys, i.e. 0.2wt.%C, 0.4wt.%C, 0.6wt.%C, and 0.8wt.%C, describing the phase equilibria boundary of $(\gamma'+\varepsilon)/\varepsilon$ between 600°C and 700°C drawn by Thermo-Calc.

Table 7. Composition of various carbon steels in wt.%

Composition / Carbon Steel	C	Mn	P	S	Fe
AISI 1020	0.18 - 0.23	0.3 - 0.6	0.04 (max)	0.05 (max)	balance
AISI 1040	0.37 – 0.44	0.6 – 0.9	0.04 (max)	0.05 (max)	balance
AISI 1060	0.55 – 0.65	0.6 – 0.9	0.04 (max)	0.05 (max)	balance
AISI 1080	0.75 – 0.88	0.6 – 0.9	0.04 (max)	0.05 (max)	balance
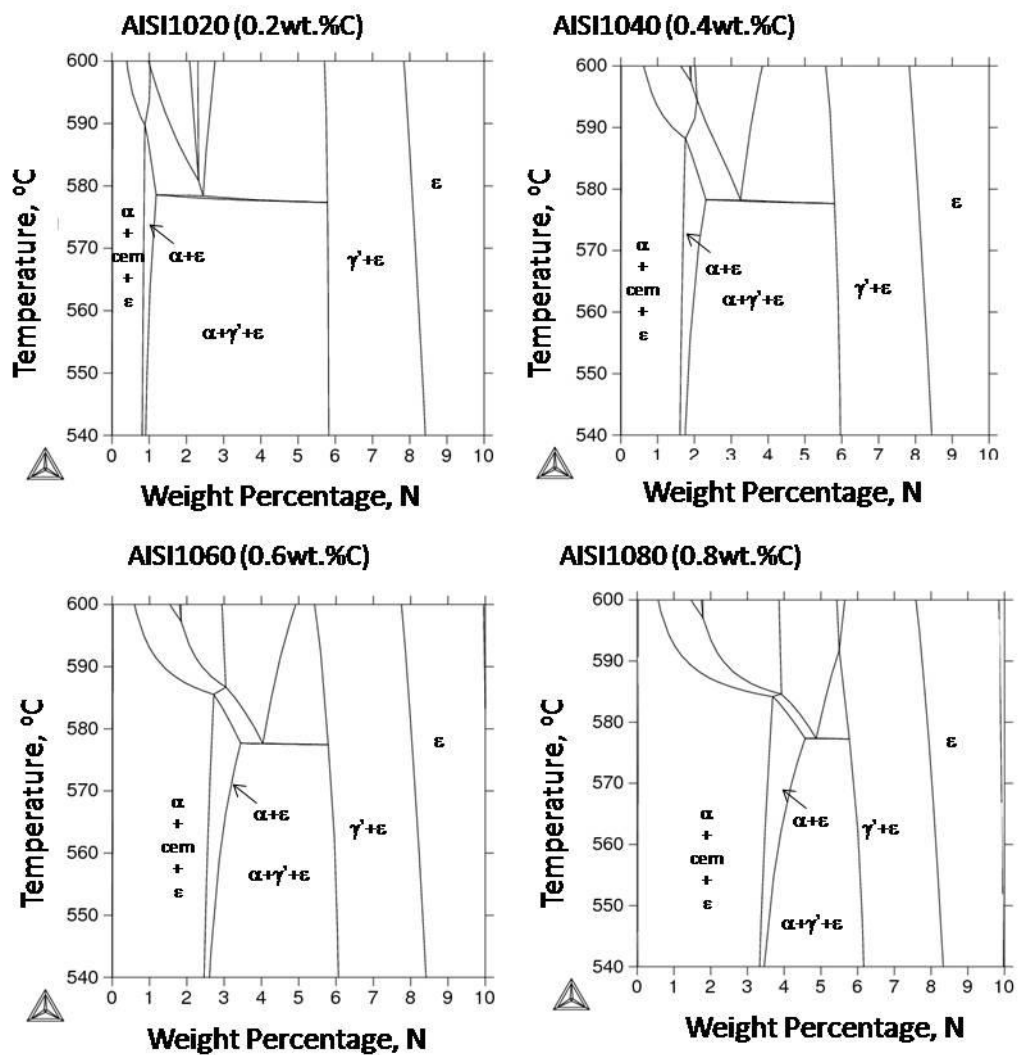
Figure 38. Isopleths calculated by Thermo-Calc for various carbon steels, i.e. AISI 1020, AISI 1040, AISI 1060, and AISI 1080.
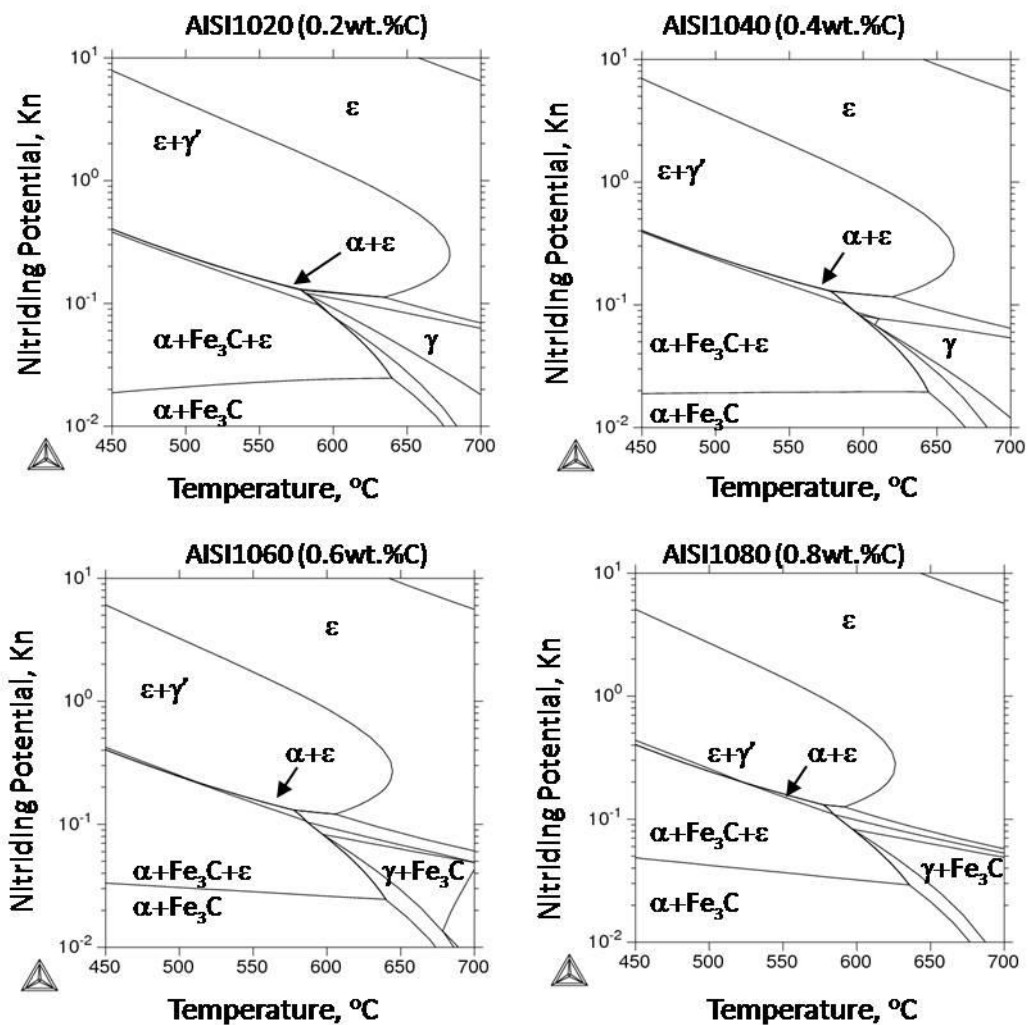
Figure 39. Customized Lehrer diagrams calculated by Thermo-Calc for various carbon steels, i.e. AISI 1020, AISI 1040, AISI 1060, and AISI 1080.
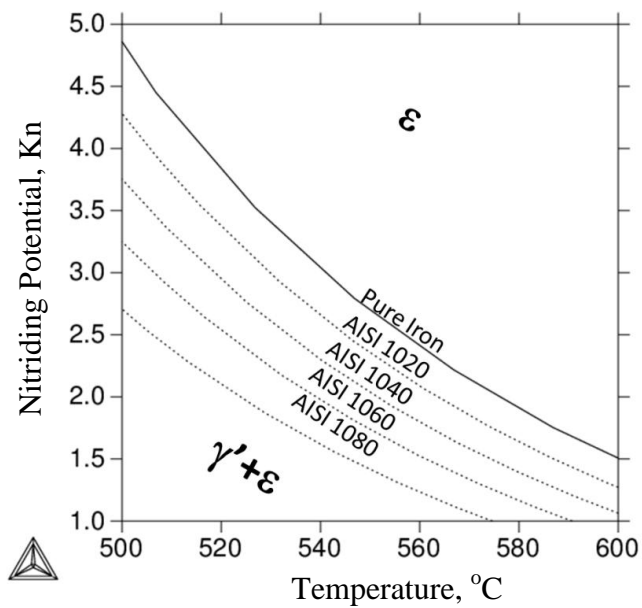
Figure 40. A portion of the Lehrer diagram of pure iron and various carbon steels describing the phase equilibria boundary of (γ'+ε)/ε between 500°C and 600°C drawn by Thermo-Calc.

Figure 41. A portion of the Lehrer diagram of pure iron and various carbon steels describing the phase equilibria boundary of (γ'+ε)/ε between 600°C and 700°C drawn by Thermo-Calc.

Figure 42. A portion of the Lehrer diagram of pure iron and various carbon steel describing the phase equilibria boundary of $(\alpha+Fe_3C+\varepsilon)/(\alpha+Fe_3C)$ between 500^oC and 580^oC drawn by Thermo-Calc.

Paper 4: Modeling the Nitriding of Steel by Compound Layer Growth Model (Accepted by Journal of ASTM international)

Abstract

The effort to simulate the nitriding process has been ongoing for the last 20 years. Most of the work has been done to simulate the nitriding process of pure iron. In the present work the compound layer growth model has been developed to simulate the nitriding process of AISI 4140 steel. In this paper the fundamentals of the model are presented and discussed including the kinetics of compound layer growth and the determination of the boundary conditions. The experimental verification of the model is also presented. It proves the concept of utilizing the compound layer growth model in other steels. The nitriding process of various steels can thus be modeled and predicted in the future.

14. Introduction

Nitriding is a thermochemical surface treatment in which nitrogen is transferred from an ammonia atmosphere into the steel below the eutectoid temperature. [1, 2] Due to the low solubility of nitrogen in ferrite [3], the nitrides (ε - Fe_{2-3}(C, N) and/or γ' - Fe_4N) precipitate during the nitriding process. A compound layer and an underlying diffusion zone (i.e. case) are formed near the surface of the steel after nitriding. The compound layer, also known as the white layer, consists of nitrides and can greatly improve wear and corrosion resistance.[4] The hardened diffusion zone is also responsible for a considerable enhancement of the fatigue endurance. Furthermore,

being a low temperature process, nitriding minimizes distortion and deformation of the heat treated parts. [2]

The properties of the nitrided steels depend on the nitriding process parameters. Conventionally, trial and error methods were used to define the nitriding process parameters to meet the specifications. This method is expensive, time consuming, and hard to control. Therefore, an effective simulation tool is needed to predict the nitriding process of a variety of steels. By using this tool the nitriding process parameters can be pre-defined to meet the specifications.

The effort to simulate the nitriding process has been ongoing for the past 20 years. Much of the work has been done to simulate the nitriding process of pure iron [5-7]. Good agreement has been achieved by using various models. However, the pure iron is never used for nitriding in industry and the simulations for steels become much more complicated, since the well-defined ε and γ' sublayers in nitrided pure iron are replaced by the mixture of these two phases in nitrided steels. [8]

In the present work, the compound layer growth model [5] is developed to simulate the compound layer growth kinetics for nitriding AISI 4140 based on the customized Lehrer diagram [9]. This model can be used to calculate concentration profiles of nitrogen as a function of time and position during the nitriding process. In addition, it can be used to predict the thickness of the compound layer.

15.Experiments

15.1.   Materials and nitriding

The AISI 4140 bars used in the experimental study were acquired from Peterson Steel Corporation and their composition determined by optical emission spectroscopy (OES) is reported in Table 4.

Table 8. Composition of AISI 4140 in wt.%

C	Mn	P	S	Si	Cr	Mo	Fe
0.399	0.91	0.01	0.029	0.266	0.88	0.166	Balance

Before nitriding, the cylindrical steel bars were heat treated to harden the core by heating to 843°C and keeping at this temperature for 1.5 hours in Endothermic gas at 0.4% carbon potential, followed by quenching in agitated 54°C mineral oil, and were washed in hot water and tempered in air at 579°C for 3 hours (Bodycote, Worcester, MA, USA).

The bars were machined into disks with a diameter of 3.175 cm and thickness of 1 cm. A hole of 2mm in diameter was drilled near the edge for holding the sample during the process. The disks were washed with alcohol prior to the nitriding process. A standard two - stage industrial nitriding process was used for the current work. During the first stage, nitriding was carried out using ammonia gas with a dissociation rate of 24% ~28% at 527°C for 10 hours. The second stage lasted 50 hours at 548°C with the dissociation rate of 79%~82%. Dissociation rate represents the percentage of ammonia

dissociated into hydrogen and nitrogen and is measured by using a burette in the furnace exhaust gas.

15.2.   SEM analysis

Figure 28 presents the backscatter electron micrograph from the cross section of the nitrided AISI 4140. It shows that the compound layer consists of two layers. The outer layer (Region A) has two different contrasts (light areas and dark areas). The inner layer (Region B) is mainly composed of a phase with bright contrast. The typical size of the discontinuous phase (dark areas in Region A) is less than 1μm. This demonstrates the presence of very fine secondary phases.
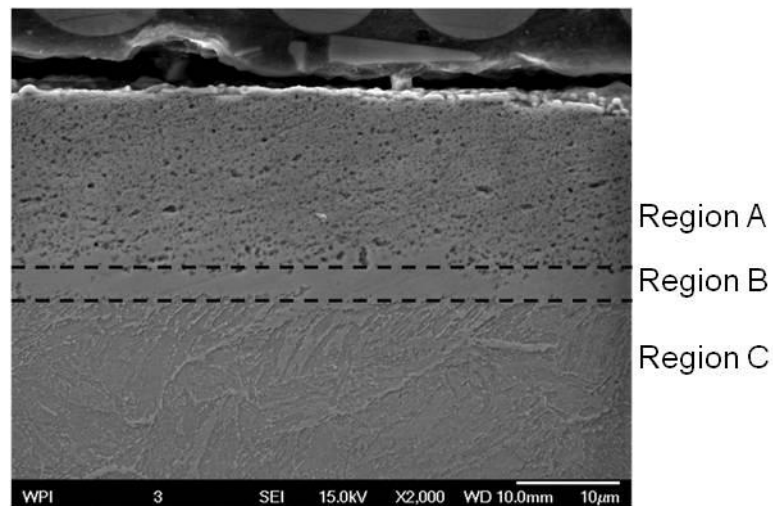
Figure 43.The SEM backscatter micrograph of the cross section of the nitrided AISI 4140 [9]

15.3. TEM analysis

The detailed TEM analysis for the cross section of the nitrided AISI 4140 was reported in the previous publication [9]. Figure 29 presents the three distinct regions for the nitrided AISI 4140. Regions A and B correspond to the two layers in the compound layer (compare with Figure 28) and Region C corresponds to the diffusion zone. As indicated in the Figure 29, Region A consists of three phases, γ' - Fe_4N, ε - $Fe_{2-3}(C, N)$, and Fe_7C_3. Region B consists of γ' - Fe_4N and Fe_7C_3. In Region C martensite and carbides were found.
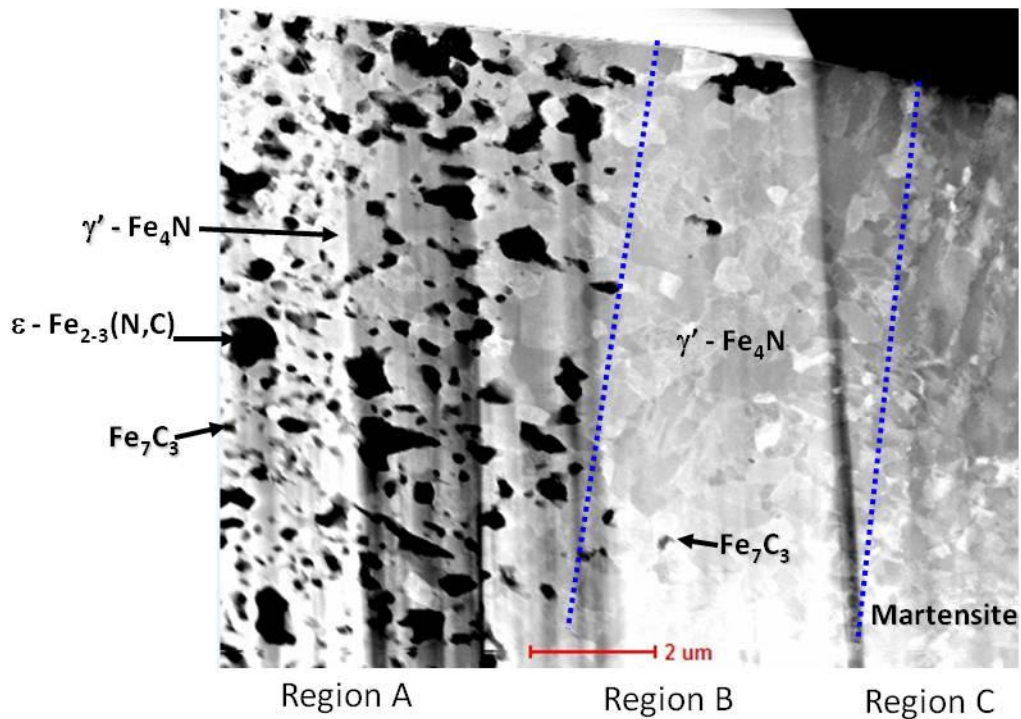
Figure 44. High angle annular dark field TEM micrograph from the nitrided case of AISI 4140 [9]

15.4.   Microhardness and nitrogen concentration

The microhardness for the cross section of nitrided AISI 4140 was measured to determine the hardness change from the surface layer to the bulk. The measurements started at 50μm depth from the edge with an increment of 100μm per measurement afterwards.

OES can only measure the nitrogen concentration on solid surfaces. To obtain the nitrogen concentration profile (nitrogen concentration vs. depth) the measured surfaces were removed layer by layer and measurements were taken at four different locations on the surface of each layer.
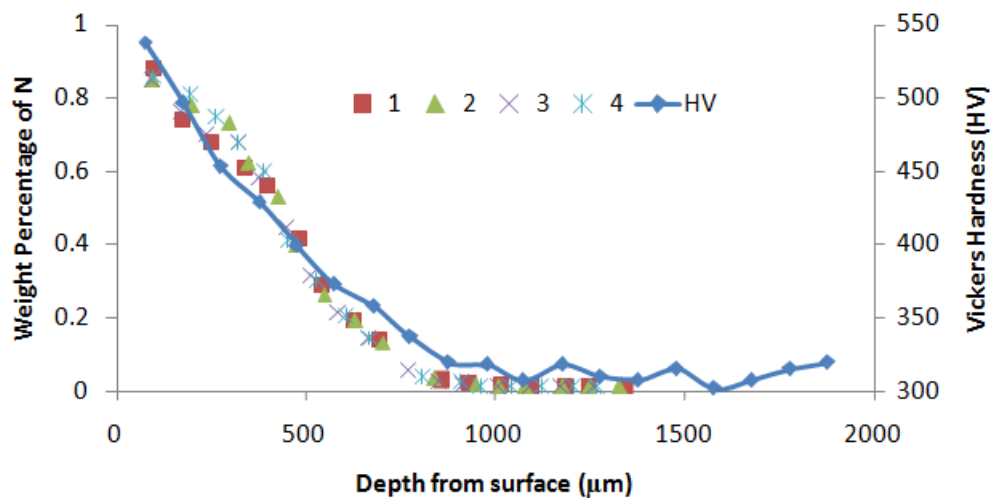
Figure 45. Weight percentages of nitrogen vs. depth from surface and Vickers hardness vs. depth from surface for nitrided AISI 4140. The weight percentages of nitrogen were measured by OES for four different locations.

The microhardness and the weight percentage of nitrogen vs. depth from surface were both plotted for nitrided AISI 4140 as shown in Figure 45. There is an excellent correlation between the nitrogen concentration and the microhardness.

16. The customized Lehrer diagram for AISI 4140

Lehrer diagram [10] depicts the development of phase constituents in pure iron as functions of nitriding potential and temperature. The nitriding potential (K_n) is defined as:

$$K_n = \frac{p_{NH_3}}{p_{H_2}^{3/2}} \tag{1}$$

where p_{NH_3} and p_{H_2} are the partial pressures of the ammonia and hydrogen gases respectively. The dissociation rate used in the present work can be converted to the values for p_{NH_3} and p_{H_2} and consequently for the nitriding potential.

The Lehrer diagram of pure iron and the customized Lehrer diagram of AISI 4140 have been successfully developed by computational thermodynamics. [11] TCFE6 database was used to make all the calculations, which were carried out using the Thermo-Calc software. [12] The Gibbs energy of fcc phase in the TCFE6 database was modeled to describe the austenite in steel and the M(C,N) carbonitrides since both share the same crystal structure. Two sublattice model $(M)_1(C,N,Va)_1$ was adopted for fcc according to its crystal structure. Metallic elements (M), such as Fe, Mn, Mo, and Cr, occupy the first sublattice that correspond to the 4a site of fcc structure; while C, N, and vacancy occupy the second sublattice, that corresponds to the 4b site of fcc structure. If the 4b site is

mainly occupied by a vacancy, it is the austenite in steel. In the current calculations for AISI 4140, there are two fcc phases (fcc1: $(Fe_{0.63}Cr_{0.36})_4(N)_3$ and fcc2: $(Cr_{0.57}Fe_{0.25}Mo_{0.16})_1(N)_1)$ due to the immiscibility of the Gibbs energy description of the fcc phase in the TCFE6 database.

(a)   (b)
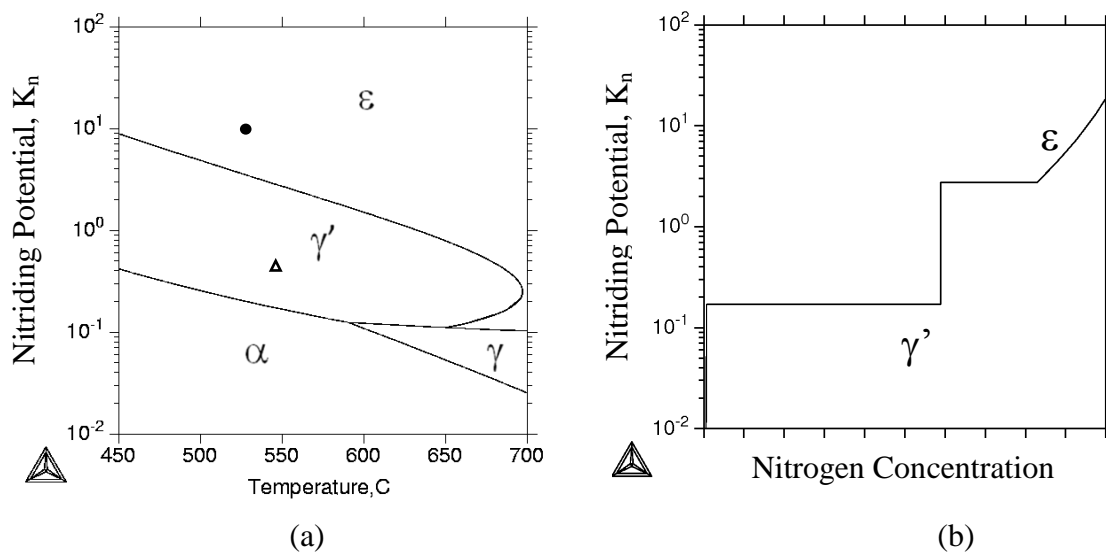
Figure 46. Lehrer diagram of pure iron (a) and nitriding potential evolution with nitrogen concentration for pure iron at $548^{o}C$ (b).($\bullet$) represents nitriding condition in stage 1, i.e. K_n=9.24, T=$527^{o}C$, (Δ) represents nitriding condition in stage 2, i.e. K_n=0.43, T=$548^{o}C$

Figure 47. Lehrer diagram of AISI 4140 (a) and nitriding potential evolution with nitrogen concentration for AISI 4140 at 548°C (b).(●) represents nitriding condition in stage 1, i.e. K_n=9.24, T=527°C, (Δ) represents nitriding condition in stage 2, i.e. K_n=0.43, T=548°C [9]

Figure 46 (a) is the Lehrer diagram of pure iron. The customized Lehrer diagram of AISI 4140 (Figure 47(a)) is very different from it. The Lehrer diagram of pure iron shows two single-phase sublayers (the ε layer and γ' layer) in the compound layer. However, single nitride phase layer in the compound layer does not exist in nitrided AISI 4140 at the typical nitriding temperature, which is less than 550°C.

In addition, the relationship between the nitriding potential and the nitrogen concentration at fixed temperature can be calculated. Figure 47 (b) shows the nitriding potential as a function of nitrogen concentration at 548°C, which is the nitriding temperature used in the second stage of the present experiment. In the nitriding potential

vs. nitrogen concentration diagram of pure iron Figure 46 (b), there are two horizontal lines. One is between α and γ' single-phase regions, the other one is between γ' and ε single-phase regions. These lines correspond to the $\alpha + \gamma$' and γ' + ε' two-phase regions and the nitriding potentials are invariant along these two lines.

According to the definition of the nitriding potential (K_n) in equation 1, the nitriding potential is proportional to the activity of nitrogen (a_N) in the atmosphere. The invariant lines on nitriding potential vs. nitrogen concentration diagram thus represent constant nitrogen activity when local equilibrium between gaseous atmosphere and steel surface is assumed. Therefore, these two invariant lines indicate the interface between γ' and ε sublayers and the interface between γ' and diffusion zone.

It is very important to note that there is a horizontal line on Figure 47 (b) for AISI 4140 when the nitrogen concentration varies from 2.3 to 6.5 wt. %N. This line indicates that the nitrogen activity is constant in nitrided AISI 4140 when the nitrogen concentration is between 2.3 and 6.5 wt.%N. Furthermore, in the region above, there is no bcc phase, while in the region below, there is bcc phase. Therefore, for nitrogen concentration higher than 6.5wt.% the compound layer exists and for nitrogen concentration lower than 2.3wt.% the diffusion zone exists. The interface between the compound layer and the diffusion zone in nitrided AISI 4140 is well defined from this nitriding potential vs. nitrogen concentration diagram (i.e. Figure 47 (b)).

17. Nitride layer growth model

The kinetics of diffusion-controlled compound layer growth can be modeled by the shift of the interface between compound layer and diffusion zone when the local equilibrium is assumed at the interface. In nitrided pure iron, single-phase layers exist in the compound layer and the nitrogen concentrations on the interfaces between these layers can be defined from the binary Fe-N phase diagram based on local equilibrium assumption [7]. Somers et al. [5] successfully adopted this model to derive the monolayer (γ') and bilayer (ε and γ') growth into the substrate for the pure iron nitriding process. However, it is challenging to apply this model for steels. In nitrided steels, the well-defined single phase layers are replaced by the multiphase mixture, which makes it hard to define the nitrogen concentrations at the interface between the compound layer and diffusion zone.

Following the nitride layer growth model of pure iron proposed by Somers et al. [5], the compound layer growth model on nitriding of steels was developed as shown in Figure 48. N^s is the nitrogen concentration on the outside steel surface. At the compound layer/diffusion zone interface, the nitrogen concentration is N^c at the interface in the compound layer and is N^d at the interface in diffusion zone. N^0 is the nitrogen concentration in steel before nitriding process.

The initial position of the interface between compound layer and diffusion zone is ξ. If the interface shifts a distance $d\xi$ into the substrate within a time increment dt, the mass conservation in the compound layer is expressed as:

$$(N^c - N^d) \cdot d\,\xi + dW = (J^c \mid_{X=0} - J^d \mid_{X=\xi}) \cdot dt$$

(2)

where J^c is the flux of nitrogen entering the compound layer at the steel surface and J^d is the flux of nitrogen leaving the compound layer at the interface, dW is the amount of solute that accumulates in the compound layer to maintain a concentration - depth profile.
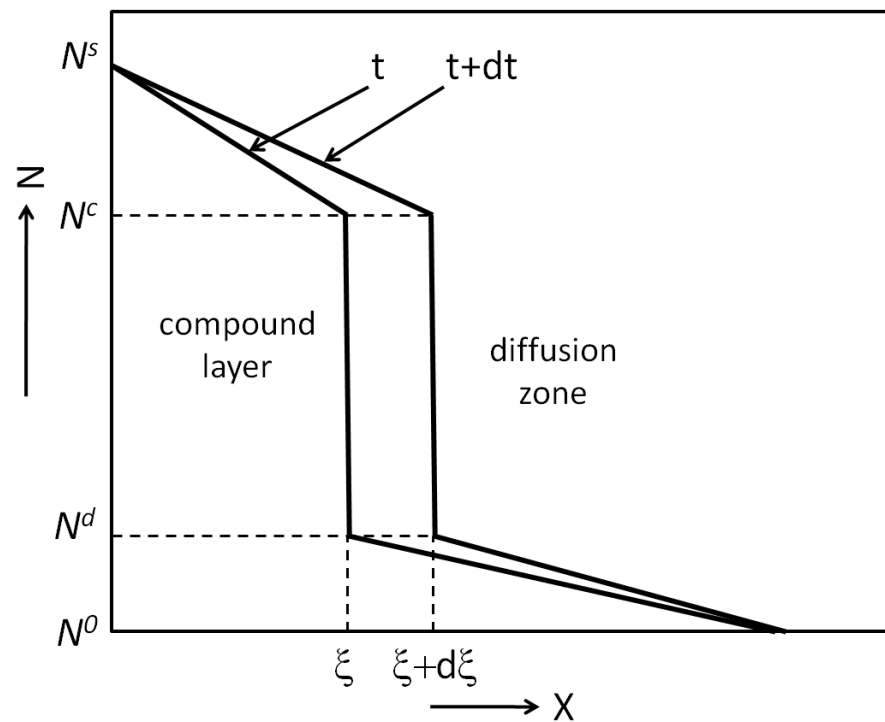
Figure 48. Schematic of the nitride layer growth model on nitriding of steel

The diffusion of nitrogen in the steel follows Fick's First Law,

$$\mathbf{J}^{c}\,|_{x=0} = (-\mathbf{D}^{c}\,\frac{\partial C}{\partial X})\,|_{x=0}$$

(3)

$$\mathbf{J}^{d}\,|_{x=\xi} = (-\mathbf{D}^{d}\,\frac{\partial C}{\partial X})\,|_{x=\xi}$$

(4)

where D^{c} and D^{d} are the diffusion coefficient of nitrogen in compound layer and diffusion zone, respectively. Substituting Equations 3 and 4 into Equation 2 yields

$$(\mathbf{N}^{c} - \mathbf{N}^{d})\cdot d\xi + d\mathbf{W} = [(-\mathbf{D}^{c}\,\frac{\partial C}{\partial X})\,|_{x=0} - (-\mathbf{D}^{d}\,\frac{\partial C}{\partial X})\,|_{x=\xi}$$

(5)

In equation 5, N^{s}, N^{c}, N^{d}, D^{c}, and D^{d} are the main parameters needed to be defined to simulate the nitriding process of steels.

Based on the customized Lehrer diagrams developed for the specified steels, the location of the interface between compound layer and diffusion zone is defined and the nitrogen concentrations at this interface can be provided (Figure 47 (b)). Furthermore, compound layer growth model can be correlated with the isopleths of nitrided steels. Figure 49 shows the correlation between the nitrogen concentrations at the compound layer/diffusion zone interface and the isopleth of nitrided AISI 4140.
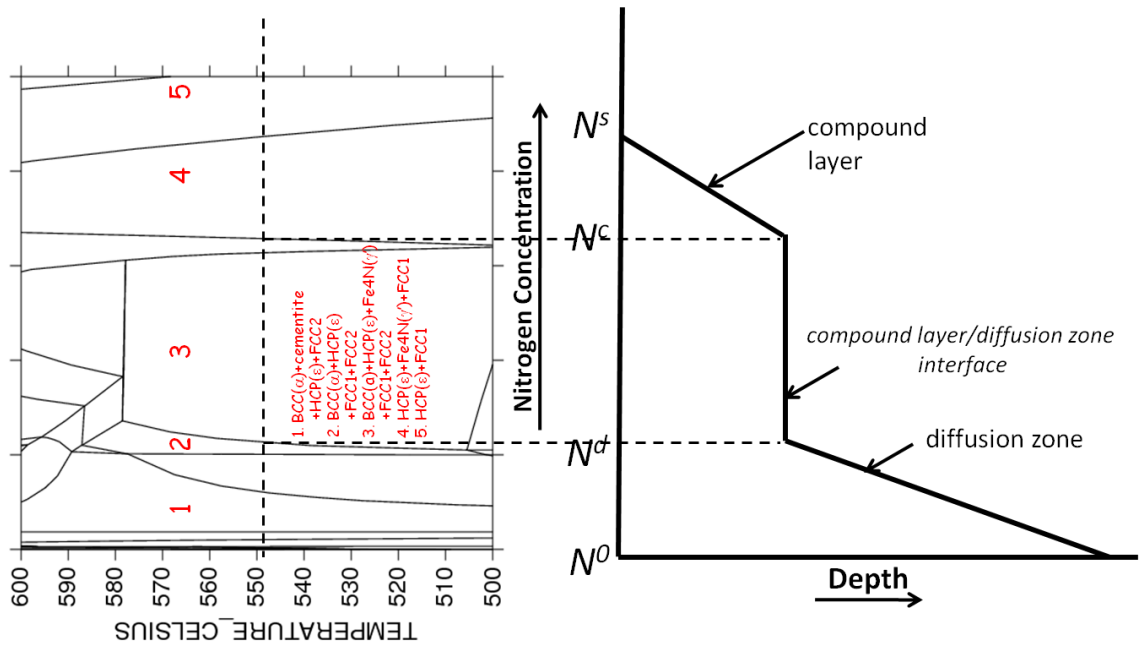
Figure 49. Relation between the isopleth (left) and nitrogen concentration/depth for the

nitride layer growth model (right) of nitrided AISI 4140

With the customized Lehrer diagram of AISI 4140, N^s is determined by the

nitriding potential used in the gas, which is 6.8wt.%N in the present experiment. N^c

is~6.5wt.%N and N^d is ~2.3wt.%N, which correspond to the nitrogen concentrations at

the interface according to Figure 49.

Due to the mixed multi-phase microstructure in the compound layer, the

effective diffusion coefficient ($<D^c>$) (equation 6) [5] is used in equation 5 to replace the

diffusivity in the compound layer, D^c. The effective diffusion coefficient in the compound

layer is the diffusion coefficient associated with the average diffusion flux through the

compound layer of thickness at ξ with concentration range from N^s to N^c [5].

$$< D^c >= \frac{1}{N^s - N^c} \int_{N^c}^{N^s} D^c dc$$

$$(6)$$

The effective diffusion coefficient can be experimentally determined based on the compound layer growth kinetics, i.e. the relationship between the compound layer thickness and the nitriding process time.

18. Results and discussion

Based on the layer growth model and the above analysis, N^s, N^c, and N^d are determined by the Lehrer diagram of AISI 4140. $<D^c>$ and D^d are still unknown. The effective diffusivity in the compound layer $<D^c>$ is calculated by using the compound layer thickness, which is about 19μm. An inverse method, that compares the results of the simulated and experimental nitrogen concentration profiles from the OES measurements, was used to determine the diffusivity in the diffusion zone, D^d. $<D^c>=2.8\times10^{-9}$cm^2/s and $D^d=5\times10^{-9}$cm^2/s are applied for AISI 4140 in the present work. The initial simulation of the nitrogen concentration profile from the compound layer growth model for AISI 4140 is shown in Figure 50. The red lines are nitrogen concentration profile calculated from the compound layer growth model. It shows very good agreement with the experimental data from OES.

The simulation results prove that the compound layer growth model can be used to simulate the gas nitriding process of steel. To apply the compound layer growth model to other steels, the boundary conditions (N^s, N^c, N^d) can be determined from the customized Lehrer diagrams. And the diffusivities need to be determined from series of

experiments for various steels. It is thus important to build up the accurate database for the diffusivities. Based on this database, the compound layer growth model can be used to provide gas nitriding process parameters for various steels.
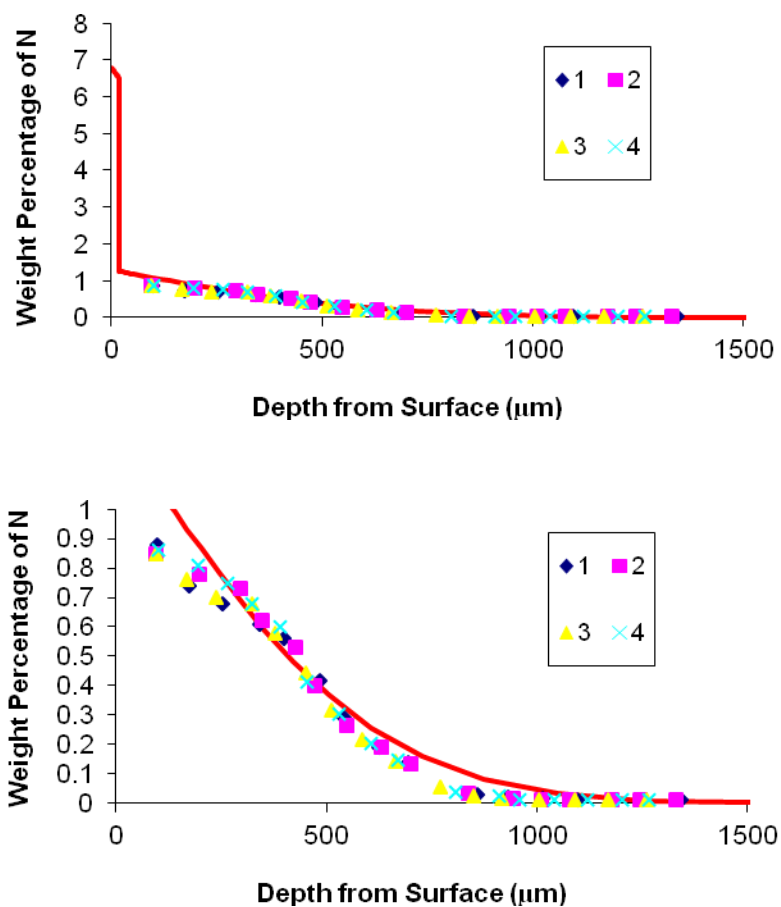
Figure 50. The initial simulation results for nitrided AISI 4140 in comparison with the OES measurement data from 4 different locations.(a): the complete nitrogen concentration profile; (b): the nitrogen concentration profile in the diffusion zone

19.Summary

In this paper, detailed analysis of the customized Lehrer diagram of AISI 4140 was discussed. The simulation of the nitriding process of AISI 4140 is demonstrated with the adoption of the compound layer growth model. The important boundary conditions, i.e. N^s, N^c, and N^d, for the first time are fixed, which are taken from our customized Lehrer diagram. The initial attempt for the adoption of the compound layer growth model shows good agreement with experimental data. It shows the possibility of utilizing the compound layer growth model in other steels. For specific steel, the customized Lehrer diagrams can be developed to provide the boundary conditions. The effective diffusivity inside the compound layer and the diffusivity in diffusion zone can be determined experimentally. The nitriding process of various steels can be thus modeled and predicted in the future.

Acknowledgement

References

1   M. A. J. Somers, *Heat Treatment of Metals* 27, (2000) 92-102.

2   D. Pye, *Practical nitriding and ferritic nitrocarburizing*, ASM International, Materials Park, OH (2003).

3   H. Baker *Alloy Phase Diagram*, American Society for Metals, Materials Park, OH (1992)

4   J. R. Davis *Surface engineering for corrosion and wear resistance*, ASM International, (2001)

5   M. A. J. Somers, E. J. Mittemeijer, *Metallurgical and Materials Transactions a-Physical Metallurgy and Materials Science* 26, (1995) 57-74.

6   M. A. J. Somers, E. J. Mittemeijer, *Heat Treating 1997: Proceedings of the 17th Conference (ASM International)* 15-18, (2000) 321-330.

7   L. Torchane, P. Bilger, J. Dulcy, M. Gantois, *Metallurgical and Materials Transactions a-Physical Metallurgy and Materials Science* 27, (1996) 1823-1835.

8   M. Yang, D. Belsito, B. Yao, Y. H. Sohn, R. D. Sisson Jr. *Intelligent Heat Treating: Simulation of the Ferritic Nitriding Process – Database Development*, Houston, TX, (2010)

9   M. Yang, B. Yao, Y. H. Sohn, R. D. Sisson Jr., *International Heat Treatment and Surface Engineering* 5, (2011) 122-126.

10   E. Lehrer, *Zeitschrift fuer Elektrochemie und Angewandte Physikalische Chemie* 36, (1930) 383.

11   N. Saunders, A. P. Miodownik, *CALPHAD (Calculation of Phase Diagrams): A Comprehensive Guide*, Pergamon, Oxford, New York (1998).

12   J. O. Andersson, T. Helander, L. H. Hoglund, P. F. Shi, B. Sundman, *CALPHAD* 26, (2002) 273-312.

Chapter 4

RESEARCH CONCLUSIONS

This thesis presents results of our work on the gas nitriding process simulation for steels through a series of papers.

There has been ongoing effort on the simulation of the gas nitriding process since 1990s and most of the work has been done to simulate the gas nitriding process of pure iron. However, in real industrial applications pure iron is never used for gas nitriding process and the simulation for steels is thus deeply needed.

The classic Lehrer diagram, which was developed in 1930s on the nitriding of pure iron is widely used in the current gas nitriding process systems to provide the process parameters of steels based on the "belief" the phase equilibria and the nitriding behavior of steel are similar to those of pure iron. However, applying the pure iron Lehrer diagram for the steels can lead to erroneous results because of the different phase stabilities in the steels.

To simulate the gas nitriding process for steels, the fundamentals of this process must be investigated first. The phase and microstructure evolution during the gas nitriding process of AISI 1045 and AISI 4140 has been investigated by computational thermodynamics and experimental investigations. (Paper #1)

- Based on thermodynamic calculation results, ε - $Fe_{2-3}(C, N)$ phase becomes stable with the increase of nitrogen concentration and γ' - Fe_4N becomes the dominate

phase with high nitrogen concentration. γ' - Fe_4N should coexist with ε - $Fe_{2-3}(C, N)$ for both alloys.

- The nitrided AISI 1045 and AISI 4140 samples were analyzed with a variety of characterization tools, including optical microscopy, OES, XRD, SEM, and TEM. The nitrogen concentration decreases monotonically from the surface through the diffusion zone for both alloys. The compound layer consisted of two layers; the outer layer contains γ' - Fe_4N and ε - $Fe_{2-3}(C, N)$ while in the inner layer is mostly Fe_4N.

- TEM analysis using HAADF and SAED demonstrated that the γ' - Fe_4N coexists with ε - $Fe_{2-3}(C, N)$ in the compound layer. This is consistent with the predictions by the CALPHAD approach.

To further understand the thermodynamics involved in the gas nitriding process for steels, the customized Lehrer diagram of AISI 4140 was successfully developed by computational thermodynamics (Paper #2). The customized Lehrer diagram differs from the Lehrer diagram of pure iron significantly. This diagram predicted the coexistence of ε - $Fe_{2-3}(C, N)$ and γ' - Fe_4N under the present nitriding process parameters. TEM diffraction analysis verified co-existence of the γ' - Fe_4N with ε - $Fe_{2-3}(C, N)$ in the compound layer of the nitrided AISI 4140 sample. It is consistent with the prediction from the customized AISI4140 Lehrer diagram. The correction of the customized Lehrer diagram is thus verified and this proves the utility of using computational thermodynamics to develop the customized Lehrer diagrams for the specified steels.

In Paper #3, the isopleths and customized Lehrer diagrams of various Fe-C alloys and carbon steels were drawn in comparison with those of pure iron. The detail comparisons show the effect of Carbon and Manganese on the nitriding temperatures and the phase stabilities during the nitriding process. It is seen that the addition of C stabilized the ε phase. The maximum nitriding temperature is greatly reduced due to the addition of C decreasing the eutectoid temperature. Mn decreases the stability of ε phase in the diffusion zone. Similar analysis of the other important alloying elements such as Al, Cr, V, and Mo can be discussed by using the same approach. Based on these understanding, the gas nitriding process of specified steel can be optimized and new nitridable steels may be designed.

In Paper #4, the compound layer growth model based on the customized Lehrer diagram is developed to simulate the gas nitriding process for AISI 4140. The important boundary conditions are determined from the customized Lehrer diagram. The simulation results of the compound layer growth model shows good agreement with experimental data. It proves the concept of utilizing the compound layer growth model in other steels. With the customized Lehrer diagrams and the experimental nitrogen concentration profiles, the effective diffusivity inside the compound layer and the diffusivity in diffusion zone can be determined. The gas nitriding process of various steels can be thus modeled and predicted.

Overall, as a breakthrough of gas nitriding process, this thesis focuses on the development of customized Lehrer diagram and the compound layer growth model. The customized Lehrer diagrams for specified steels can provide correct process control

parameters, which is the key point for the accurate gas nitriding process control. More importantly, the compound layer growth model is constructed to take the gas nitriding process kinetics into consideration. By combing the compound layer growth model and customized Lehrer diagram, the gas nitriding process of various steels can be predicted and controlled to meet the specifications.

Paper Review for MTE PhD Qualify Oral Exam

Models for Numerical Treatment of Multicomponent Diffusion in Simple Phases

1.   Paper Selected:

Models for numerical treatment of multicomponent diffusion in simple phases

Author(s): **Jan-Olof Andersson** and **John Ågren**

Source: Journalof Applied Physics

Volume: 72   Issue: 4   Pages: 1350-1355

Published: AUG 15 1992

Times Cited: **183**   References: 10

2.   The need for the paper and its importance:

It is well known that the performance of the materials is defined by the material properties and almost all the important engineering properties are structure-sensitive. The microstructure evolution control during the process is thus important. With the development of material properties design and optimization, it becomes necessary to simulate the microstructure evolution by using mathematical modeling.

The rate of diffusion-controlled phase transformations can be estimated from the volume diffusion rate of the different components if the thermodynamic local equilibrium is assumed at the moving phase boundary. Therefore, when the thermodynamic behavior and the volume diffusivities of a system are known it is possible to simulate the phase boundary migration rate without any experimental information on the phase transformation itself. This approach has a strong predictive potential which should be of great practical importance in materials science.

By application of the CALPHAD[1] (CALculation of PHAse Diagram) approach, the consistent thermodynamic databases can be constructed and used to simulate the thermodynamic behavior in multicomponent system. For the diffusion in multicomponent system, it is also necessary to choose some model to construct the consistent kinetic databases, which can be used to simulate the multicomponent phase transformations when combined with the thermodynamic databases. The aim of this paper is to suggest such kind of model to treat the multicomponent diffusion and describe how to implement it on the computer.

Based on the analysis of this paper, atomic mobilities, which are defined as the atomic drift velocity for a unit driving force, instead of diffusion coefficients are chosen to be modeled to construct the kinetic databases. The reason of using atomic mobilities is that there are only $(n-1)$ mobilities compared to $(n-1)^2$ interdiffusion coefficients and $n \times (n-1)$ intrinsic diffusion coefficients. By combining atomic mobilities with the thermodynamic factor, which is the second derivative of the Gibbs free energy with

respect to concentration, the diffusion coefficients can be calculated. Furthermore, since atomic mobility Ω_k can be expressed as

$$\Omega_k = \Omega_k^0 e^{-Q_k/RT} \tag{1}$$

where Ω_k^0 is frequency factor, Q_K is an activation energy and both depend on composition and temperature, in the spirit of the CALPHAD approach, the authors proposed that in a multicomponent system both Ω_k^0 and Q_K can be expressed with a linear combination of the values at each end point of the composition space and a Redlich–Kiste polynomial (detail will be described later).

By adopting this model, DICTRA, a software tool used for detailed simulations of diffusion controlled phase transformations for multicomponent systems, is developed. The power of this tool is not only to utilize the well-defined kinetic database but also to develop the consistent kinetic databases from the experimental information on diffusion. This approach is widely accepted to model the diffusion coefficients as an efficient representation of the composition dependence in multicomponent systems. According to the times cited of this paper, which is 183 times, many efforts have been done including experiments and modeling to expand the mobility databases for various multicomponent systems.

3.   Summary of the paper:

The first part of this paper is mainly a generalization of previous work by Kirkaldy [2] on ternary diffusion and a continue study by Agren [3]. The authors presented the multicomponent diffusion concepts such as frame of references, entropy production and driving force, linear theory and phenomenological coefficient, and practical diffusion coefficients. A suitable formalism in multicomponent systems is then suggested to represent the fluxes J_K entering the mass conservation equation

$$\frac{\partial C_K}{\partial t} = -div(J_K)$$

(2)

where C_K is the amount, e.g., moles or kilograms, of K component per unit volume and div denotes the divergence operator. This formalism is used to treat the multicomponent diffusion and forms the basis of the kinetic database.

Furthermore, in order to implement the above formalism on the computer the authors described the models for phenomenological coefficients in crystalline phases. Based on these models, mobility is adopted to model the experimental diffusion information and implemented into a general package of computer programs to simulate the multicomponent phase transformation.

4.   The work before the paper:

This paper focused on the numerical modeling of multicomponent diffusion in simple phases. Before the publication of the paper, there had been extensive development

in the field of computational thermodynamics and kinetics for the multicomponent diffusion.

4.1. The theoretical development of multicomponent diffusion

After Adolf Fick proposed Fick's laws[4], there was considerable progress in the understanding of diffusion in solids and liquids. The diffusion in one component (pure) and two-component (binary) systems are relatively easy. And there are simple standard solutions for those diffusions.

In an isothermal, isobaric one-phase binary alloy, a net flux of the corresponding components is established with the presence of a concentration gradient in one direction x. The law relating flux and concentration gradient is Fick's first law, which is expressed as

$$J_B = -D_B \frac{\partial C_B}{\partial x} \tag{3}$$

where J_B is the flux, i.e., the amount of diffusing substance that passes per unit time and unit area of a plane perpendicular to the x direction. C_B is the concentration of B, i.e., the amount of the diffusing substance per unit volume. x is the position on the x direction. D_B is the intrinsic diffusivity of B for interstitial diffusion, which defined with respect to the lattice-fixed frame of reference and the interdiffusion coefficient of B for substitutional diffusion, which defined with respect to the number-fixed frame of reference. Generally, D_B depends on concentration and temperature.

By itself, Fick's first law is not very useful in practice application. However, when combined with the mass conservation equation which considers the concentration changes with time,

$$\frac{\partial C_B}{\partial t} = \frac{\partial}{\partial x}(-J_B)$$

(4)

it gives the fundamental differential equation of diffusion

$$\frac{\partial C_B}{\partial t} = \frac{\partial}{\partial x}(D_B \frac{\partial C_B}{\partial x})$$

(5)

This is the Fick's second law, which can be used to predict the phase boundary migration rate when combined with thermodynamic data.

For the alloys contain more than two components, i.e., the multicomponent systems, it is found that the diffusivities in Fick's first law do not only depend on concentration but also on the concentration gradients [5, 6]. This makes Fick's first law rather useless for practical calculations in multicomponent alloys.

There are several important theories as the fundamental of solving the diffusion in multicomponent systems, i.e. linear response theory, absolute reaction theory, and Onsager reciprocal relations.

The first one is the linear response theory is proposed by Kubo[7]. It is to describe the response of the output signal to the input signal. Diffusion is one area that linear response theory is widely used. The key conclusion is that the output signal (flux) is in linear response to the input signal (driving force) in irreversible processes while the system is close to equilibrium state.

The second one is the methodology of absolute reaction theory which is developed independently by Eyring [8] and Meredith Gwynne Evans and Michael Polanyi [9, 10]. It is also called transition state theory. The theory assumes there is a special type of chemical equilibrium (quasi-equilibrium) between initial state and the activate transition state. The energy difference between these two states is the energy barrier that the system needs to overcome to reach the final state.

The absolute reaction theory is used primarily to understand qualitatively how chemical reactions take place. The absolute reaction theory has been successful in calculating the standard enthalpy of activation (Δ*H), the standard entropy of activation (Δ*S), and the standard Gibbs energy of activation (Δ*G) for a particular reaction if its rate constant has been experimentally determined. (The * notation refers to the value of interest at the transition state.)

The third important theory is the Onsager reciprocal relations. Onsager [11]proposed the Onsager reciprocal relations to express the relationship between different pairs of flows and forces in thermodynamic systems out of equilibrium. The

reciprocal relations apply generally in many places and are treated as the fundamental of the diffusion modeling.

According to the Onsager's reciprocal relations, in the regime where both the flows J_i are small and the thermodynamic forces ∇I_j vary slowly, there will be a linear relation between them, parameterized by a matrix of coefficients conventionally denoted L:

$$J_i = \sum_j L_{ij} \nabla I_j \qquad (6)$$

The Onsager reciprocal relations become very useful in multicomponent system, as the diffusion is determined by the matrix of L. For n-component system, the n x n matrix for L is needed. However, the system of n equation with n^2 coefficient can be reduced to a set of independent equations containing $(n-1)^2$ coefficients since only n-1 chemical potentials are independent. The structure is further reduced by the application of Onsager reciprocal relations[11], which states that if a proper choice is made for the independent fluxes, J_i and the forces ∇I_j, the reduced matrix of phenomenological coefficients is symmetric, i.e.:

$L_{ij} = L_{ji}$ (i, j= 1, 2, ...n)

It may appear that linear response theory and absolute reaction theory conflict with each other. In the linear theory the fluxes are linear functions of the driving forces. But by application of the absolute reaction rate theory, nonlinear expressions will be obtained in general for the fluxes from atomistic model derivation. After the simplification, both theories can be used together. If Taylor expansion around the equilibrium states is appliedto derive atomistic model for fluxes $\tilde{J}_k$ in the lattice fixed frame of reference the linear expressionswill be obtained:

$$\tilde{J}_k = -\sum_{j=1}^{n} L_{kj} \nabla \mu_j \tag{7}$$

where the L_{kj} are phenomenological parameters that relate the flux of k to all the driving forces. The zeroth order term vanishes because here only flow caused by chemical potential gradients $\nabla \mu_j$ is interested.

After the effort of Onsager, more complete investigations were done by Groot and Mazur [12], de Groot [13], Prigogine [4], and Fitts[14]. The entropy production in the irreversible processes was investigated.

There are also two important experimental discoveries by Kirkendall and Darken respectively.

In 1947, Ernest Kirkendall [15]reported the results of experiments on the interdiffusion between copper and zinc in brass and observed the movement of the interface between the different phases due to high-temperature interdiffusion, now called

the Kirkendall Effect. This phenomenon supported the idea that atomic diffusion occurs through vacancy exchange. Since its discovery, the Kirkendall Effect has been found in various alloy systems, and studies on lattice defects and diffusion developed significantly.

In 1949, L. S. Darken[5]published his experiments in Fe-Si-C ternary system to show the uphill diffusion phenomenon, which proved the driving force of diffusion is chemical potential gradients instead of the concentration gradients.

Furthermore, with the effort of Kirkaldy [2], the solutions of multicomponent diffusion can be achieved. It is realized that the diffusion can be described by the product of a kinetic parameter, atomic mobility and a thermodynamic factor, the second derivative of the Gibbs free energy with respect to concentration. The thermodynamic factor can be directly achieved from the computational thermodynamics.

Dayananda [16] proposed a method to determine the atomic mobilities in multicomponent system. It shows that mobilities can be obtained directly from the cumulative intrinsic fluxes past the Kirkendall interface. Further experiments were investigated with infinite diffusion couples in the Cu-Ni-Zn system by Sisson and Dayananda [17] to determine the intrinsic and interdiffusion coefficients in multicomponent system. Based on this experimental determination method a new approach of studying the diffusion in multicomponent system was established by measuring the concentration profiles [18], which is an alternative and efficient way to

model the diffusion in multicomponent systems. A series papers were thus published to investigate the diffusion in multicomponent systems [19-24]. A user-friendly computer program called MultiDiFlux has been developed by Dayananda and Ram-Mohan [25] to carry out the interdiffusion flux and interdiffusion coefficients calculations from experimental data on concentration profiles of solid-solid diffusion couples.

4.2. The development of computational thermodynamics

The computational thermodynamics was developed starting from 1970s [26]. With the effort, it became possible to use the phase equilibrium information, such as liquidus, solidus, etc, and thermochemical data, such as enthalpy, entropy, and heat capacity, etc., to establish consistent Gibbs energy descriptions of individual phases in complex systems. Many different types of phase diagrams, such as isothermal sections, isopleths, liquidus projections, in multicomponent systems are readily calculated with the thermodynamic database. The extensive development of the computational thermodynamics provides the reliable thermodynamic database, which makes it possible to do the multicomponent phase transformations simulation.

Therefore, with a lot of efforts in computational thermodynamics and diffusion investigation in multicomponent systems, the world is ready for the phase transformation simulation of the multicomponent system. However, before the publication of this paper, it was not generally realized all the previous efforts can be combined together topave the way for the computational phase transformations simulation.

5.   The contributions of the paper:

In the traditional diffusive reactions treatment the diffusion coefficients are usually evaluated from the experiments. In the multicomponent system a large number of diffusion coefficients have to be evaluated, and moreover, they are generally functions of alloy composition and are interrelated. A database of diffusivities would thus be very complex. A superior alternative is to store atomic mobility in the database, rather than diffusion coefficients. The number of parameters which need to be stored in the kinetic database will then be substantially reduced and the parameters are independent. The diffusion coefficients, which are used in the simulations, can then be obtained as a product of the thermodynamic and the kinetic factors.

This paper describes in detail how to relate the mobilities to diffusivities and how to implement the mobilities into the computational modeling. The mobilities database forms the basis of the kinetic database which, when combined with the thermodynamic database, can be used to predict the progress of phase transformations.

In this paper, the atomic mobility Ω_k is adopted to construct the kinetic database. The mobility was further divided into a frequency factor Ω_k^0 and an activation energy Q_K from absolute reaction rate theory arguments.

$$\Omega_k = \Omega_k^0 e^{-Q_k/RT} \tag{1}$$

Both Ω_k^0 and Q_K are generally depend on the composition, the temperature, and the pressure. It is convenient to represent these composition dependencies with expressions used to represent thermodynamic quantities. The composition dependency is thus represented with a linear combination of the values at each end point of the composition space and a Redlich-Kister expansion. For example, in a binary A-B substitutional alloy the activation energy would be expressed as:

$$Q_A = x_A Q_A^A + x_B Q_A^B + x_A x_B \sum_{k=0}^{m} {}^k Q_A^{A,B} (x_A - x_B)^k \qquad (8)$$

Equivalent equation is used for frequency factor:

$$\Omega^0{}_A = x_A \Omega^{0A}{}_A + x_B \Omega^{0B}{}_A + x_A x_B \sum_{k=0}^{m} {}^k \Omega^{0A,B}{}_A (x_A - x_B)^k \qquad (9)$$

The advantages of this expression are:

First, the Ω_k^0 and Q_K can both be optimized and comparing with experimental data. Since the Redlich-Kister expansion is also used to describe the interaction parameters in thermodynamic modeling of solution phases. Same optimization approach and engine, such as the Parrot module in Thermo-Calc can thus be used for the optimization of Ω_k^0 and Q_K.

Second, based on the diffusion mechanisms Ω_k^0 and Q_K can be correlated with the experimental data of various diffusion coefficients. Then these experimental data can be used to optimize and fix the modeling parameters in Ω_k^0 and Q_K.

For crystalline phases the vacancy exchange mechanism was applied. In this model it is assumed that diffusion occurs by atoms jumping into neighboring vacant lattice sites. It is assumed that at each instance there is a random distribution of vacant sites as well. In the lattice fixed frame of reference, the diffusional flux of a component k is

$$\tilde{J}_k = -c_k y_{Va} M_{kVa} \nabla \mu_k \tag{10}$$

where y_{Va} is the site fraction of vacancy in the sublattice where k is dissolved and M_{kVa} is a kinetic parameter that gives the rate of exchange if there is a vacancy adjacent to a k atom.

With the linear response theory mentioned above, the flux in lattice fixed frame of reference is expressed as

$$\tilde{J}_k = -\sum_{j=1}^{n} L_{kj} \nabla \mu_j \tag{11}$$

Comparing these two expressions, it is identified that

$$L_{kk} = -c_k y_{Va} M_{kVa} \tag{12}$$

Now the relation between M and L is established. And it is convenient to introduce

$$\Omega_k = y_{Va} M_{kVa} \tag{13}$$

Ω_k is the mobility that depends on composition, temperature, and pressure.

And since some of the experimental data are achieved in the volume fixed frame of reference, it is necessary to know how to relate the phenomenological coefficients in different frame of references. In the volume fixed frame of reference,

$$J_k = -\sum_{j=1}^{n} L'_{kj} \nabla \mu_j \tag{14}$$

Therefore, the relationship between L_{kj} and L'_{kj} lies in the following equations

$$L'_{kj} = \sum_{i=1}^{n} [\delta_{ik} - x_k (\frac{V_i}{V_m})] L_{ij} \tag{15}$$

where δ_{ik} is the Kronecker delta, i.e., = 1 when i= k and 0 otherwise.

However, in practical calculations it is usually more convenient to treat concentration gradients rather than potential gradients and all the direct experimental data are the diffusivities. It would be great if diffusivities instead of L_{kj} can be fixed. By using the chain rule of derivation, D_{kj} can be related with L_{kj}.

$$D_{kj} = \sum L_{kj} \frac{\partial \Phi_i}{\partial c_j} \tag{16}$$

Because of the relation between the concentration gradients,

$$\sum_{j=1}^{n} c_j V_j = 1 \tag{17}$$

it is possible to eliminate one of them. And thus the flux is now expressed as

$$J_k = -\sum_{j=1}^{n-1} (D_{kj} - D_{kn}) \nabla C_j \tag{18}$$

From this equation, a new type of diffusivity is introduced

$$D_{kj}^n = D_{kj} - D_{kn}(V_j / V_n) \tag{19}$$

and finally obtain

$$J_k = -\sum_{j=1}^{n-1} D_{kj}^n \nabla C_j \tag{20}$$

which represents the fluxes entering the mass conservation equation.

6. The limitation of this paper:

There are some limitations of this paper. It oversimplified the flux formalism with the linear response theory. The first order term with the Taylor expansion is adopted. However, higher order terms also play important roles in some cases.

In this paper the diffusion in simple phases was described. The simple phases mean disordered substitutional and substitutional-interstitial crystalline phases and disordered liquids. The phases exhibiting various ordering phenomena, the formation of molecular like species, and phases having a complicated crystal structure were not described and limitedthe practical applications.

7. The state of the art after the publication of this paper:

After the publication of this paper, many practical advances were made in the numerical simulation of multicomponent diffusion field.

The first one is the mature and the industrial application of numerical simulations. DICTRA, a software tool used for detailed simulations of diffusion controlled phase transformations for multicomponent systems, is developed based on the models established in this paper. In order to perform simulations using DICTRA, both thermodynamic and kinetic descriptions are needed. Moreover, the results and the accuracy of the simulations critically depend on the quality of these descriptions. The

thermodynamic descriptions are available from the Thermo-Calc [27] system. Kinetic descriptions, the mobility database are available within the DICTRA system.[28-30]

Figure 51 shows the basic calculation procedure of DICTRA. It is evident that in order to perform simulations using the DICTRA software, it is necessary that both thermodynamic and kinetic data are available. The diffusivities can be defined by using the mobilities from the kinetic database and the second derivation of Gibbs free energy from the thermodynamic database to solve the diffusion equations. Furthermore, with the boundary condition of interfacial equilibrium, which is also provided by the thermodynamic database, the practical interests involving a moving boundary can be treated.

Currently, DICTRA can be used to simulate the diffusion process in many applications, such as solidification and microsegregation, growth or dissolution of secondary phases, such as carbides, nitrides, etc. carburizing, nitrocarburizing, nitriding. It can also be used to solve the moving boundary problems [31], diffusion in disperse systems [32]. Instead of modeling the simple solution phase as shown in this paper, the diffusion in complex phases can also be modeled.
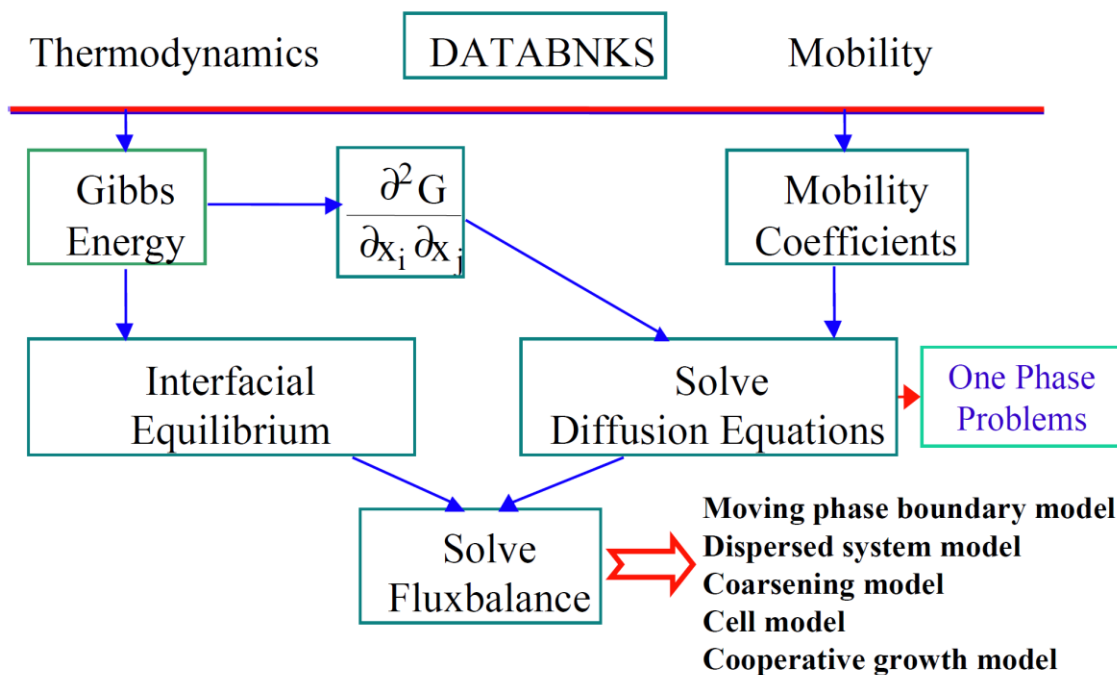
Figure 51. Basic calculation procedure of DICTRA[33]

However, there are two main limitations of DICTRA. First, DICTRA can only handle simple geometries, and thus it is not a complete simulation tool. The geometries that can be handled are planar, cylindrical, and spherical, of which all can be reduced into one space variable. Second, the sharp interface model is used in DICTRA. Based on the assumption that the phase boundary is physically sharp the local equilibrium always prevails at the interface, which is not always the case.

Because of limitations of DICTRA, the much more expensive phase field simulation becomes the hot topic, especially due to the dramatic improvement on the computing power in recent years. The phase field method[34-38], has frequently been

applied to study the phase transformation and the evolution of microstructure, such as dendritic solidification, martensitic transformations, recrystallization, grain growth, precipitation, etc. Different from DICTRA, it is straight forward to take account of various driving forces, including, chemical potentials, interface energies, elastic strain energies, and external fields. In the phase-field method, the interface between different phases or grains is defined as a finite region with a gradual variation in physical properties, i.e. the interface is diffuse in nature. The position of the interface, and the state of system, is given by the so called phase-field variable $\varphi(x, t)$ which varies smoothly from zero to one over the interface of finite thickness.

The total energy, or some other thermodynamic state function, of the system is given by a functional F. For an isobarothermal system the functional F may be expressed as

$$F = \int_{\Omega} (f(c, \phi) + \frac{\varepsilon^2}{2} \nabla \phi) d\Omega \qquad (21)$$

where f is the Gibbs energy density, c is the concentration and Ω is the domain, e.g. the volume of the system. The phase-field variable is a non-conservative quantity, and its temporal evolution is postulated to obey the Allen-Cahn equation[39]

$$\frac{\partial \phi}{\partial t} = -M_\phi \frac{\delta F}{\delta \phi} \qquad (22)$$

where M_ϕ is a kinetic parameter playing the role of an interfacial mobility. The equation above is sometimes also referred to as the time-dependent Landau-Ginzburg equation. The concentration of element k, c_k, is a conserved quantity and the time evolution is thus governed by the continuity equation

$$\frac{\partial c}{\partial t} = -\nabla J \tag{23}$$

To obtain an expression for the flux of element k the Onsager linear law of irreversible thermodynamics is applied

$$J = -L''\nabla(\frac{\delta F}{\delta c}) \tag{24}$$

The solution of Eqs. (21)−(24) then yields the microstructural evolution of the system.

Although the phase field approach is very powerful and popular nowadays, the kinetic simulation using DICTRA is still very important in industrial applications. As a relative low computer power consumption approach, it can provide quick and pretty reliable results, especially when the interface energy doesn't play a dominant role. DICTRA and phase field are pretty comparable for one dimensional kinetic simulation.

References:

1   N. Saunders, A. P. Miodownik, *CALPHAD (Calculation of Phase Diagrams): A Comprehensive Guide* Pergamon, Oxford, New York (1998).

2   J. S. Kirkaldy *in Advances in Materials Research*, Wiley, New York (1970)

3   J. Ågren, *Journal of Physics and Chemistry of Solids* 43, (1982) 421-430.

4   A. Fick, *Annalen der Physik* 170, (1855) 59-86.

5   L. S. Darken, *Transactions AIME* 180, (1949) 430-438.

6   L. S. Darken, *Transactions AIME* 150, (1942) 157-171.

7   R. Kubo, *J. Phys. Soc. Jpn.* 12, (1957) 570-586.

8   H. Eyring, *Journal of Chemical Physics* 3, (1935) 107–115.

9   K. Laidler, *The chemical intelligencer* 4, (1998) 39.

10   K. J. Laidler, M. C. King, *The Journal of Physical Chemistry* 87, (1983) 2657-2664.

11   L. Onsager, *Phys. Rev.* 37, (1931) 405 - 426.

12   S. R. d. Groot, P. Mazur, *Non-Equilibrium Thermodynamics*, Wiley, New York (1962).

13   S. R. d. Groot, *Thermodynamics of Irreversible Processes,*, North-Holland Publ. Co., Amsterdam (1952).

14   D. D. Fitts, *Nonequilibrium Thermodynamics: A Phenomenological Theory of Irreversible Processes in Fluid Systems*, McGraw-Hill, New York (1962).

15   A. D. Smigelskas, E. O. Kirkendall, *Trans. AIME* 171, (1947) 130-142.

16   M. A. DAYANANDA, *TRANS MET SOC AIME.* 242, (1968) 1369- 1372.

17   R. Sisson, M. Dayananda, *Metallurgical and Materials Transactions A* 8, (1977) 1849-1856.

18   M. A. Dayananda, C. Kim, *Metallurgical and Materials Transactions A* 10, (1979) 1333-1339.

19   M. A. DAYANANDA, *Metallurgical and Materials Transactions A* 14, (1983) 1851-1858.

20   C. Kim, M. Dayananda, *Metallurgical and Materials Transactions A* 15, (1984) 649-659.

21   M. A. DAYANANDA, *Defect and Diffusion Forum* 95-98, (1993) 521.

22   M. Dayananda, *Metallurgical and Materials Transactions A* 27, (1996) 2504-2509.

23   M. A. Dayananda, Y. H. Sohn, *Scripta Materialia* 35, (1996) 683-688.

24   M. A. Dayananda, Y. Sohn, *Metallurgical and Materials Transactions A* 30, (1999) 535-543.

25   M. A. Dayananda, L. R. Ram-Mohan *"MultiDiFlux" website* https://engineering.purdue.edu/MSE/Fac Staff/Faculty/dayananda.wshtml

26   L. Kaufman, H. Bernstein, *Computer Calculation of Phase Diagrams*, Academic Press, New York (1970).

27   J. O. Andersson, T. Helander, L. HÃ¶glund, P. Shi, B. Sundman, *Calphad* 26, (2002) 273-312.

28   T. Helander, J. Ågren, *Acta Materialia* 47, (1999) 1141-1152.

29   Nsson, B, *Ferromagnetic ordering and diffusion of carbon and nitrogen in bcc Cr-Fe-Ni alloys*, Hanser, München, ALLEMAGNE (1994).

30   B. Jonsson, *Zeitschrift fur Metallkunde (Germany)* 83, (1992) 349-355.

31   S. Crusius, G. Inden, U. Knoop, L. Hoglund, J. Ågren, *Z Metallkd* 83, (1992) 673–678.

32   A. Engstrà¶m, L. Hà¶glund, J. Ã…gren, *Metallurgical and Materials Transactions A* 25, (1994) 1127-1134.

33   Z.-K. Liu *Introduction of Dictra*,

34   J. W. Cahn, J. E. Hilliard, *J Chem Phys* 28, (1957) 258-267.

35   A. A. Wheeler, W. J. Boettinger, G. B. McFadden, *Physical Review A* 45, (1992) 7424.

36   K. Ryo, *Physica D: Nonlinear Phenomena* 63, (1993) 410-423.

37   L. Q. Chen, *Scripta Metall Mater* 32, (1995) 115-120.

38   I. Steinbach, F. Pezzolla, B. Nestler, M. SeeÃŸelberg, R. Prieler, G. J. Schmitz, J. L. L. Rezende, *Physica D: Nonlinear Phenomena* 94, (1996) 135-147.

39   S. M. Allen, J. W. Cahn, *Acta Metall* 27, (1979) 1085-1095.